Fundamental Carrier-Envelope Phase Noise Limitations during Pulse Formation and Detection

Dissertation

zur Erlangung des Grades eines
Doktors der Naturwissenschaften (Dr. rer. nat.)

am Fachbereich Physik
der Freien Universität Berlin

vorgelegt von

Johannes Nils Raabe

Berlin 2019

Erstgutachter:	Prof. Dr. M. J. J. Vrakking
Zweitgutachter:	Prof. Dr. M. Weinelt
Tag der Disputation:	09.01.2020

Selbständigkeitserklärung

Hiermit bestätige ich, dass die vorliegende Dissertation selbstständig und nur unter Verwendung der angegebenen Literatur und Hilfsmittel verfasst wurde. Die Arbeit ist nicht in einem früheren Promotionsverfahren angenommen, noch mit ungenügend beurteilt worden.

Aurich, 30.07.2019 _____

Johannes Nils Raabe

Abstract

The difference between the positions of the maximum peak of the carrier wave of a laser pulse and the maximum of its intensity envelope is termed carrier-envelope phase (CEP). In the last decades, the control and stabilization of this parameter has greatly improved, which enables many applications in research fields that rely on CEP-stable pulses such as attosecond science and optical frequency metrology. Further progress in these fields depends strongly on minimizing the CEP noise that restricts stabilization performance. While the CEP of most high repetition-rate low-energy laser oscillators has been stabilized to a remarkable precision, some types of oscillators show extensive noise that inhibits precise stabilization. The CEP stabilization performance of low repetition-rate high peak-power amplified laser systems also remains limited by noise, which is believed to stem mainly from the CEP detection process.

In this thesis, the origins of the CEP noise within four oscillators as well as the noise induced by the measurement of the CEP of amplified pulses are investigated. In the first part, the properties of the CEP noise of one Ti:sapphire oscillator and three different fiber oscillators are extracted by analyzing the unstabilized CEP traces by means of time-resolved correlation analysis of carrier-envelope amplitude and phase noise as well as by methods that reveal the underlying statistical noise properties. In the second part, investigations into the origin of CEP noise induced by the measurement of the CEP of amplified pulses are conducted by comparing several different CEP detection designs that are based on f-2f interferometry. These detection setups differ in the employed sources of spectral broadening as well as frequency doubling media, both necessary steps to measure the CEP. The results in both parts of this thesis show that white quantum noise dominates most CEP measurements. In one particular fiber oscillator, the strong white noise is found to be a result of a correlating mechanism within the employed SESAM. During amplifier CEP detection, the CEP noise is found to be originating only to a marginal degree from the number of photons that are detected during the measurement, which excludes shot noise as a limiting source. Instead, the analysis reveals that the origin of the observed strong white noise can be interpreted as a loss of coherence during detection. This type of coherence is termed here intra-pulse coherence and describes the phase transfer within f-2f interferometry. Its degradation is a result of amplitude-to-phase coupling during the spectral broadening process that leads to pulse-to-pulse fluctuations of the phases at the edges of the extended spectrum. Numerical simulations support the concept of intra-pulse coherence degradation and show that the degradation is substantially stronger during plasma-driven spectral broadening as compared to self-phase modulation-dominated spectral broadening. This difference in degradation also explains the much stronger CEP noise typically observed in amplified systems as compared to oscillators, as the former typically rely on filamentation-based and hence plasma-dominated spectral broadening for CEP detection. The concept of intra-pulse coherence constitutes a novel measure to assess the suitability of a spectral broadening mechanism for application in active as well as in passive CEP stabilization schemes and provides new strategies to reduce the impact of the CEP detection on the overall stabilization performance of most lasers.

Zusammenfassung

Diese Arbeit beschäftigt sich mit der Identifizierung und Minimierung fundamentaler Rauschquellen, die zu einer Limitierung des erreichbaren Carrier-Envelope Phasen (CEP) Jitters führen. Die Carrier-Envelope Phase beschreibt die Differenz zwischen dem Maximum der Trägerwelle und dem Scheitelpunkt der Intensitätseinhüllenden. In den letzten Jahrzehnten hat sich die Kontrolle und Stabilisierung der CEP deutlich verbessert, was zu einem schnellen Fortschritt in Forschungsfeldern geführt hat, bei denen CEP-stabile Pulse notwendig sind. Diese Forschungsfelder umfassen die Attosekundenforschung und optische Frequenzmetrologie. Weitere Entwicklungen in diesen Feldern hängt stark von der Minimierung von CEP Rauschen ab, welches die CEP Stabilisierung stark beeinträchtigt. Obwohl die CEP der Pulse der meisten Laseroszillatoren mit hohen Repetitionsraten äußerst genau stabilisiert werden kann, existieren einige Laseroszillatoren bei denen starke Rauschquellen eine Stabilisierung verhindern oder stark einschränken. Des Weiteren zeigen vor Allem verstärkte System mit niedrigen Repetitionsraten und hohen Spitzenleistungen eine Beschränkung der CEP Stabilisierung aufgrund von Rauschen, dass vermutlich zum großen Teil durch den Detektionsprozess entsteht. In dieser Arbeit ist der Ursprung von CEP Rauschen in vier unterschiedlichen Laseroszillatoren sowie während der Detektion der CEP von verstärkten Systemen untersucht worden. Im ersten Teil wurden die Eigenschaften des CEP Rauschens eines Ti:Saphir-basierten Oszillators und drei verschiedener Faserlaser analysiert. Hierzu wurde das Rauschen unter anderem mittels zeitaufgelöster Korrelationsanalyse von Carrier-Envelope Amplituden- und Phasenrauschen sowie mittels Methoden, die die statistischen Eigenschaften des Rauschens offenlegen, analysiert. Im zweiten Teil der Arbeit wurde das Rauschen untersucht, welches durch den Messprozess der CEP von verstärkten Pulsen mittels f-$2f$ Interferometrie entsteht. Experimentell wurden hierzu vier unterschiedliche Detektionsanordnungen verwendet, die sich durch die Nutzung unterschiedlicher nichtlinearer Prozesse zum Erzeugen der spektralen Verbreiterung sowie zur Erzeugung der zweiten Harmonischen unterscheiden. Die Ergebnisse in beiden Teilen der Arbeit zeigen dominierendes weißes Quantenrauschen in den meisten CEP Messungen. In einem bestimmten Faserlaser, in dem besonders starkes weißes Rauschen vorlag, konnte der Ursprung einer Wechselwirkung innerhalb des verwendeten halbleiterbasierten sättigbaren Absorbers zugeordnet werden. Bei der Detektion der CEP bei verstärkten Systemen wurde hingegen gezeigt, dass niedrige Photonenzahlen und damit Schrotrauschen nur zum kleinen Teil für die starken weißen Rauschanteile verantwortlich gemacht werden kann. Stattdessen kann die Ursache des starken Rauschens einem Verlust von Kohärenz zugeordnet werden. Diese Art von Kohärenz ist hier mit intra-Puls Kohärenz bezeichnet und beschreibt den Phasentransfer innerhalb der Detektion mittels f-$2f$ Interferometrie. Der Verlust von intra-Puls Kohärenz ist eine Folge von Amplituden-zu-Phasen Koppelung während der spektralen Verbreiterung. Von Puls zu Puls führt dies zu Fluktuationen der Phase an beiden Rändern der erzeugten spektralen Verbreiterung. Numerische Simulationen unterstützen das Konzept der intra-Puls Kohärenz und zeigen auf, dass die Degradation bedeutend stärker bei plasmadominierten Prozessen ausfällt als im Vergleich zu spektraler Verbreiterung mittels Selbstphasenmodulation. Dieser unterschiedlich starke Verlust der intra-Puls Kohärenz erklärt das deutlich höhere Rauschniveau in verstärkten Systemen im Vergleich zu Oszillatoren, da verstärkte Systeme plasmadominierte Prozesse zur spektralen Verbreiterung nutzen. Das Konzept der intra-Puls Kohärenz stellt ein neues Maß zur Einschätzung einer Methode zur spektralen Verbreiterung für eine bestimmte Anwendung dar, die sowohl in aktiven sowie passiven CEP Stabilisierungen von Lasern eine Rolle spielt. Es ermöglicht somit neue Strategien, um den Einfluss der Detektion auf die CEP Stabilisierung der meisten Laser zu senken.

Contents

Introduction

Mode-locked lasers enable routine generation of ultra-short pulses that comprise only few electric field oscillations underneath the intensity envelope [1, 2, 3]. In these few-cycle pulses the field strength of neighboring peaks of the carrier wave can vary greatly, which makes the position of the strongest peak of the carrier wave with respect to the intensity envelope maximum an important parameter. This difference is termed carrier-envelope phase (CEP) and is of particular importance for the application of ultra-short high peak power pulses in experiments that involve highly nonlinear light-matter interaction such as high-order harmonic generation (HHG) [4] and the generation of isolated attosecond pulses (IAP) [5, 6]. These ultra-short high peak power pulses are routinely generated by means of the chirped-pulse amplification (CPA) technique that has been recently awarded with the Nobel prize in physics.

In the frequency domain picture of the output of a mode-locked laser, the CEP counterpart termed carrier-envelope offset (CEO) frequency determines the stability of the position of the frequency comb[1]. In frequency metrology, the stabilization of this CEO frequency and the pulse repetition frequency enable extremely precise measurements of frequencies that are widely used in optical clockworks and will eventually be used in the future definition of the unit of time [7, 8]. In 2005, the importance of frequency metrology was recognized by the Nobel prize in physics [9].

Thus, applications of ultra-short laser pulses in frequency metrology as well as in attosecond science require the stabilization of the CEP at high precision. This demands the identification and minimization of fundamental noise sources that easily spoil the precise control over the CEP. This noise is predominately induced during pulse formation, pulse amplification and during the CEP detection process. While the CEP was measured for the first time by cross-correlation of two successive pulses [10], improved precision and subsequent control was enabled by means of f-$2f$ interferometry [11], which provides access to the CEP by heterodyning two harmonics of one pulse. Over time, the measurement and stabilization has been fine-tuned and reached a point where the CEP of a Ti:sapphire oscillator can be stabilized with residual jitters of less than 20 mrad [12]. Today, while the CEP of Ti:sapphire–based oscillators is routinely controlled very precisely, a large class of oscillators still exists that are hard to stabilize. Among these, especially high-repetition low-energy fiber oscillators have partly been spoiled by excessive noise that inhibits stabilization. The origin of this strong noise strongly depends on the type of laser and is not fully understood yet. Investigations into the governing mechanisms that determine CEP noise within the cavity mainly rely on interpreting frequency noise densities. A deeper understanding of the origin of the CEP noise may be achieved by the application of novel methodologies that allow to reveal the complex intra-cavity interaction of linear and nonlinear effects.

Despite the precise control of the CEP of ultra-short pulses of at least some types of oscillators, the stabilization of the CEP of high peak power pulses generated by amplified laser systems has re-

mained limited by noise in most cases [13, 14, 15, 16, 17]. Even when employing the best-performing CEP-stabilized Ti:sapphire-based oscillators in combination with CPA-based amplifiers the stabilization performance of these amplified systems has stagnated considerably above 100 mrad residual jitter [5, 6, 18, 19] on a shot-to-shot basis. Another class of laser amplifiers based on optical parametric chirped-pulse amplification (OPCPA) provides much longer wavelengths compared to traditionally employed near infra-red Ti:sapphire-based CPA lasers. Longer driver wavelengths enable higher harmonics to be generated, which, in turn, allow ever shorter attosecond pulses. OPCPA systems rely on parametric three-wave mixing for the passive stabilization of the CEP, which is enabled by the removal of the CEP offset in one of the resulting pulses [20, 21, 22] and thus do not require active stabilization. Nevertheless, in many cases, the remaining jitter amounts to several hundred milliradian and may readily exceed a radian [15], i.e., the CEP stabilization in those cases is not suitable for CEP-sensitive experiments. A third promising avenue for short pulse generation are mode-locked thin disk lasers that are characterized by high peak powers combined with MHz repetition rates straight out of the oscillator. Until now this class of oscillators has only demonstrated proof-of-principle results of CEP-stabilized performance [23] as the stabilization of these systems has been found difficult [13, 14].

While these lasers differ in the way they provide high peak power ultra-short pulses and hence may have different noise sources, they share the same approach for measuring the CEP, i.e., they rely on f-$2f$ interferometry. During CEP detection, the spectral content of the pulse is substantially broadened to extend over one octave. Subsequently, frequency-doubling of the lower-energy wing is carried out. The interference fringes of the fundamental and second harmonic provide access to the CEP. During the nonlinear processes, the CEP may be compromised by additional uncertainty that is introduced by shot noise [16, 24] and amplitude-to-phase coupling during spectral extension [25]. The former, shot noise, is ultimately the result of unavoidable conversion losses during the nonlinear processes within f-$2f$ interferometry. This loss leads to low photon numbers that can reduce the precision of the CEP measurement. While it is believed that shot noise introduces substantial CEP noise, it remains unanswered to what extent it is actually interfering with proper CEP extraction and stabilization. Amplitude-to-phase coupling during spectral broadening and its effect on the CEP measurement has not been deeply investigated so far. As it turns out, the underestimated effect of this coupling can be interpreted as a type of coherence degradation that ultimately has implications for the whole field of CEP stabilization.

The work presented in this thesis sets out to investigate the origin and influence of fundamental noise sources that are present during pulse formation and CEP measurement and strongly compromise the stabilization of many oscillators and amplified systems. The presented findings provide new perspectives for the CEP stabilization of currently unstabilizable oscillators and new routes to substantially improve CEP stabilization of amplified sources by bringing sub-100 mrad jitters within reach.

Chapter 1

Ultrashort Laser Pulses in Dielectric Media

This chapter begins with the theoretical background of laser pulses, which includes the mathematical approach for pulse propagation through dielectric media. As most measurement schemes of the carrier-envelope phase (CEP) rely on nonlinear spectral broadening, the important concepts of filamentation and spectral broadening in general are thus provided. Furthermore, mode-locking mechanisms are introduced that enable ultra-short pulse generation deep into the femtosecond regime. These mode-locking principles provide the basis for the understanding of fundamental CEP noise formation mechanisms in various laser oscillators. Subsequently, the carrier-envelope phase, its measurement and stabilization in oscillators and amplified systems is introduced. Finally, potential noise sources and coupling mechanisms during pulse formation within the oscillator as well as amid pulse propagation are discussed and further extended by noise that is appended during measurement of the CEP.

1.1 The Electromagnetic Pulse in Dielectric Media

Laser pulses can be described as the superposition of waves that are solutions of the wave equation, which is deduced from Maxwell's equations. In an isotropic, homogeneous, transparent medium with electronic displacement **D**, an electric field **E** and free carriers forming a current density **J** originating from ionization dynamics, the wave equation can be expressed as [26, 27, 28]

$$\nabla(\nabla\cdot\mathbf{E})-\nabla^2\mathbf{E}=-\mu_0\left(\frac{\partial^2\mathbf{D}}{\partial t^2}+\frac{\partial\mathbf{J}}{\partial t}\right), \tag{1.1}$$

where $\nabla^2=\partial_x^2+\partial_y^2+\partial_z^2$ represents the three-dimensional Laplacian operator and μ_0 the magnetic constant. The electric displacement relates to the polarization **P** via $\mathbf{D}=\varepsilon_0\mathbf{E}+\mathbf{P}$, with ε_0 the vacuum permittivity. In dielectric media, where the intensity is usually well below the ionization threshold and only the polarization is relevant to describe the response of the medium, the current density **J** is typically considered zero. However, in the case of laser filamentation the light field is highly localized, thus intense enough for ionizing the media and consequently, **J** is no longer negligible when a plasma is present. In order to obtain a solution of the wave equation, the description of light propagation is limited to weakly divergent laser beams. Therefore, the paraxial approximation is employed, where the wave vector perpendicular to the direction of propagation is considered negligible, i.e., $k_\perp \ll \boldsymbol{k}$. Thus, the solution of

Eq. 1.1 is then described as a mono-frequent, continuous plane wave **E**. Considering linearly polarized light, the electric field of a plane wave can be mathematically expressed as the combination of a carrier wave and an electric field envelope

$$E(\mathbf{r},t) = \frac{1}{2}\mathbf{e}_x[\mathcal{E}(\mathbf{r},t)\exp(ik_z z - i\omega t) + \text{c.c.}]\,, \tag{1.2}$$

where $\mathbf{e}_x = (1,0,0)$ gives the x-direction as the linear polarization orientation, which is perpendicular to the wave vector $\mathbf{k} = (0,0,k_z)$ with $k_z = \frac{\omega n}{c}$. Here the wave frequency is denoted as ω and the linear refractive index as n. Any superposition of these plane waves with different frequencies also represent a solution of the wave equation 1.1. In fact, the superposition of multiple waves $\tilde{E}$ that have different frequencies and a constant phase relationship can then be understood as the formation of a laser pulse with

$$E(\mathbf{r},t) = \int_{-\infty}^{\infty} \tilde{E}(\omega)\exp(i\omega t)d\omega\,, \tag{1.3}$$

where $\tilde{E}(\omega)$ is the electric field in the frequency domain. In general, an optical pulse has the mean or carrier frequency ω_c, which is specified as

$$\omega_c = \frac{\int_{-\infty}^{\infty}\omega\,|\tilde{E}(\omega)|^2\,d\omega}{\int_{-\infty}^{\infty}|\tilde{E}(\omega)|^2\,d\omega}\,. \tag{1.4}$$

In the case of optical laser pulses with central frequency ω_c, the spectral width $\Delta\omega$ and pulse duration τ are two dependent parameters and relate via the time-bandwidth product $\tau\Delta\omega \geq$ const., where the constant depends on the pulse shape. The shortest obtainable pulses are characterized by a flat spectral phase, which is referred to as bandwidth-limited or Fourier-limited pulses. Under the condition that the spectral amplitude $\tilde{E}(\omega)$ extends only a small range around ω_c, i.e., $\Delta\omega \ll \omega_c$, the time-dependent electric field of a laser pulse propagating in the z-direction can be written as

$$E(z,t) = \mathcal{E}(z,t)\exp(i\varphi(z,t))\exp(-i\omega_c t)\,, \tag{1.5}$$

where $\mathcal{E}(z,t)$ and $\varphi(z,t)$ represent the envelope and phase of the pulse, respectively. Assuming a narrow spectral width, commonly referred to as the slowly-varying envelope approximation (SVEA), the temporal and spatial variation of the envelope are small compared to one oscillation of the electric field, which can be expressed as

$$\left|\frac{\partial\mathcal{E}}{\partial z}\right| \ll |k(\omega_c)\mathcal{E}| \text{ and } \left|\frac{\partial\mathcal{E}}{\partial t}\right| \ll |\omega_c\mathcal{E}|\,, \tag{1.6}$$

with $k(\omega_c)$ the wave number at the carrier frequency. At a central wavelength of 800 nm, the SVEA is fulfilled for pulses as short as 10 fs, which then consist only of about four oscillations of the underlying electric field. However, the SVEA breaks down for pulses with less optical cycles, where a separation of the pulse into an envelope and a phase term does not hold anymore. Then, higher-order terms get relevant during pulse propagation and a neglectance of those terms would violate energy conservation as unphysical dc-fields are introduced. Advanced theories have been developed to properly describe pulse propagation within this regime [29, 30, 31]. Since only experiments with pulses longer than 10 fs are considered in this thesis, the validity of the SVEA is expected.

1.1.1 Propagation

During propagation through dielectric media, the pulse experiences the refractive index $n = n(\omega)$ as frequency-dependent, which, in turn, affects the pulse shape and pulse duration. Expanding the frequency dependence of the dispersion relation $k(\omega) = \frac{\omega}{c} n(\omega)$ in a Taylor series around the carrier frequency ω_c leads to

$$k(\omega) = \sum_{m=0}^{\infty} \frac{1}{m!} \beta_m (\omega - \omega_c)^m, \text{with} \tag{1.7}$$

$$\beta_m = \left. \frac{d^m k(\omega)}{d\omega^m} \right|_{\omega=\omega_c}. \tag{1.8}$$

The expansion of the dispersion relation describes the interaction between the different frequencies of the pulse with media, where β_0 and β_1 represent the phase velocity $v_p = \omega_c/\beta_0$ and group velocity $v_g = 1/\beta_1$, respectively. While the former defines the velocity of the carrier wave, the latter relates to the speed of the propagating envelope. Higher order terms, namely β_2 and β_3, are referred to as the group-velocity dispersion (GVD) and third-order dispersion (TOD), respectively, and have a direct influence on the pulse duration. Further terms are neglected here.

Since the phase and group velocities typically differ, the associated refractive index $n(\omega) = \frac{c}{v_p}$ and group refractive index[1]

$$n_g(\omega_c) = \frac{c}{v_g} = n(\omega_c) + \omega_c \left. \frac{dn(\omega)}{d\omega} \right|_{\omega=\omega_c} \tag{1.9}$$

experienced by the pulse are different. Hence, pulse propagation through dispersive media results in the continuous phase slips of the carrier wave relative to the envelope. Referred to as group-phase offset (GPO), this continuous evolving difference affects the evolution of the carrier-envelope phase (CEP) [11, 32]. In a more illustrative way of speaking, the CEP is the difference of the strongest electric field antinode and the envelope peak that is therefore affected by the changing of the GPO. During propagation in a medium, the GPO experienced by the pulse can be expressed as

$$\Delta\varphi_{\text{GPO}}(z) = \omega_c \left(\frac{z}{v_g} - \frac{z}{v_p} \right) = \frac{\omega_c z}{c} (n_g(\omega_c) - n(\omega_c)) \tag{1.10}$$

$$= \frac{\omega_c^2 z}{c} \left. \frac{dn(\omega)}{d\omega} \right|_{\omega=\omega_c}. \tag{1.11}$$

Hence, the main influence on the GPO is due to β_1, while higher orders generally act on the temporal pulse shape. So far, the treatment of the pulse propagating through dispersive media has neglected absorption. In a real medium, however, the refractive index $n(\omega) = \sqrt{\varepsilon(\omega) \cdot \mu}$ needs to be expressed using a complex scalar dielectric function $\tilde{\varepsilon}(\omega)$, while the permeability μ is typically approximated to 1.

$$\varepsilon(\omega) = 1 + \chi^{(1)}(\omega), \text{ and} \tag{1.12}$$

$$\tilde{\varepsilon}(\omega) = \varepsilon_r(\omega) + i\varepsilon_i(\omega) = \left(n(\omega) + i \frac{c}{2\omega} \alpha(\omega) \right)^2, \tag{1.13}$$

[1] The group refractive index is defined as the vacuum speed of light relative to the group velocity and hence depends on the wavelength.

where $\chi^{(1)}(\omega)$ is the linear susceptibility, $\varepsilon_r(\omega)$ and $\varepsilon_i(\omega)$ the real and imaginary part of the dielectric function and $\alpha(\omega)$ the absorption function. The susceptibility relates the dispersive properties to the linear polarization $\mathbf{P}(\omega) = \varepsilon_0 \chi^{(1)}(\omega)\tilde{E}(\omega)$. The connection between absorption and dispersion can be quantified by the Kramers-Kronig relation [33, 34], which in general relates the real and imaginary part of the refractive index via

$$n(\omega) - 1 = \frac{c}{\pi}\,\mathcal{CH}\int_0^\infty \frac{\alpha(\Omega)}{\Omega^2 - \omega^2} d\Omega\,, \tag{1.14}$$

where Ω is the angular frequency of the integration and $\mathcal{CH}$ denotes the Cauchy principal value of the integration result.

1.1.2 Nonlinear Polarization

When the optical intensity $I = {}^{cn\varepsilon_0|E|^2}/_2$ exceeds several TW/cm^2, higher-order terms of the polarization become important. Then, the response of the medium deviates from linear behavior, which can be expressed by a Taylor expansion

$$\mathbf{P} = \mathbf{P}^{(1)} + \mathbf{P}_{\mathrm{NL}} \text{ with} \tag{1.15}$$

$$\mathbf{P}_{\mathrm{NL}} = \mathbf{P}^{(2)} + \mathbf{P}^{(3)} + \mathbf{P}^{(4)} \ldots \tag{1.16}$$

$$= \varepsilon_0 \left(\chi^{(2)}\mathbf{E}^2 + \chi^{(3)}\mathbf{E}^3 + \chi^{(4)}\mathbf{E}^4 + \ldots \right). \tag{1.17}$$

Although the electric susceptibility χ is formally a tensor, here only isotropic media are considered, which allows simplification of χ to a scalar quantity. In centro-symmetric materials such as many gases, liquids and crystals, the even-order susceptibilities are vanishing and only first, third and higher odd-order susceptibilities are present. In the case of inversion symmetry, substituting the electric field from Eq. 1.2 in Eq. 1.17, while considering scalar susceptibilities, results in

$$\mathbf{P}^{(3)} = \frac{\varepsilon_0}{8}\chi^{(3)}\left[3|\mathcal{E}|^2\exp(i\omega t - ikz) + \mathcal{E}^2\exp(3i\omega t - 3ikz)\right]\mathcal{E}(\boldsymbol{r},t) + \text{c.c.}\,, \tag{1.18}$$

where the first term oscillates with a frequency of ω and the second term leads to an oscillation at 3ω, commonly referred to as third harmonic generation. While for the latter phase-matching needs to be considered in order to avoid destructive interference of the newly generated third harmonic, the former term renders the polarization to be intensity-dependent, thereby inducing an index change Δn [28]

$$\Delta n = n_2 I(\boldsymbol{r},t) = \frac{3}{2n_0^2\varepsilon_0 c}\chi^{(3)} I(\boldsymbol{r},t)\,, \tag{1.19}$$

where n_0 represents the linear refractive index and n_2 the nonlinear refractive index. Hence, the combined refractive index under strong intensities $I(\boldsymbol{r},t)$ can be written as

$$n(I(\boldsymbol{r},t)) = n_0 + n_2 I(\boldsymbol{r},t)\,. \tag{1.20}$$

The intensity-dependence of the refractive index and hence the nonlinear response of the medium is referred to as the all-optical Kerr effect [28]. In the time domain, the Kerr effect induces self-phase

modulation (SPM), which is proportional to the length L of the media

$$\phi_{\mathrm{nl}}(t) = -n_2 I(t) \frac{\omega}{c} L. \tag{1.21}$$

As a result of Eq. 1.21, new frequencies are generated. Besides this self-phase modulation, the spatial intensity distribution of a laser pulse leads to self-focusing within a Kerr medium. Both nonlinear effects are further discussed in the upcoming section 1.1.3.

1.1.3 The Formation of a Filament

As mentioned earlier, the third-order nonlinearity plays a key role in the broadening process of the incident spectrum. Limiting the discussion to only positive n_2, a spatial Gaussian intensity profile leads to an intensity-dependent refractive index change that is stronger at the center of the pulse, which effectively increases the optical path in the center. This can be described as a tilt of the phase front of the laser beam comparable to the propagation through a focusing lens and results in self-focusing, which is arrested by plasma generation and linear diffraction. Neglecting at first the plasma generation for the sake of simplicity, linear diffraction can only be surpassed if the increasing intensity leads to an even stronger decreasing beam waist. However, this is not the case as diffraction is strengthened. Hence, to overcome linear diffraction and enable self-focusing to dominate, the beam waist needs to stay constant while the intensity is increased. Thus increasing power, not intensity is required to overcome linear diffraction. The necessary power to overcome diffraction by employing a continuous-wave laser is termed the critical power P_{crit} [35, 36]

$$P_{\mathrm{crit}} = \frac{3.77\lambda^2}{8\pi n_0 n_2}, \tag{1.22}$$

where λ is the central wavelength. The effective self-focusing length for a collimated laser beam is expressed by the equation [35]

$$z_{\mathrm{sf}} = \frac{0.367 z_0}{\sqrt{(\sqrt{\frac{P_{\mathrm{in}}}{P_{\mathrm{crit}}}} - 0.852)^2 - 0.0219}}, \tag{1.23}$$

where $z_0 = \pi n_0 w_r^2/\lambda$ is the Rayleigh length of the initial laser beam. Once self-focusing is increasing the intensity I within a dielectric media strongly, the generation of free electrons becomes increasingly relevant. Ultimately, at high enough intensities, this plasma generation leads to a balancing of both processes, in which the pulse experiences regions of focusing and subsequently, a region of plasma-induced defocussing, followed again by self-focusing. This results in the formation of a stable filament when the following condition is fulfilled

$$n_2 I = \frac{q_e^2}{\omega_p^2 m_e \varepsilon_0} N_e, \tag{1.24}$$

where ω_p is the plasma frequency, m_e the electron mass and N_e the electron density. The negative contribution of the intensity-dependent refractive index is then canceled out if the electron density N_e within the plasma reaches 10^{17} - 10^{18} cm^{-3} [37]. The highest intensity for a stable filament is given by

the clamping intensity [26, 38]

$$I_{\text{clamp}} = \frac{\tau_p N_{nt} W(I_{\text{clamp}})}{2 N_c n_0 n_2}, \tag{1.25}$$

where τ_p is the pulse duration, W the ionization rate, and N_{nt} and N_c are the neutral and critical electron densities, respectively. Plasma generation causes photon loss and hence, after several periods of balanced propagation, the pulse power drops below P_{crit} and diffraction dominates over the nonlinear effects. During filamentation, spectral broadening is enabled due to a combination of various nonlinear processes such as self-phase modulation (SPM), plasma generation and four-wave mixing. In gases, the nonlinearity n_2 is about a thousand times smaller as compared to in solids, which leads to a critical power that is around three orders of magnitude higher. However, due to an additional thousandfold increase of the ionization rate W [39], which leads to a decrease in required intensities to balance self-focusing in solids relative to gases, the clamping intensity in both is roughly equal and in the order of 10^{13} to 10^{14} W/cm^2. Nevertheless, pulses with mJ pulse energy can be employed for filamentation in gases, while energies are limited to hundreds of nJ in solids as the filament diameter is drastically increased in the former [37, 40]. If the power is increased multiple times beyond the critical power P_{crit}, modulation instability begins to dominate, which leads to pulse breakup and multi-filamentation. Modulation instability describes the strengthened nonlinearly intensification of small disturbances [41] that ultimately lead to pulse breakup and the opening of new filaments when the input power exceeds the critical power many times over. The resulting far-field that consists of the interference of several filaments is termed multi-filamentation.

In this thesis, however, only the single filament case is further discussed, in which a continuous, typically polarization-maintaining and coherent octave-spanning spectrum can be generated. The interested reader is referred to [42, 43] for further details on multi-filamentation. Having discussed the fundamentals of pulse propagation through dielectric media, the self-induced spectral extension is illuminated by discussing four different models in the next part. These models will be of interest for evaluating the influence of the spectral broadening mechanisms on the measurement of the CEP.

1.2 Theory of Supercontinuum Generation

Previously, the interaction of a pulse with dielectric media that results in the formation of a filament has been discussed. In this way, guided propagation of laser pulses can be achieved, which enables a severe increase in intensity over large distances and thereby allows a strong contribution of the nonlinearity over time. Then, spectral extension is achieved that can exceed one octave, which is termed supercontinuum generation (SCG). As supercontinuum generation is a prerequisite for most CEP detection schemes, a detailed discussion provides the basis for the later presented analysis. Since spectral broadening can be achieved in various ways, it is here introduced by four models illuminating the process of spectral extension from different angles.

1.2.1 Self-Phase Modulation

Self-phase modulation (SPM) is the dominating process that induces the generation of new frequency components in the presence of a steep intensity profile especially during the propagation through optical fibers [44]. On-axis propagation of a laser pulse with intensity profile $I(z,t)$ and central frequency ω_c

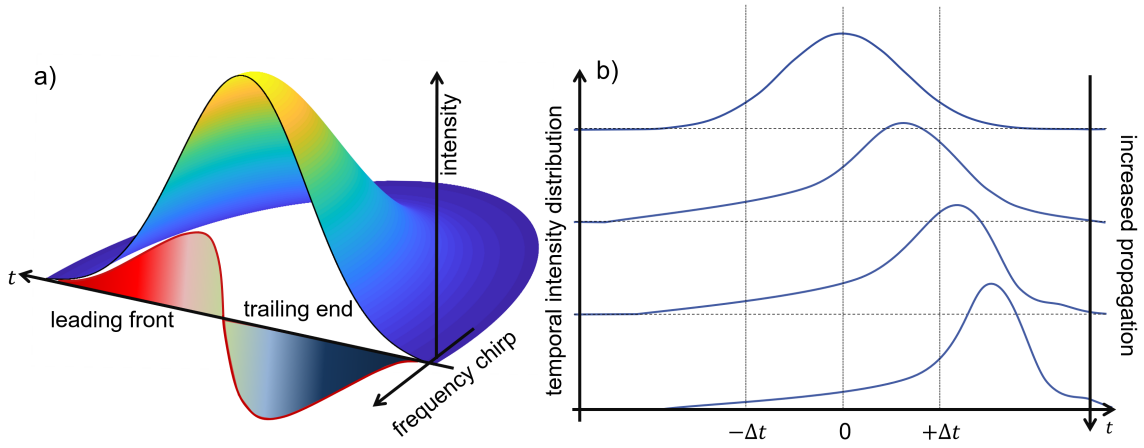

Figure 1.1: Nonlinear effects acting on the pulse. a) Gaussian intensity distribution and resulting symmetrical broadening induced by SPM with longer wavelengths at the front and shorter wavelengths at the back of the pulse. b) Sketch following [47] of self-steepening acting on the pulse with increased propagation through a third-order nonlinear medium. The peak is shifted to the back, while the front slope is flattened. With SPM depending on the slope, the spectrum is far more extended to short wavelengths than longer ones.

through a medium of length L results in the accumulation of nonlinear phase similar to Eq. 1.21

$$\phi_{\mathrm{nl}}(t) = \int_0^L n_2 I(z,t) \frac{\omega_c}{c} dz \quad , \tag{1.26}$$

while the extrema of this accumulation give rise to the spectral extent

$$\Delta\omega_{\pm} = \left(-\frac{\partial \phi_{\mathrm{nl}}}{\partial t} \right)_{\mathrm{max/min}} , \tag{1.27}$$

where $\Delta\omega_+$ ($\Delta\omega_-$) determines the maximum rate of decrease (increase) of nonlinear phase and hence spectral extent. As can be seen in Eq. 1.27 and is illustrated in Figure 1.1 a) red-shifted new frequencies are generated on the leading edge, while the trailing, decreasing intensity profile leads to a blue-shifted extension. In simulations carried out employing a simple SPM theory [45, 46], where the symmetric intensity envelope is assumed to stay constant while propagating, a nearly symmetric spectral extension to the Stokes and anti-Stokes side is present as shown in Fig. 1.2 a).

In a precise description of SPM by Yang et al. [48], where plasma generation is neglected and a hyperbolic secant input pulse is employed $E_0(\mathbf{r},\tau) = E_0(\mathbf{r})\ \mathrm{sech}(t/\tau_0)$, the spectral broadening can be described by

$$\frac{\Delta\omega_{\pm}}{\omega_0} = \frac{1}{2}\left(\sqrt{Q^2+4} \pm |Q| \right) - 1 , \tag{1.28}$$

where $Q = 2n_2 IL/(c\tau_0)$, τ_0 the pulse duration and I the intensity. For $Q \ll 1$, this converges to symmetric spectral broadening, while for $Q \gg 1$ asymmetric broadening is present. Implementing self-steepening leads to a much stronger asymmetry in closer approximation with the experimental observation. Self-steepening is a result of the intensity-dependent refractive index, effectively reducing the group velocity at the peak of the pulse, while the front and trailing part of the pulse are only weakly affected, which results in a deformation where the trailing part catches up with the center of the intensity profile. In a

normal dispersive regime, this leads to a slowly increasing envelope that abruptly rolls off after the peak as is sketched in Fig. 1.1 b). In combination with strong space-time focusing, the abrupt roll-off of the intensity within the timescale of an optical cycle at the back-end of the pulse leads to an experimentally seen blue pedestal, even without considering any plasma contributions. This is referred to as the formation of an optical shock [49, 50]. It is observed that the shock formation needs to precede plasma generation to enable supercontinuum generation. However, for a proper modeling of experimental results from filament-based spectral broadening, plasma generation needs to be taken into account as it arrests self-focusing. This is of particular relevance in the context of limitations for spectral broadening, where, e.g., a band gap E_g dependence of the onset threshold for SCG relative to the energy of the photon E_{ph} can be observed, i.e., $E_{\mathrm{g}}/E_{\mathrm{ph}} \geq 3$. Hence, if the band gap is too small, self-focusing is arrested too early by plasma generation prior to the formation of the optical shock and the filament. Moreover, the high frequency cut-off of the generated spectrum also depends on the band gap of the material [50, 51, 52]. In order to explain these effects, a more sophisticated view on spectral broadening via filamentation is required.

1.2.2 Plasma-Dominated Spectral Broadening

Within a filament that is formed by a laser pulse with pulse powers above P_{crit} and below optical breakdown, self-focusing is arrested by plasma formation and linear diffraction. The former, plasma formation, is a result of the ionization dynamics within the media, which are either caused by multi-photon excitation or tunnel ionization. Both ionization mechanisms essentially describe two limiting cases of the process of ionization, while the dominating mechanism depends on the laser pulse and material characteristics. In this work, the models employed are essentially in the multi-photon excitation regime that can be explained by a perturbative approach.

In the upcoming part, the photoionization by intense fields from a general perspective is briefly introduced, which is followed by a first approach to model plasma generation using a N-th order multi-photon process in combination with Drude theory. Then, a more precise description of ultra-short pulse propagation through media with $\chi^{(3)}$ nonlinearity is provided that employs the nonlinear envelope equation (NEE).

Photoionization in Intense Fields

As filamentation requires the formation of a plasma to counteract self-focusing, there is a strong need to understand the ionization dynamics of atoms and molecules in intense laser fields. While the precise ionization probability of atoms is calculated solving the time-dependent Schrödinger equation, this approach is numerically challenging and simple analytic solutions are preferred. First efforts in this direction were undertaken by Keldysh [53], who, starting from first-oder perturbation theory, developed a photoionization rate for hydrogenic atomic systems in their electronic ground state without considering Coulomb interaction of the freed electron and residual ion [26]. From the photoionization rate, Keldysh was able to deduct a parameter γ that allowed separation of the ionization scenario into the tunnel ionization regime for $\gamma \ll 1$ and the multi-photon ionization (MPI) regime $\gamma \gg 1$. Later referred to as the

Keldysh parameter, it can be expressed as

$$\gamma = \omega \frac{\sqrt{2m_e U_i}}{|q|E_p}, \tag{1.29}$$

where m_e and q are the electron mass and charge, respectively. The ionization potential of the atom is given by U_i, while $E_p = \omega/q\sqrt{U_p 4m_e}$ describes the electric field within which the freed electron oscillates and where it holds a ponderomotive potential U_p. Essentially, the Keldysh parameter separates two limiting cases of the ionization process. It can also be expressed as the ratio of the tunneling time of the electron across the potential barrier of the atom and the oscillation period of the laser field. Since filamentation is limited by a clamping intensity in the order of 10^{13} W/cm^2, this leads to a Keldysh parameter at 800 nm central wavelength, e.g., for xenon in the range of $\gamma_{\mathrm{Xe}} = 3.2$. For solids, the ionization potential can be exchanged by the band gap [54], i.e., $\gamma = \sqrt{E_g/2U_p}$. Thus, e.g., under the same conditions as above for xenon a Keldysh parameter for sapphire of $\gamma_{\mathrm{Sa}} \approx 2.87$ is reached. Therefore, further discussion is limited to the multi-photon regime.

Considering the extreme multi-photon excitation scenario, where $\gamma \to \infty$, it is possible to express the ionization rate W by [26]

$$W_K = \sigma_K I^K, \text{where} \tag{1.30}$$

$$\sigma_K = 4\sqrt{2}\omega \left(\frac{U_i}{\hbar\omega}\right)^{2K+3/2} \frac{e^{2K-U_i/(\hbar\omega)}}{E_0^{2K}} \Phi_0\left(\sqrt{2K - \frac{2U_i}{\hbar\omega}}\right), \tag{1.31}$$

with σ_K the photoionization cross-section, $\Phi_m(x) = e^{-x^2}\int_0^x (x^2-y^2)^{|m|} e^{y^2}\mathrm{d}y$ and,
$K = \mathrm{mod}(U_i/\hbar\omega) + 1$ the number of photons simultaneously absorbed to liberate an electron. For simplicity, atomic units (a.u.) are used within this part, where $m_e = \hbar = q = 1$[26]. Conversion of the cross-section to SI units $s^{-1}cm^{2K}/W^K$ is carried out by $\sigma^{(K)} = \sigma_K[\text{a.u.}]/[2.42\times10^{-17}\times(3.51\times10^{16})^K]$. An experimental approximation is given later in Eq. 1.36.

While the Keldysh theory enables an approximative description of photoionization in solids and liquids, for gaseous media another theory developed by Perelomov, Popov and Terent'ev (PPT) is commonly employed. The PPT model allows to consider any atomic state as possible initial state and also includes the Coulomb interaction. The ionization rate given by the PPT theory reads as

$$\begin{aligned} W = \frac{4\sqrt{2}}{\pi}|C_{n^*,l^*}|^2 \frac{f(l,m)}{|m|!} U_i = \left(\frac{2E_0}{E_p g}\right)^{2n^*-3/2-|m|} \exp[-2\nu(\sinh^{-1}(\gamma) - \frac{\gamma g}{1+2\gamma^2})] \\ \times \quad U_i \frac{\gamma^2}{g^2} \sum_{\kappa\geq\nu_0}^{+\infty} \exp[-\alpha(\kappa-\nu)]\Phi_m(\sqrt{\beta(\kappa-\nu)}), \end{aligned} \tag{1.32}$$

where $g = \sqrt{1+\gamma^2}$ and Z the residual ion charge. With l, m the orbital angular momentum and the magnetic quantum number, respectively, the effective quantum number $n^* = Z/\sqrt{2U_i}$ and $l^* = n^* - 1$ the effective orbital quantum number can be given. The initial atomic state influences the ionization rate via

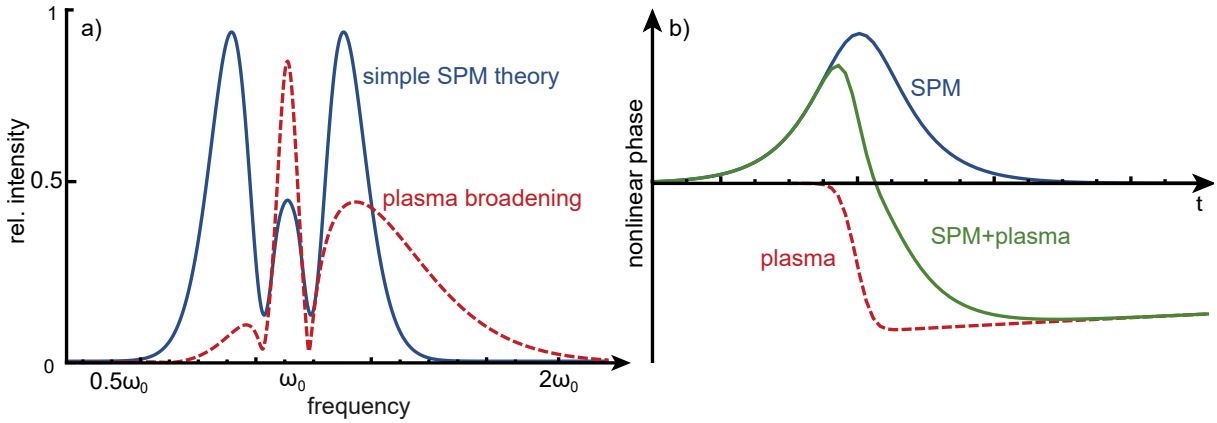

Figure 1.2: Simulated SPM-dominated and plasma-dominated broadening with the resulting spectral extension in a) and the nonlinear phase shift in b). Relaxation dynamics are not included.

C_{n^*,l^*} and $f(l,m)$, which can be written as

$$|C_{n^*,l^*}| = \frac{2^{2n^*}}{n\Gamma(n^*+l^*+1)\Gamma(n^*-l^*)}, \tag{1.33}$$

$$f(l,m) = \frac{(2l+1)(l+|m|)!}{2^{|m|}|m|!(l-|m|)!}. \tag{1.34}$$

With the possibility of considering an arbitrary initial state of the atom and including Coulomb interaction, description of a broader range of atoms and their interaction with light is possible. Despite proper description of the photoionization of atoms in both extreme regions of the Keldysh parameter, discrepancies are found to experimental observations when it comes to more complex atomic and molecular systems, especially in the tunneling regime. For $\gamma \ll 1$, the Ammosov, Delone and Krainov (ADK) model [55] is often used for complex systems. A more rigorous description and deduction of the ionization rate of the PPT and ADK models can be found in [26, 56, 57, 58]. Nevertheless, despite being limited to hydrogen-like atoms and neglecting the Coulomb interaction of the freed electron and ion, the Keldysh theory is very well suited to describe photoionization in the MPI regime, which is made use of in the upcoming section.

Multi-Photon Ionization Dominated Spectral Broadening

In the multi-photon regime, i.e., when $\gamma \gg 1$, the ionization rate is found to scale according to Equation 1.30 for a $K = \mathrm{mod}(E_g/\hbar\omega)$-th order absorption process with a minimum required number of photons K to overcome the band gap $E_g \leq K\hbar\omega$.

Starting from the wave equation 1.1, which includes a current density $\mathbf{J} = qN_e v_e$ [26], with v_e the electron velocity and N_e the electron density, temporal dynamics of the electron density can be described by including the photoionization and relaxation process. A rate equation is given by [59]

$$\frac{dN_e(t)}{dt} = \alpha N_e(t)\zeta I(t) + \beta_K[\zeta I(t)]^K - \frac{N_e(t)}{T}, \tag{1.35}$$

where $I(t)$ is the pulse intensity, $N_e(t)$ the time-dependent electron density, α the avalanche coefficient, β_K the K-th order multi-photon absorption coefficient and T the effective relaxation time. ζ gives the

ratio of the maximum internal to incident intensity [60, 61]. The right-hand side of the rate equation from left to right consists of a term describing avalanche photoionization, a multi-photon excitation term and lastly, a relaxation term. The contribution of the latter is typically of negligible importance in gases when considering ultra-short pulses, as the time scale is in the order of nanoseconds [26]. However, in solids, this timescale can vary strongly, but has been observed to be typically above 50 fs [26, 59]. This results in a slow linear decrease of the freed electrons if ultra-short pulses of 10 fs duration are used. In silica and sapphire, the effective decay time is around 220 fs [59]. While for picosecond pulses, relatively slow avalanche ionization is found to strongly enhance SPM on the anti-Stokes side [62, 63], for femtosecond pulses free-electron generation must be dominated by a much faster process such as multi-photon ionization [53, 64, 65]. In order to cancel the Kerr effect, electron densities of 10^{17} to $10^{18}\,\mathrm{cm}^{-3}$ are required. These electron densities are not easily reached by means of avalanche ionization for ultra-short pulses as electron densities are only doubled after roughly 50 fs at intensities of 10^{13} W/cm^2. Therefore, the initial contribution of avalanche ionization to femtosecond pulse-induced plasma generation is small. Nevertheless, this contribution can be substantially higher after electrons have been freed by MPI and subsequently accelerated by the intense laser field [37, 52, 62, 65]. In the case of sapphire and silica, α is $12\,\mathrm{cm}^2$/J and $8\,\mathrm{cm}^2$/J, respectively. However, the actual contribution was shown to be small far away from the damage threshold [66]. MPI on the other hand has a rise time that is comparable to the pulse duration and will directly affect the pulse. It depends on the multi-photon absorption rate that is calculated by the Keldysh or PPT theory, and therefore on the atom to be ionized. Although the Keldysh theory is limited to hydrogen-like atoms and excludes Coulomb interaction of the ion and the freed electron, by adapting the reduced effective mass[2] m_r of the electron [59] the experimentally found results agree well within the MPI regime in crystals with the multi-photon absorption (MPA) coefficient

$$\beta_K \approx \frac{\omega}{9\pi}\left(\frac{m_r\omega}{\hbar}\right)^{3/2}\left(\frac{q^2}{8\omega^2 m_r c\varepsilon_0}\right)^K \frac{\exp(2K)}{(n_0 E_g)^K}\,. \tag{1.36}$$

Making use of the Drude model of a collisionless plasma, the plasma-induced change of the refractive index for a neutral refractive index n_0 is given by

$$n = \sqrt{n_0^2 - \frac{\omega_p^2}{\omega^2}}, \tag{1.37}$$

where $\omega_p = q\sqrt{\frac{\rho}{\varepsilon_0 m_e}}$ is the plasma frequency at a plasma or electron density $\rho = N_e$. In the case of $\rho \ll \rho_c$ with $\rho_c = \omega^2 m_\mathrm{e}\varepsilon_0/q^2$ the critical plasma density, the isolated refractive index change can be approximated to $\Delta n = \frac{\rho}{2n_0^2\rho_c}$. As the nonlinear phase is additionally modulated by the contribution of the plasma via $\Delta\phi_\mathrm{nl} = 2\pi\Delta n/\lambda$, which is building up during the pulse propagation, especially at the end of the pulse a sharp drop of the nonlinear phase is present as can be seen in Fig. 1.2 b). In turn, this leads to a strong blue-shift of the resulting spectrum as is shown in Fig. 1.2 a). Here, it is calculated exemplary for a secant hyperbolic input pulse profile in the case of sapphire [59, 67].

[2]The reduced effective mass of the electron or any other particle enables to describe the way it responses to forces. For example, the effective mass of the electron allows a simplified description of the electrons response within the band structure, where the effective mass depends on the material.

1.2.3 (2D+1) Model of Supercontinuum Generation

For a detailed and precise description of the supercontinuum process involving dispersive effects, self-steepening, self-phase modulation, plasma generation and other spatial effects, the nonlinear envelope equation (NEE) can be used. It can be deduced from the wave equation [56]. The NEE requires the paraxial approximation ($k_\perp \leq |\boldsymbol{k}|$) to be valid and requires an angular spread with a numerical aperture (NA) of approximately 0.1 or less. Equivalently, an angle acceptance cone of only a few degrees around the propagation direction is required, which is typically fulfilled in a filament.

Hence, few-cycle pulses and their interaction with media can be appropriately described under the conditions found in a filament [56]. The nonlinear envelope equation [29, 56, 68] relates the envelope $\mathcal{E}$ of the electric field to the plasma density ρ and third-order nonlinear effects by means of

$$\begin{aligned}\partial_z \mathcal{E} = \frac{i}{2k_0} T_o^{-1} \Delta_\perp \mathcal{E} + i\mathcal{D}\mathcal{E} + i\frac{\omega_0}{c} n_2 T_o |\mathcal{E}|^2 \mathcal{E} - i\frac{k_0}{2\rho_c} T_o^{-1} \rho \mathcal{E} \\ - \frac{\sigma}{2}\rho\mathcal{E} - \frac{U_i W(I)(\rho_{nt} - \rho)}{2I}\mathcal{E}, \qquad (1.38)\end{aligned}$$

$$\partial_t \rho = W(I)(\rho_{nt} - \rho) + \frac{\sigma}{U_i}\rho I, \qquad (1.39)$$

with $I = |\mathcal{E}|^2$ the averaged field intensity and U_i the ionization potential. The first term on the right-hand side of Eq. 1.38 handles diffraction. This includes space-time focusing implemented in front of the diffraction term $\Delta_\perp$ by the $T_o = 1 + (i/\omega_0)\partial_t$ operator, which acts in the frequency domain. While diffraction naturally includes wavelength dependency, resulting in shorter wavelengths being less diffracted than longer ones, this effectively leads to a narrowing of the on-axis spectrum and thereby creating temporal pulse broadening. The second term includes the dispersion of the temporal pulse profile by means of the operator

$$\mathcal{D}(\omega) = \sum_{m=2}^{\infty} \frac{1}{m!} \beta_m \left(\frac{\partial}{\partial t}\right)^m, \qquad (1.40)$$

where β_m relates to Eq. 1.8. Furthermore, the third term in Eq. 1.38 includes the intensity dependence of the refractive index, which was previously introduced as the Kerr effect. Assuming a positive nonlinear index n_2, this term provides self-steepening on the pulse through the operator T_o [49] in combination with SPM on the phase. Together, this enables the asymmetric broadening characteristically found in dielectric media. The fourth term takes into consideration the phase change induced by the free-electron plasma that is generated in a filament. While the first four terms include an imaginary part that enables to act upon the phase, the latter two include responses of the pulse to environmental changes due to photon absorption. With the fifth term describing photon losses caused by free electrons accelerated in the laser field, the sixth term relates the photon loss due to multi-photon absorption with the rate $W(I)$. Equation 1.39 describes the temporal evolution of the plasma density in form of a rate equation, where the first term accounts for photo-ionization, while the second includes avalanche ionization by means of the cross-section σ and U_i the ionization potential.

The next section will introduce the concept of mode-locking, which is essential for enabling pulses within the 10 fs regime.

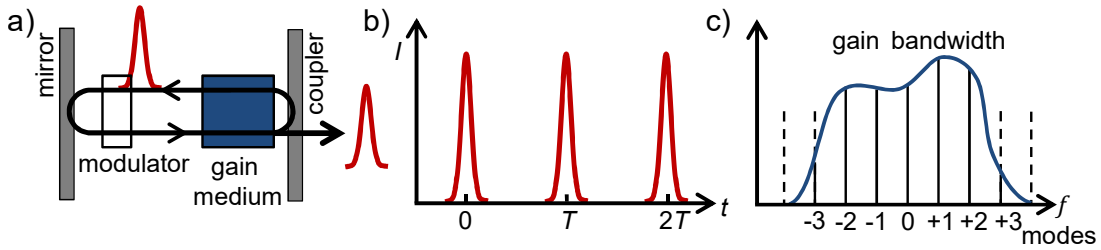

Figure 1.3: a) Sketch of a cavity for the illustration of active mode-locking. b) Sketched output pulses of a mode-locked laser and c), the gain bandwidth in combination with longitudinal resonator modes in the spectral domain.

1.3 Principles of Mode-Locked Lasers

Not long after the invention of the laser by Maiman et al. [69] in 1960, the discovery of mode-locking [70, 71] and its continuous optimization let to the generation of ultra-short pulses with durations well within the femtosecond regime. The realization of phase-locking is introduced for different lasing situations, which provide the basis for the investigation of the intra-cavity noise formation mechanisms in chapter 2.

1.3.1 Mode-Locking

Mode-locking is based on the phase-locking of different longitudinal cavity modes f_m

$$f_m = f_{\mathrm{CE}} + \frac{mc}{2n_0 L}, \tag{1.41}$$

where m is the mode integer as is sketched in Figure 1.3 c), c the vacuum speed of light, n_0 the refractive index and L the length of the cavity. The frequencies of all cavity modes are offset by the carrier-envelope offset frequency f_{CE}, which will be explained in more detail later. During mode-locking, a fixed relationship between the phases of all lasing modes is established that allows constructive interference. This enables the formation of pulses within the cavity for a multiple of the pulse round-trip time $T_R = L/c$. When the spectral phase of each mode is additionally nearly identical to the phases of their neighboring modes, Fourier-limited pulse generation is achieved. In this case, the time-bandwidth product for, e.g., sech^2-shaped pulses, $\Delta\tau \cdot \Delta f \geq 0.32$ is at its minimum, which leads to the shortest possible pulse duration τ for a particular bandwidth. Thus, increasing the spectral bandwidth Δf of a pulse renders it potentially shorter, if the condition of a flat spectral phase is met. To achieve pulse durations within the femtosecond regime with common repetition rates ranging from tens of MHz down to several GHz, mode-locking of THz wide spectra and therefore between hundreds and millions of different longitudinal modes is required, respectively. Such a high degree of correlation between the phases of the mode-locked modes can be achieved by means of active or passive techniques.

Active mode-locking is typically realized by amplitude modulation (AM) of the intra-cavity field with a periodicy equal to the round-trip time. A simple laser design to achieve mode-locking is shown in Fig. 1.3 a). The modulation can be achieved by, e.g., an acousto-optic or electro-optic modulator, which results in the generation of sidebands located at the position of the neighboring longitudinal modes (see 1.3 c)). Then, a correlation is established between the phases of neighboring modes that is also referred to as injection lock. This processes cascades through the full gain bandwidth of the gain medium and

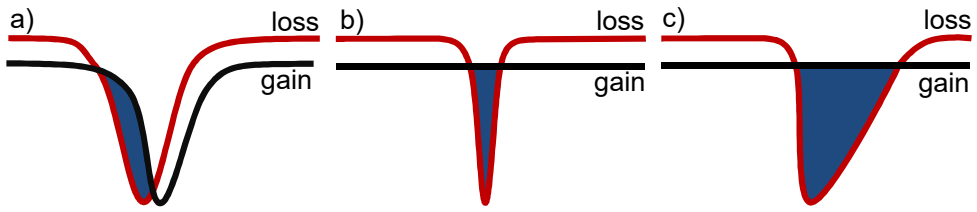

Figure 1.4: Three fundamental passive mode-locking models over time with indicated (blue) net gain window. a) Slow absorber and dynamic gain saturation, b) fast absorber and constant gain, and c) soliton mode-locking.

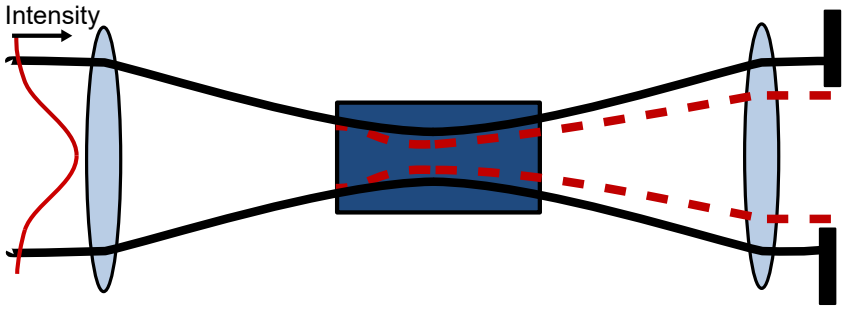

Figure 1.5: Principle of the Kerr lens acting as a saturable absorber.

effectively couples modes to form an equally-spaced frequency comb. In the time domain, this frequency comb translates to a pulse train as is depicted in Fig. 1.3 b).

Today, passive mode-locking is almost exclusively used, where the pulse inflicts the modulation onto itself. This self-amplitude modulation (SAM) can be realized by a nonlinear process. To this end, a saturable absorber is typically employed within the cavity. Three different passive mode-locking situations can be distinguished, where the response time of the saturable absorber (SA) as well as the gain saturation dynamics are considered. Saturable absorbers are introduced to favor strong intensities by reducing loss for higher intensity. They were used in the first realization of passive mode-locking in 1966 based on a dye solution [72], which functions as a slow absorber as well as a dynamic gain source. Thereby, the gain and loss are balanced and a steady-state net gain window forms that can be as short as the pulse duration. This is illustrated in Fig. 1.4 a) and has enabled pulses as short as 27 fs [73].

The second model, shown in Fig. 1.4 b), is based on a very fast saturable absorber with a steady gain as is found in most solid-state lasers with long upper-state lifetime. With the fast bleaching of the SA, a net gain window forms. In order to achieve ultra-short pulses within the lower femtosecond regime only artificial saturable absorbers such as the Kerr lens are available, which, for example, can be directly used within the laser host material Ti:sapphire. Based on the third-order susceptibility, the Kerr effect leads to self-focusing of the dominating intensity part of the pulse, which, in combination with an aperture, enables to filter out low intensities at the wings of the pulse that are less focused. Therefore, self-amplitude modulation is achieved by favoring intensity spikes that experience less attenuation. This is shown in Fig. 1.5. One main advantage of the Kerr lens is the quasi-instantaneous response of the Kerr effect, which has been found to be less than a femtosecond [74]. For achieving ever shorter pulse durations, the dispersion management within the cavity is found crucial. To this end, the balance of nonlinear self-phase modulation (SPM) and a net negative group delay dispersion (GDD) is an important step to maintain self-stabilizing soliton[3]-like pulses after every round-trip [75, 76]. Traditionally, this

[3]Solitons are pulses that can propagate without being temporally stretched due to the counteracting effect of a balanced SPM and GVD.

was achieved by introducing dispersive elements such as prisms or gratings into the cavity. Nowadays, chirped mirrors [77] are commonly employed that enable the generation of pulses straight out of the cavity from a KLM-based Ti:sapphire oscillator of only 4.4 fs [78] in duration.

However, to obtain ultra-short pulses, the response time of the SA does not need to be on the same timescale as the achievable pulse duration. This is depicted in Fig. 1.4 c) and referred to as soliton mode-locking, where the balancing of SPM and negative GDD controls almost all dynamics of the pulse and its duration depends almost solely on this balance. A semiconductor saturable absorber mirror (SESAM) is normally introduced into the cavity for stabilization and starting the mode-lock. Nevertheless, the actual net gain window can be multiple times larger as the pulse duration. The SESAM only suppresses the continuum that is accumulated due to parasitic losses of the soliton. A SESAM is based on the excitation of electrons from the valence to the conduction band that results in an increased reflectivity and enables the formation of a net gain window. Important parameters of SESAMs are the recovery time τ_A, the modulation depth ΔR, saturation intensity I_{sat} and saturation fluence F_{sat}.

1.3.2 Artificial Saturable Absorber

Many variants of artificial fast saturable absorbers have been employed so far. Besides the Kerr lens in Ti:sapphire lasers, especially additive-pulse mode-locking [79, 80] is well known for bulk lasers, where an additional cavity formed by a single-mode fiber is used to achieve an artificial SA via nonlinear phase shifts. The additional single-mode fiber is coupled to the bulk medium cavity by a semi-transparent mirror. Due to the differently acquired nonlinear phase shift of a pulse propagating in the single-mode fiber and in the cavity, the interference at the semi-transparent mirror can be tuned to attenuate the wings and constructively interfere with the peak of the pulse.

Similar mode-locking approaches have been realized for fiber lasers, where mode-locking is achieved by employing nonlinear polarization rotation (NPR) [81, 82], a nonlinear optical loop mirror (NOLM) [83] or a nonlinear amplifier mirror (NALM) [84]. The former, nonlinear polarization rotation is shown for a ring cavity using an Er:doped fiber in Figure 1.6 a). During most of the propagation through the cavity, the orthogonal components of the elliptically polarized light experience different refractive indexes as a result of SPM and cross-phase modulation (XPM)[4]. Then, pulsed compared to CW light enters at a different polarization in the second polarizer, effectively establishing losses for the CW component, while an additional isolator ensures unidirectional propagation. The latter two optical switching devices based on a NOLM or NALM make use of nonlinear phase shifts of counter-propagating pulses in a second loop connected via a four port coupler. A NOLM utilizes a slightly asymmetric power-coupling ratio of close to 50:50, where a pulse entering in port 1 is split into two counter-propagating parts in the NOLM exiting port 3 and 4 as is sketched for a NALM in Fig. 1.6 b). Linearly, the optical paths are identical and constructive interference back at the coupler is present, which results in a mirroring of the incident pulse out of port 1. However, if nonlinear effects are included and the splitting ratio of the coupler is not 50/50, a nonlinear phase shift difference between both counter-propagating pluses occurs, which leads to different interference situations upon return to the coupler. Depending on the accumulated difference in nonlinear phase the pulse is either transmitted into port 2 or mirrored back into port 1. The power-dependent reflectivity is illustrated in Fig. 1.7. An optical isolator ensures unidirectional propaga-

[4] Cross-phase modulation describes a nonlinear interaction based on the optical Kerr effect, where the phase of one pulse is altered by the intensity-dependent refractive index change caused by another pulse.

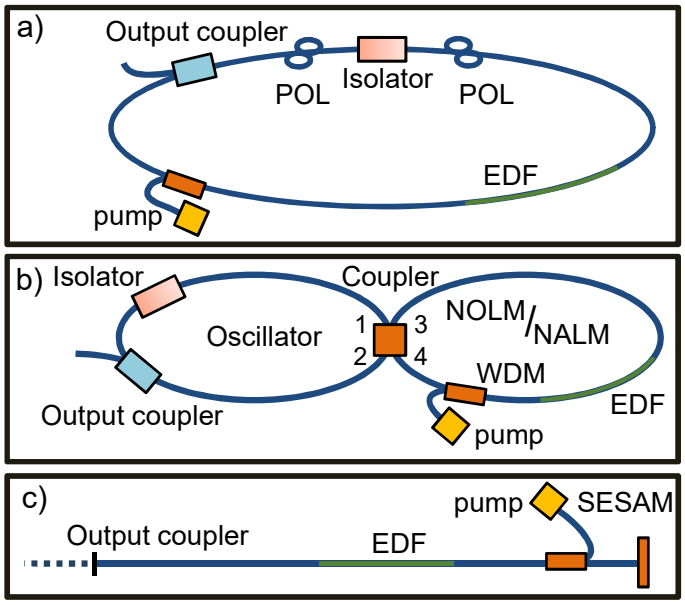

Figure 1.6: Three passive mode-locking schemes employed for fiber lasers are illustrated, which are based on an implemented Er:doped fiber (EDF). a) NPR mode-locking; b) Nonlinear optical loop mirror (NOLM) and nonlinear amplified loop mirror (NALM) mode-locking in a figure-of-eight configuration. Only the latter includes an EDF, a wavelength-division multiplexing device (WDM) as well as a pump. c) Saturable absorber mirror based mode-locking (SESAM). After [85].

tion in the oscillator. Similar to a NOLM, a NALM employs a coupling ratio of precisely 50/50 and the nonlinear phase shift is strengthened by implementing amplification in an erbium-doped fiber (EDF) on one site of the ring which then occurs earlier for one of the counter-propagating pulses. Consequently, the accumulated nonlinear phase differs in either direction, leading to different interference conditions at the coupler.

As shown in Fig. 1.6 c), the third concept involves a linear cavity including a SESAM to provide saturation of the self-amplitude modulation[5]. By introducing intensity-dependent losses, pulses are favored over CW operation. While this work is dominated by the application of Ti:sapphire-based lasers, variants of the presented fiber laser mode-locking designs are employed within the comparative study in chapter 2 to analyze the origin of carrier-envelope phase noise. All of these lasers are essentially based on a fast saturable absorber.

1.3.3 Haus Master Equation of Fast Saturable Absorber Mode-Locking

The intra-cavity evolution of the pulse for a broad range of different mode-locking mechanisms based on saturable absorber mode-locking has been for the first time properly described by the Haus master equation [86]. The equation is based on the assumption of a negative group velocity dispersion and self-phase modulation as is found in Kerr lens mode-locked lasers, soliton-based mode-locking and many other variants of fiber lasers based on a NOLM or NPR. To this end, the Master equation describes the adiabatic nonlinear pulse evolution as a function of essentially two time scales, a slowly-varying time scale over many round-trips T_l and a fast time scale t. The equation reads

[5]Self-amplitude modulation summarizes the combined effect within a laser cavity of dispersion and nonlinear interaction that act upon the pulse. In lasers with a slow response time to external perturbations, such as media with high upper-state lifetime, it is necessary to saturate this self-amplitude modulation to achieve stable operation against perturbations.

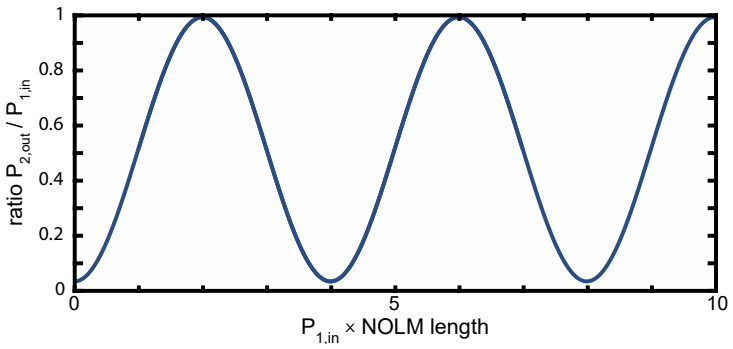

Figure 1.7: Sketched power-dependent reflectivity of a NOLM. Output at port 2 depends on the input strength at port 1 and the length of the NOLM. Here, the case of slightly asymmetric coupling to port 3 and 4 is sketched.

$$T_R \frac{\partial}{\partial T_l} A(t,T_l) = \left[-l + g\left(1 - \frac{1}{\Omega_g}\frac{\partial}{\partial t} + \frac{1}{\Omega_g^2}\frac{\partial^2}{\partial t^2}\right) + iD\frac{\partial^2}{\partial t^2} + (\gamma_s - i\delta)|A|^2 \right] A(t,T_l) + T_R S(t,T_l)\,, \tag{1.42}$$

where T_R is the round-trip time, A the electric field amplitude as a function of both time scales, T_l and t, l and g, the incremental loss and gain, respectively, and Ω_g the gain bandwidth related to the gain medium. Further gain terms describe the coupling of the group velocity as well as the finite gain that act as a restoring force, respectively. D relates to the group velocity dispersion. Furthermore, the saturable absorber action and the Kerr phase modulation is included by

$$\gamma_s = \frac{s_0}{I_{\text{sat}} A_{\text{eff}}} \quad \text{and} \tag{1.43}$$

$$\delta = \frac{2\pi}{\lambda A_{\text{eff}}} n_2 L \quad , \tag{1.44}$$

respectively. Here, s_0 describes the unsaturated loss, I_{sat} the saturation intensity of the used absorber, A_{eff} the effective area of the mode and L the length of the interaction. In order to use the original Master equation for estimating the effect of a perturbative noise source, a small perturbation can be introduced by adding the last term $T_R S(t,T_l)$ [87], which is made use of in section 1.5. Nevertheless, the discussion continues without considering noise by describing the steady-state situation. In order to obtain a solution for the Master equation the following conditions are assumed. The case of balancing SPM and GVD is considered, where solitons are formed. Further, a possible chirp is neglected and a phase shift per pass Ψ through the medium proportional to the Kerr lens dependence on the amplitude $\Psi = -\frac{\delta}{2}A_0^2$ is assumed. Then, one obtains a solution of the Master equation that reads

$$A(t,T_l) = A_0 \,\text{sech}\left[\frac{1}{\tau}(t-t_0)\right] \exp\left(-i\frac{\delta}{2}A_0^2\frac{T_l}{T_R} + i\varphi\right) \tag{1.45}$$

$$\tau = \frac{1}{A_0}\sqrt{\frac{2|D|}{\delta}} \quad , \tag{1.46}$$

where φ is the phase of the pulse, which is set to an arbitrary value without the presence of noise. The Master equation enables the analytic analysis of the pulse evolution within various mode-locking laser cavities.

1.4 The Carrier-Envelope Phase

Within the first section 1.1, pulse dynamics in dielectric media were addressed. It was shown in Eq. 1.5 that the temporal evolution of a laser pulse $E(t)$ can be separated in a carrier wave ω_c multiplied by an envelope function $A(t)$, which leads to

$$E(t) = A(t)e^{i(\omega_c t+\varphi_{\mathrm{CE}})} \ , \tag{1.47}$$

where φ_{CE} is the carrier-envelope phase. While the pulse is propagating through the laser cavity, dispersion is acting upon the pulse, leading to the group-phase offset $\Delta\varphi_{\mathrm{GPO}}$ presented in Eq. 1.11. For one full round-trip of length L within the laser cavity, it reads

$$\Delta\varphi_{\mathrm{GPO}} = -\omega_c \int_0^L \left(\frac{1}{v_g} - \frac{1}{v_p}\right) \mathrm{d}z = \frac{\omega_c^2}{c} \int_0^L \left.\frac{\mathrm{d}n(\omega,z)}{\mathrm{d}\omega}\right|_{\omega=\omega_c} \mathrm{d}z \ , \tag{1.48}$$

where $n(\omega,z)$ is the refractive index. The above equation neglects nonlinear contributions within the gain medium. Within a laser cavity main contributors to the dispersion include the mirrors, the path through air and the gain medium itself. In case of a Ti:sapphire laser with a medium of a few millimeter thickness, the dominant dispersion contribution is the crystal's dispersion, resulting in a group-phase offset of several hundred optical cycles [11]. Despite these hundreds of slips of the phase through the envelope that render two successive pulses substantially different in terms of the absolute phase, only changes that are not a full integer of 2π are of interest. Hence, the CEP slippage rate is referred to as

$$\Delta\varphi_{\mathrm{CE}} = \Delta\varphi_{\mathrm{GPO}} \mod 2\pi. \tag{1.49}$$

Since a mode-locked laser emits a periodic train of pulses, the phase difference actually refers to a continuous slippage or drift of the CEP $\Delta\varphi_{\mathrm{CE}}$ that can be related to the carrier-envelope frequency (CEF) f_{CE} via

$$f_{\mathrm{CE}} = f_{\mathrm{rep}} \frac{\Delta\varphi_{\mathrm{CE}}}{2\pi}. \tag{1.50}$$

This is shown in Fig. 1.8 a) for a slippage rate of $\Delta\varphi_{\mathrm{CE}} = \pi/2$, where the electric field change underneath the intensity envelope at the same spatial position for successive pulses is considered. The resulting equally-spaced frequency comb is shown in Fig. 1.8 b). Following Eq.1.41, the frequency comb can be expressed as

$$\nu_m = f_{\mathrm{CE}} + m f_{\mathrm{rep}}, \quad m \in \mathbb{N}, \tag{1.51}$$

where the whole comb is defined by two parameters, the offset f_{CE} and the needle spacing f_{rep}.

Precise measurement of the frequency comb has shown a stability of the comb down to 1 in 10^{-15} [88, 89, 90]. This stability has enabled great progress in the field of frequency metrology, where measurements of frequencies by means of heterodyne techniques have enabled precise time measurement.

The carrier-envelope phase is important for the generation of attosecond pulses [91], where the electric field structure of intense few-cycle driver pulses is influencing spectra [6] that are obtained by high-harmonic generation (HHG). HHG can be described by the three-step model. In the first step, an electron

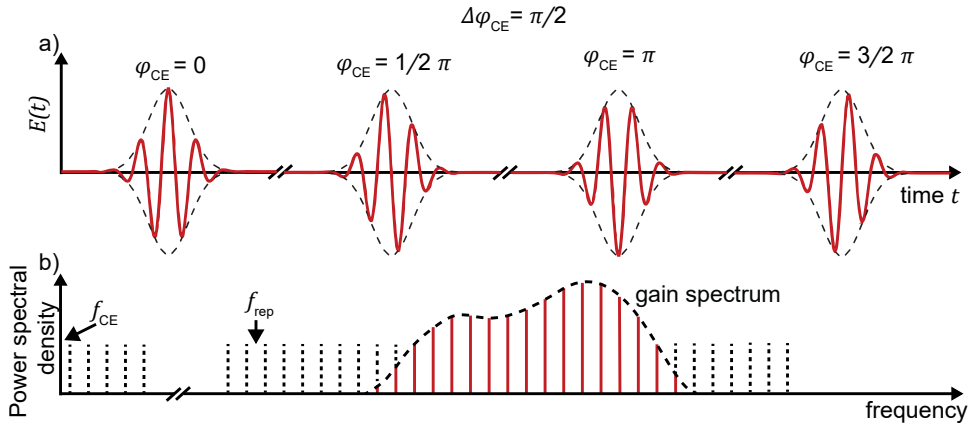

Figure 1.8: a) Time-domain evolution of the electric field $E(t)$ of a few-cycle pulse with a CEP drift of $\Delta\varphi_{\mathrm{CE}} = \pi/2$. b) Corresponding Fourier domain representation. The whole frequency comb is offset by f_{CE}, while also the actual gain spectrum is shown.

is freed by tunnel ionization from, e.g., a noble gas by the intense few-cycle driving pulse that strongly lowers the potential barrier. This occurs every half-cycle around the maxima of the carrier. In the second step, the freed electron is accelerated by the electric field of the driver pulse, while its trajectory depends on the moment of release. Third, after the driving field reverses, the electron can recollide with the parent ion and emit the acquired energy in form of a high energy photon. As a result of this strong dependence on the electric field of the driving pulse, the high-harmonic spectra feature a CEP-dependent structure and are especially sensitive at the cut-off of the harmonics [6].

When isolated attosecond pulses are of interest for, e.g., time-resolved measurements, temporal gating techniques such as polarization gating (PG)[6] [92] or double-optical gating (DOG)[7] [93] are employed to limit HHG to only once per cycle of the driving IR-field.

1.4.1 Measurement

Measurement of the CEP was first realized by Xu et al. [10], who measured the CEP drift between successive pulses by employing cross-correlation of both in a nonlinear interferometer. In this case, the position of the peak within the resulting interference pattern provides access to the change of the CEP. However, precise extraction of the CEP by cross-correlation has been found troublesome as long interferometer arms are required, which renders the pulse strongly susceptible to external noise sources. Hence, this approach has been found too inaccurate to be used within a CE phase-locking scheme for stabilization. Briefly after, a novel approach based on the heterodyning of harmonics obtained via nonlinear processes from parts of an extended pulse spectrum [11, 94] has been proposed and realized. Different variants of this measurement scheme have been developed that are referred to as f-$2f$ [11, 94, 95], 0-f [96] or $2f$-$3f$ [97] interferometry. All these schemes rely on nonlinear frequency conversion, and hence need to preserve the carrier-envelope phase. This condition was shown to be fulfilled and thus access

[6]Polarization gating relies on the interference of two counter-rotating circularly polarized pulses that when slightly overlapped form a region in which linear polarization is present. In this way, a window of a strongly increased ionization probability is formed that can be adapted by adjusting the temporal delay between both pulses. Hence, only one attosecond pulse is generated per cycle, when both pulses are as short as 6 fs.

[7]Double optical gating combines polarization gating with two-color gating. It makes use of a third, second-harmonic field (hence two colors) during window formation that enables to generate isolated attosecond pulses under a relaxed requirement for the employed driving laser pulse duration compared to PG.

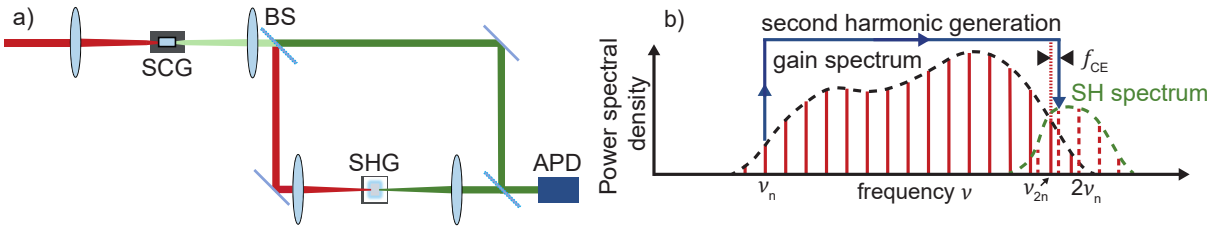

Figure 1.9: Principle of f-$2f$ interferometry. The beat signal is generated by two frequency combs present at the region of overlap of the second harmonic and the fundamental, respectively.

to the CEP was provided by down-conversion of the carrier-envelope frequency to the radio-frequency domain. Furthermore, another approach of this class called balanced homodyne detection [98] provides access to the carrier-envelope frequency f_{CE}.

While most measurements of the CEP rely on nonlinear processes, few detection schemes exist that do not require nonlinear interaction. These are for example based on a slightly off-resonant ring resonators [99, 100]. However, these schemes are rather limited to only MHz precision, which renders proper stabilization impossible. Among the presented CEP detection schemes, f-$2f$ interferometry is the most widely used approach and represents the basis of most CEP stabilization schemes, including the ones employed here. Therefore, this measurement scheme is further discussed in detail.

f-$2f$ Interferometry for Oscillators

In the case of oscillators, the CEP slippage between successive pulses is commonly measured by employing f-$2f$ interferometry. To this end, two nonlinear processes are required. First, spectrally broadening of the incident pulse spectrum is carried out in order to cover at least one octave. Then, subsequent frequency-doubling of the lower energy wing enables interference of two spectral densities. This is shown in Fig. 1.9 b). The interference of two frequency combs that overlap at the higher frequency edge of the spectrum results in a beating that has the difference signal of

$$f_{\mathrm{beat}} = 2\nu_n - \nu_{2n} = 2nf_{\mathrm{rep}} + 2f_{\mathrm{CE}} - (2nf_{\mathrm{rep}} + f_{\mathrm{CE}}) = f_{\mathrm{CE}}\,, \tag{1.52}$$

where ν_{2n} and ν_n represent the comb needles of the frequency comb of the fundamental and adjacent second harmonic, respectively. The latter has an offset of exactly f_{CE} relative to the former as the CEP is doubled during frequency-doubling [20]. Upon interference, the difference results in a radio-frequency amplitude modulation that is readily detected with an avalanche photodiode. The resulting amplitude modulation is shown in Fig. 1.10. Once the signal is Fourier-transformed or visualized by a spectrum analyzer, the rf power spectrum can be observed. In the noise-free case, only the carrier-envelope beat f_{CE}, the repetition rate f_{rep} and their mixing products are present.

The spectral broadening is typically realized by using microstructured fibers or photonic crystal fibers (PCF)[8]. Especially PCF's have been used for oscillators as they require only relatively low input energies, but provide reliable octave-spanning spectrum generation by highly nonlinear interaction. The highly nonlinear interaction is achieved by strong spatial confinement of the beam within a photonic structure

[8] Photonic crystal fibers are a type of optical fibers that rely on refractive index variations by means of an air cladding structure to guide and confine laser pulses. Their design enables strong confinement and hence high intensities of even weak pulses as well as the tailoring of the zero-dispersion wavelength, at which the group delay dispersion is zero.

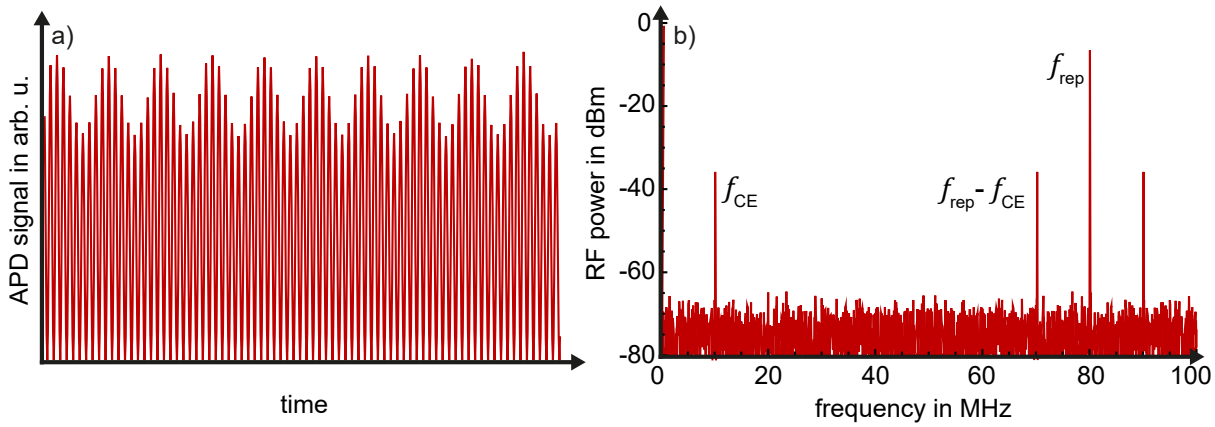

Figure 1.10: a) Simulated amplitude modulation at the back-end of the f-$2f$ interferometer. b) Corresponding power spectrum that shows the frequency of the beating f_{CE}, the pulse repetition frequency f_{rep} and their mixing products.

despite low pulse energies. Additionally, PCF's enable tailoring of the zero-dispersion wavelength. Then, a negative GVD at 800 nm in combination with SPM gives rise to the formation of a soliton that enables extensive spectral broadening typically via soliton fission[9].

The subsequent frequency-doubling is carried out by a second harmonic crystal. Among many choices, periodic-poled lithium niobate (PPLN)[10] is often used due to its high efficiency at weak incident intensities and its inherent tuning capabilities by adjusting the temperature. Once the CEP of the oscillator is measured, additional disturbances may further add noise during amplification that needs to be determined, too.

Spectral Interferometry for Amplifiers

Earlier presented heterodyning methods have proven reliable in the field of high-repetition rate oscillators. However, with $1/f$ noise close to the DC baseband dominating at low frequencies, these methods have been not suitable for low-repetition rate amplifiers as the beat note would either be fully covered or only partially visible above the noise floor. Hence, a different approach is taken by spatially resolving the delayed interference of the fundamental and second harmonic that results in the formation of spectral fringes. This approach is referred to as spectral interferometry [95, 101, 102]. The fringes are formed for each interfering pulse and thereby enable single-shot resolution. The intensity pattern forming the

[9] Soliton fission is partly responsible for the spectral broadening in fibers in an anomalous dispersion regime. During propagation in fibers, the formation of higher-order soliton pulses and their break-up into fundamental solitons and accompanied non-solitonic radiation is described as the soliton fission process.

[10] A periodic-poled lithium niobate crystal is engineered to allow quasi-phase-matching conditions for a particular application such as, e.g., second-harmonic generation. This is achieved by inverting the Lithium niobate crystal orientation with a periodicy that depends on the wavelengths of the input and the generated light as well as the temperature.

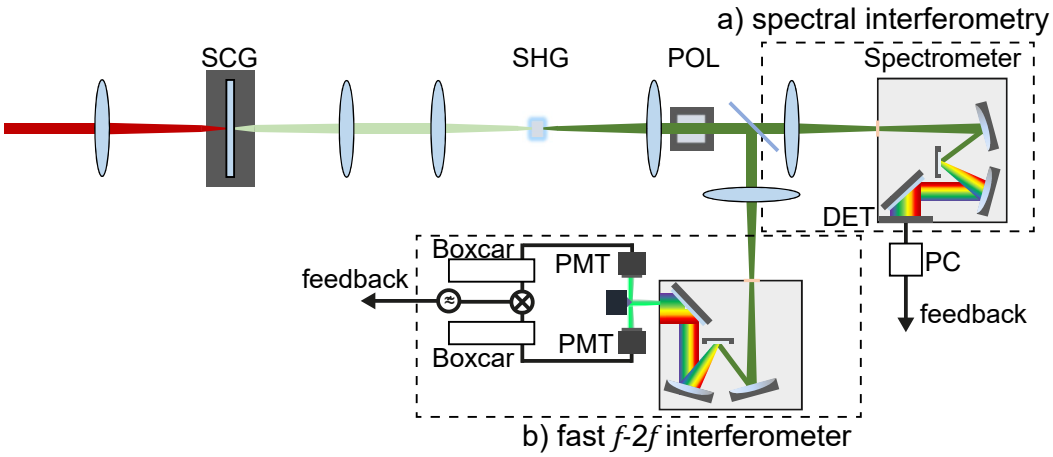

Figure 1.11: Common-path spectral interferometry setup involving a spectral broadening process (SCG) to reach at least one octave and a subsequent frequency-doubling (SHG) of the lower energy spectral wing. A polarizer (POL) is used to match the polarization of the SH and fundamental. Further detection is either carried out by traditional spectral interferometry involving a digital readout at the CCD (DET) a) or using the fast f-$2f$ interferometer b) with Photomultiplier tubes (PMT) and subsequent isolation of the signal by boxcar averagers (gated integrator).

fringes is described by

$$I(\omega) \propto \left|\mathcal{E}(\omega)+\mathcal{E}_{\mathrm{SH}}(\omega)\right| \tag{1.53}$$

$$= \left|A(\omega)\,\mathrm{e}^{i(\varphi_{\mathrm{CE}}+\Delta\varphi(\omega))}+A_{\mathrm{SH}}(\omega)\,\mathrm{e}^{i(2\varphi_{\mathrm{CE}}+\pi/2+\omega\tau_D+\Delta\varphi^{\mathrm{SH}}(\omega))}\right|^2 \tag{1.54}$$

$$= \left|A(\omega)\right|^2+\left|A_{\mathrm{SH}}(\omega)\right|^2+ \tag{1.55}$$

$$2\cdot\left|A(\omega)A_{\mathrm{SH}}(\omega)\right|\cdot\cos(\varphi_{\mathrm{CE}}+\Delta\varphi^{\mathrm{SH}}(\omega)-\Delta\varphi(\omega)+\pi/2+\omega\tau_D) \quad , \tag{1.56}$$

where the fringe characteristics are determined by the amplitude of both, fundamental $A(\omega)$ and second harmonic $A_{\mathrm{SH}}(\omega)$, as well as the last term in Eq. 1.56. While τ_D represents the non-zero temporal delay between the fundamental and the second harmonic that controls the width of the fringes of the resulting pattern, φ_{CE} is responsible for their position in the spectral domain. Additionally, potential phase fluctuations of the f and $2f$ components are included by $\Delta\varphi^{\mathrm{SH}}(\omega)-\Delta\varphi(\omega)$, while the constant indeterminable absolute phase is neglected in the description. The phase fluctuations are typically considered to have negligible effect. The temporal delay can be easily controlled in a Mach-Zehnder arrangement by the variation of arm lengths, while common-path arrangements enable adjustment of τ_D by introducing additional dispersive material after the spectral extension. A CEP drift at the back-end of the detection after frequency-doubling translates into a shift of the position of the fringes, which then can be subsequently detected on a CCD camera. The setup is shown in Fig. 1.11 a). As a result of the poorly efficient nonlinear processes weak spectral densities are present that lead to a reduced fringe contrast. Especially weak fringe contrast has established the need to average over multiple, successive laser pulses, which further deteriorates measurement precision.

To avoid these issues, Koke et al. [16] developed the fast f-$2f$ interferometer as shown in Fig. 1.11 b). It provides single-shot access to the CEP without any digital processing and hence avoids computational latencies. While the CEP is also resolved by means of nonlinear processes comparable to spectral interferometry, the read-out of the fringes is done by isolating one fringe, splitting it in half using a metallic prism, and subsequently, detecting each part separately by photomultiplier tubes. Then,

taking the difference of both measurements provides access to the movement of the CEP. An analog error signal enables stabilization and single-shot measurement of the CEP after isolation by boxcar integrators. While for f-2f interferometry the proper choice of the nonlinear processes has been addressed earlier, spectral interferometry as well as the fast f-2f interferometer typically rely on sapphire as a stable supercontinuum source and BBO for frequency-doubling. A more comprehensive discussion on potential sources is carried out in chapter 3.

Alternative Methods for Extracting the CEP from Amplified Pulses

In principle any carrier-envelope phase sensitive process could be employed for measuring the CEP. Especially, photoionization processes are of interest as they inherently show no unknown contribution to the absolute phase, which is typically the case for interferometer-based schemes. Such methods include the analysis of THz pulses originating from a few-cycle pulse-induced plasma [103], where a CEP-dependent spatial charge asymmetry is imprinted onto the THz pulses. Furthermore, CEP-dependent photoemission of electrons from metals [104, 105] is found to provide access to the CEP. Another common approach relies on above-threshold ionization (ATI) of inert gas atoms [106, 107], where a CEP-related asymmetry in the photoionization leads to an angular dependence in the measurement of the freed electrons. While ATI is routinely used for tagging, where the CEP of each pulse as measured by ATI is subsequently linked to the respectively measured experimental interaction [108], it is not employed to provide stabilization. This is due to the overall delay between measurement at the end of the laser chain and the feedback for stabilization, which results in a delayed feedback that is too slow for achieving appropriate correction bandwidths.

1.4.2 Stabilization

The measurement of the CEP was discussed under the assumption that the CEP slippage rate $\Delta\varphi_{\mathrm{CE}}$ is unperturbed. However, in reality, quantum noise, technical noise and other environmental disturbances, even if they are small, can have severe influence on the CEP. Over the earlier mentioned hundreds of optical cycles group-phase offset per cavity round-trip [11], even slight disturbances are having an accumulating effect. These noise sources are investigated in section 1.5.

With such a strong influence by noise, the active control of the CEP has been found to be a necessary step to minimize short-term and long-term CEP jitters. Especially in chirped-pulse amplification (CPA) schemes, the CEP is typically stabilized separately in two loops. While a fast loop is used to minimize high-frequency CEP noise of the oscillator, a second slow loop is employed to take control over additional low frequency CEP noise added during the amplification step.

CEP Stabilization of Oscillators

In oscillators, stabilization of the CEP slippage rate is carried out by either the feedback or the feed-forward approach, which are sketched in Fig. 1.12. Traditionally, the feedback approach is used for stabilization of the f_{CE} by means of establishing a phase-locked loop (PLL). To this end, the f_{CE} beat signal is measured by f-2f interferometry and subsequently, its phase is compared with a reference signal either by a mixer or a digital phase comparer. This reference signal is deduced from the repetition rate and down-converted by frequency division to an integer fraction of the repetition rate. After low-pass

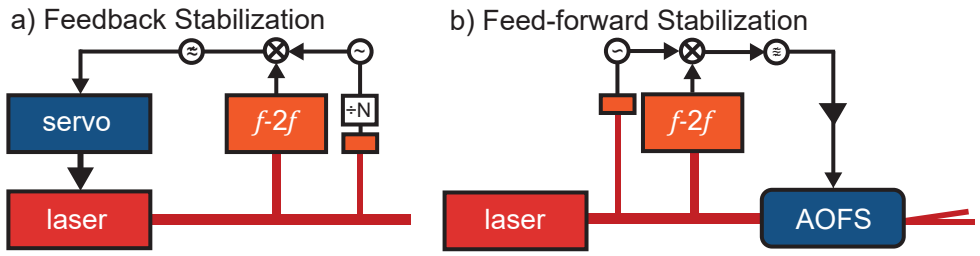

Figure 1.12: Oscillator stabilization schemes. a) feedback stabilization involving mixing of the measured beat note with a reference oscillator and subsequent low-pass filtering prior a servo is used for properly adjusting intra-cavity dispersion. The reference oscillator's frequency is deduced from the repetition frequency. b) Feed-forward approach, where an AOFS is used to correct for additional fluctuations of the carrier-envelope phase slippage.

filtering, the mixing product is further processed by a proportional-integral-differential (PID) controller to establish an appropriate error signal that enables improved loop stability. Several approaches have been realized to control the intra-cavity dispersion, which include shifting intra-cavity wedges [109] or introducing additional dispersion by tilting the end mirrors in a prism compressor section within the cavity [110]. Both lead to changes of the round-trip group-phase offset [111]. While these methods are fairly limited to correction bandwidths up to several ten kHz [112] due to associated inertia while moving, modulation of the pump power [6] has been found to increase the possible feedback bandwidth and hence possible control. In this way, the feedback can be given in principle up to the relaxation oscillations [113]. Modulation of the pump power is realized by using the error signal provided by the measurement to control an acoustic wave inside an acousto-optic modulator (AOM) situated in between the gain medium and the pump laser. These modulations lead to changes of the intra-cavity peak power and hence modulate, e.g., the Kerr-induced nonlinear refractive index. This affects the phase and group velocity differently and therefore leads to a change of the group-phase offset [114]. While the Kerr nonlinearity acts nearly instantaneously, the laser response to gain changes are a limiting factor. Furthermore, a time delay between measurement and inserted feedback, such as the propagation of the acoustic wave inside the AOM or the servo control, ultimately limit the correction bandwidth to around 100 kHz [115]. Therefore, any noise above this bandwidth cannot be corrected. Furthermore, the modulation of intra-cavity pump power also leads to a modulation of the output power. To date, the best reported oscillator stabilization based on the feedback method resulted in sub-100 mrad residual jitters [12].

In 2010, Koke et al. [116] presented a scheme that allows to circumvent drawbacks associated with the feedback approach by utilizing an acoustic-optical frequency shifter[11] (AOFS) to correct the CEP of the pulse directly without any intra-cavity disturbances. Termed feed-forward, this scheme as depicted in Fig. 1.12 b) enables to increase possible correction bandwidth up to 1 MHz [117], which allows to generate CEP stable pulses with residual jitters below 45 mrad [116]. By diffracting the beam within the AOFS on an acoustic wave-induced refractive index modulation, the minus first-order diffraction provides a frequency comb that reads

$$\nu_m(t) = f_{\mathrm{CE}}(t) - f_{\mathrm{ac}}(t) + m f_{\mathrm{rep}}, \tag{1.57}$$

where $f_{\mathrm{ac}}(t) = {}^{v_{\mathrm{ac}}}/_{\lambda_{\mathrm{ac}}} = f_{\mathrm{CE}} + n f_{\mathrm{rep}}$ is the frequency of the acoustic wave. Thereby, the carrier-envelope

[11] Similar to an AOM, an AOFS employs the interaction of an acoustic wave-induced refractive index lattice with the pulse to shift frequencies. Within CEP stabilization schemes, it is optimized for removing the carrier-envelope offset frequency from the frequency comb, which renders the output, typically in first diffraction order, carrier-envelope offset free.

offset is effectively removed from the comb. This approach has several advantages compared to feedback stabilization. First, since no PLL is involved, it is robust against phase shifts that exceed π and automatically re-locks. Second, unperturbed operation of the laser ensures stable performance and avoids influence on any laser parameters such as repetition rate or pulse power. Nevertheless, side-effects exist that need to be addressed when the feed-forward approach is used as a seed for CPA-based amplification with stretchers and compressors. The interested reader is referred to [116, 117, 118, 119] for more details on the feed-forward technique.

To date, the best performance on any oscillator CEP stabilization scheme is obtained by Borchers et al. [12], who combined the feedback with the feed-forward approach and achieved a residual timing jitter of below 10 as, which corresponds to 20 mrad residual phase jitter.

CEP Stabilization of Amplifiers

Once the oscillators' CEP is stabilized by either a feedback or feed-forward arrangement and the pulse is amplified in, e.g., a CPA scheme, the pulse experiences additional spurious distortions originating from stretching and compressing of the pulse, pulse picking or as a result of the amplification process itself. However, as these fluctuations typically appear on time scales much slower than CEP noise that originates in the oscillator cavity, they can be (partly) compensated by an additional slow loop. Using earlier presented spectral interferometry or the fast f-$2f$ interferometer and extracting the fringes' change in position, the feed back signal can be used to either adjust the intra-cavity dispersion within the oscillator or by adapting the dispersion within the amplifier system. While the former may result in interference of both error signals, rendering a CEP lock in some cases troublesome, the latter is often used to control the CEP up to frequencies of several hundreds of Hz. Dispersion control within the amplifier can be carried out by adjustment of the compressor or stretcher [120, 121] as well as by the use of a programmable acousto-optic dispersive filter (AOPDF) [122]. The latter is typically included in CPA-based systems anyhow, which then enables high-bandwidth feedback. Performance of the amplifier CEP stabilization is typically limited to around 100-200 mrad on a shot-to-shot basis [5, 16, 19, 123], while most systems require averaging over multiple shots to achieve stabilization, which can lead to strongly underestimated residual CEP jitters. Additionally, stabilization can be limited by slow processing times of the spectrometer in the detection or due to the digital extraction of the fringe position that leads to a reduced feedback bandwidth of the CEP control.

1.5 Carrier-Envelope Phase Noise

The CEP not only needs to be stabilized against a partial change of 2π from pulse-to-pulse, but also due to the interference of various noise sources and coupling mechanisms that prevent the constant round-trip evolution of the group-phase offset inside the cavity and further on while propagating through, e.g., possible amplification stages. Additional noise is then added during the measurement of the CEP. Limiting noise sources are typically of quantum noise origin, and hence stochastic, while technical noise sources can substantially increase the noise floor, which nevertheless have rather a deterministic character. Further on, all parts within a CEP-stabilized laser chain as shown in Fig. 1.13 are addressed separately. The emphasis is laid on the influence of noise especially on the CEP. Beginning with the impact of the pump and coupling mechanisms within the cavity on the basis of the Haus Master equation, further

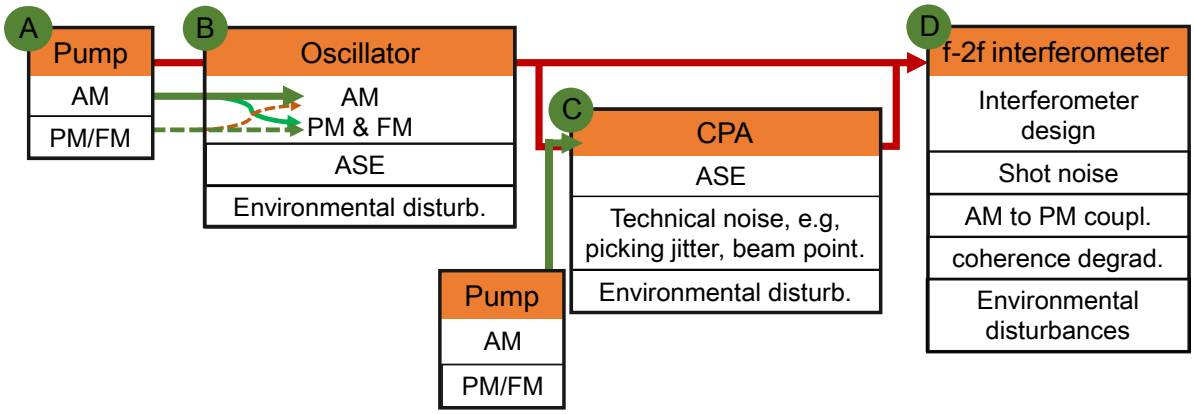

Figure 1.13: Sources of noise in the laser chain, starting from A), the pump, B) noise coupling inside the oscillator, C), pump and possible CPA-induced noise and d), noise during detection of the CEP.

disturbances during amplification and subsequent measurement of the CEP are addressed.

1.5.1 Coupling Effects and Noise during Formation of the Laser Pulse

During formation of the laser pulse within the cavity, the pump feeding the gain medium with energy induces amplitude modulation (AM) and phase modulation (PM) of the intra-cavity field. These fluctuations can be either of technical or quantum origin and are further accompanied by environmental perturbations and other noise sources within the laser cavity itself. Additional frequency modulation of the pump (FM) can lead to changes in the intra-cavity field due to frequency-dependent absorption of the pump. Common pump lasers possess a fractional frequency stability within 10^{-9} and relative intensity noise in the order of 10^{-7}, which results in a dominant AM contribution to the fluctuations of the intra-cavity field. The former, frequency fluctuations of the pump, are further omitted in the discussion.

The combined effect of amplitude modulation, phase modulation and other disturbances within passively mode-locked lasers, where a fast saturable absorber is employed, has been for the first time comprehensively studied by Haus and Mecozzi [86, 87], who made use of the Haus Master equation [86] as presented in Eq. 1.42. While the Master equation describes the steady-state situation, weak disturbances are included by making use of the perturbation theory in an adiabatic way. Employing the ansatz

$$A(t,T_l) = \left(A_0 \operatorname{sech}\left[\frac{t}{\tau}\right] + \Delta A(t-t_0,T_l)\right) \times \exp\left(-i\frac{\delta}{2}A_0^2\frac{T_l}{T_R}\right) \tag{1.58}$$

to solve the Master equation and further expanding ΔA in first-order, the perturbation of ΔA can be expressed as variations of four pulse parameters. These include pulse energy ΔE_P, the phase $\Delta\varphi$, timing Δt and the center frequency $\Delta\omega_c$ of the pulse. After additional calculations that are out of the scope of this work [87], equations of motion for the above parameters are formulated. These equations of motion include noise sources $S(t,T_l)$ that range from gain fluctuations Δg, length changes Δl and refractive index fluctuations Δn to amplified spontaneous emission[12] fluctuations.

[12] Amplified spontaneous emission describes the amplification of the photons spontaneously released by a decay process, the latter being connected to the limited life time of an excited state. Thus, the energy of this transition to a lower, stable energy state is associated with the release of a photon. In the presence of a population inversion, the freed photon can induce stimulated emission, which then leads to incoherent photons within the laser pules that affect the pulse in manifold ways.

From these equations of motion the following conclusions can be drawn in the presence of noise within the cavity [87]. Energy fluctuations in the form of amplified spontaneous emission (ASE) either from the pump or the gain medium couple to phase changes via Kerr-induced SPM. Additionally, energy variations ΔE_p lead to group velocity changes and hence additional timing jitter. Furthermore, center frequency variations $\Delta\omega_c$ are experiencing a restoring force by the limited gain bandwidth of the medium as the spectrum is pushed back to the gain center. This induces a timing jitter via group delay dispersion. Additionally, cavity length changes Δl lead to a timing jitter as well as a repetition rate variation. Cavity length fluctuations might further introduce beam pointing fluctuations that can change the effective saturable absorber action of the Kerr lens. Refractive index fluctuations are only considered here in first-order and introduce similar noise as cavity length changes.

While the model introduced by Haus and Mecozzi is based on soliton-like pulse dynamics with weak perturbations, it neglects other possible degrees of freedom [124]. These include pulse shape changes or possible intra-cavity chirp. Further, it totally omits laser and relaxation dynamics. Nevertheless, these effects have been found important to describe the composition of the carrier-envelope phase noise. For example, self-steepening was seen to be of utter importance for the slippage of the CEP, where it is found to introduce additional group delay [125] and hence add another nonlinear contribution that is opposite in direction and twice as strong compared to the nonlinear phase shift induced directly by SPM [126]. Furthermore, the relaxation dynamics are of critical importance, too, as the gain medium inherently limits the transfer of any fluctuations to above the upper-state lifetime. In the case of Ti:sapphire oscillators, where the gain medium has an upper-state lifetime of around 4 µs, the actual transferable frequency contribution from any fluctuation is limited to below roughly 300 kHz, which is the relaxation oscillation frequency. Above this, only white, random noise originating mainly from amplified spontaneous emission and vacuum noise entering through elements with optical loss is present. This effect is also referred to as the low-pass filtering of the gain medium. However, in lasers with very long upper-state lifetime such as Er:doped fiber lasers, where $\tau_{\mathrm{rad}} = 8 - 10$ ms, the laser dynamics become increasingly important and the actual laser response bandwidth depends on the nonlinear losses introduced to saturate self-amplitude modulation [127]. The laser response bandwidth is typically higher compared to the response bandwidth due to the upper-state lifetime of the gain medium alone.

Effect on the Frequency Comb and the CEP

Intra-cavity pulse propagation is severely influenced by quantum noise as was shown by Haus and Mecozzi [87], which also plays a strong role in the noise dynamics regarding the carrier-envelope phase and the whole laser comb. Fundamentally, the width of each frequency comb needle is limited by the ASE-induced phase noise contribution, which is also known as Schawlow-Townes (ST) noise [128]. Further corrected by Lax et al. [129], the ASE-induced minimum linewidth reads

$$\Delta\nu_{\mathrm{laser}} = \frac{\pi h\nu(\Delta\nu_c)^2}{P_{\mathrm{out}}}, \tag{1.59}$$

where $\Delta\nu_c$ is the full width at half maximum (FWHM) resonator bandwidth. Parasitic losses are omitted. In mode-locked lasers, P_{out} is typically taken as the full output of all laser modes, since all cavity modes are phase-locked. Therefore, Schawlow-Townes noise refers to a translational jitter of the whole comb, resulting in a finite linewidth. For passively mode-locked lasers without stabilization of the repetition

rate Paschotta suggested [130] that the Schawlow-Townes limit is only valid in the center of the comb spectrum. This is a result of the ASE-induced timing jitter, which results in a broadening of the needles that are further away from the center of the pulse. This effect is referred to as the elastic-tape model and leads to a breathing of the comb [131]. Due to the measurement by f-$2f$ interferometry relying on heterodyning either spectral edge, this results in a strongly increased linewidth of the CEP beat note. In chapter 2 measurements are presented where the carrier-envelope frequency beat note at 6 dB (representing the optical FWHM) is roughly 50 kHz in width, which, in combination with the upper-state lifetime, comes close to a Lorentzian lineshape limit. The central linewidth, however, can be estimated for a repetition rate of 85 MHz at 800 nm and 500 mW output power to be below mHz.

While frequency comb considerations are interrelated with the CEP via Eq. 1.50, carrier-envelope phase noise is more suitably characterized using frequency noise densities after subtraction of the periodic evolution of the phase. ASE fluctuations of the pulse energy ΔE_p, timing jitter Δt as well as the optical phase $\Delta\varphi$ each lead to their own white noise spectra that are mutually uncorrelated. Fundamentally, earlier introduced Schawlow-Townes noise not only gives the minimum linewidth of the comb needles, but also provides the lowest seen frequency noise floor. The respective ASE limit $S_{\nu_c,\mathrm{ST}}$ is estimated to be [132]

$$S_{\nu_c,\mathrm{ST}} = 0.11\Gamma \quad \text{with} \tag{1.60}$$

$$\Gamma = \sqrt{\Theta \frac{h\nu_c g}{P_{\mathrm{int}}}} f_{\mathrm{rep}}, \tag{1.61}$$

where Θ is the excess spontaneous emission, g the saturated intensity gain and P_{int} the intra-cavity power. When considering power fluctuations inflicted by ASE, the resulting frequency noise density (FND) $S_{\Delta P}$ reads

$$S_{\mathrm{PSD},\Delta P} = \sqrt{2\Theta g P_{\mathrm{int}} h\nu_c} \tag{1.62}$$

$$S_{\Delta P} \approx \kappa f_{\mathrm{rep}} \tau_p S_{\mathrm{PSD},\Delta P}, \tag{1.63}$$

with τ_p the pulse duration, κ the power-to-CEP coupling factor that enables conversion from the power spectral density (PSD) to the FND. While depending on the cavity parameters, the CEP noise of typical ultra-short Ti:sapphire lasers is not dominated by a white noise floor originating from power fluctuations as other sources are stronger. Another contribution to the white noise floor seen in most frequency noise densities is the timing jitter that is due to the unbound drift of the pulse timing as well as center frequency fluctuations. Noise originating from repetition rate changes can be described by [132]

$$S_{f_{\mathrm{rep}}} = 0.73\Gamma f_{\mathrm{rep}} \tau_p \tag{1.64}$$

$$S_\nu = 0.73|\nu - \nu_c|\Gamma\tau_p, \tag{1.65}$$

where the latter includes the contribution as a result of measuring the CEP beat note far off from the center frequency ν_c. The timing jitter noise level is typically above the Schawlow-Townes level and is reached within some part of the frequency spectrum.

To summarize, first, the optical phase noise is mainly limited by Schawlow-Townes noise as it defines the linewidth. Additional contributions are due to the unbound drift of the pulse timing, leading

to an extended linewidth further away from the central frequency of the comb. Together, optical phase noise then translates to carrier-envelope phase noise by projecting the comb towards zero frequency to its offset [130]. Second, as the CEP jitter is also referable as the fluctuation of the group-phase offset per round trip, changes in the refractive index Δn within the gain medium or during propagation in air influence the CEP via pump power-induced crystal heating [133] and external perturbations such as pressure changes. Third, earlier addressed fluctuations of the group delay dispersion in combination with a central frequency shift $\Delta\omega_c$ of the pulse lead to GPO fluctuations and hence a timing jitter. Fourth, additional nonlinear phase shifts originating from the amplitude modulation that change SPM and self-steepening conditions lead to fluctuations of the CEP [126, 133, 134]. Investigations into the relative contributions of these different sources to the CEP jitter has shown that the nonlinear phase shift dominates over other sources within a few-cycle oscillator [126, 134], in which the intra-cavity GDD is within 10-100 fs^2. This is the case for the employed Ti:sapphire laser in this work. After the pulse is severely influenced by intra-cavity noise sources, further propagation and amplification may deteriorate the CEP jitter even further. This is addressed in the upcoming part.

1.5.2 Additional Noise induced during Amplification

During amplification of the oscillator pulse in a typical chirped-pulse amplification scheme, the pulse is first stretched by using dispersive media or optics to avoid damage when subsequently being amplified and typically down-clocked to a lower repetition rate. Afterwards, the pulse is compressed as close as possible to its Fourier-transform limit to achieve the highest possible peak powers. During this whole process, besides white quantum noise originating from ASE, especially environmental and technical influences on the CEP are present. In the latter, these involve pulse picking jitter [135], beam pointing while being stretched or compressed [32, 133] or even periodic opening of a valve within the cooling circuit. Environmental disturbances such as pressure or temperature fluctuations can readily introduce strong phase noise, too, as they change the effective optical path length. Furthermore, amplifier pump laser fluctuations from shot-to-shot have been found to be a limiting factor [118], which have been also very important for the stability of the oscillator. Nevertheless, the strongest contribution to the CEP jitter is typically still from the oscillator and hence, residual CEP noise in CPA-based amplifiers is ultimately limited by the performance of the oscillator [118].

1.5.3 Noise Sources during CEP Detection of Oscillator Pulses

So far, limitations on the CEP stability that are inherently present during pulse formation and subsequent amplification have been discussed. In this section, additional noise that is appended during measurement is considered that forces the phase loop to respond and hence may deteriorate CEP stabilization performance. Besides technical noise sources, the emphasis is laid on the inherent presence of shot noise that affects the precise extraction of the CEP in such schemes.

Noise in f-2f Interferometry

Measurement of the CEP by employing some variant of f-2f interferometry as is shown in Fig. 1.9 a) can be separated into a combination of several processes that include spectral broadening, interferometry, second-harmonic generation and photodetection. Each of these steps bear their own noise characteristics

and origins, which are addressed briefly in the following for f-$2f$ interferometry. The first step, spectral broadening, is typically carried out within a PCF. Amplitude noise of the seed is amplified and directly transferred into phase noise via amplitude-to-phase coupling as the GPO is intensity-dependent [5, 112, 136]. According to numerical investigations conducted by Washburn et. al. [136] and Borchers et al. [12], relatively short fibers of about 1 cm length, slightly positively chirped seed pulses and higher pulse energies are enabling low phase noise conditions while an octave-spanning spectrum is still achieved. The supercontinuum process can also lead to degradation of the coherence as has been observed within fibers, where a loss of temporal coherence renders the pulses hardly compressible [137, 138].

Second, the interferometer design can significantly influence the precise measurement of the CEP. The simplest concept of f-$2f$ interferometry is realized in the form of a Mach-Zehnder interferometer. As has been shown in section 1.4.1, a Mach-Zehnder interferometer separates the high frequency wing of a supercontinuum from the low frequency region, which is subsequently frequency-doubled. Overall, this type of interferometer is extremely susceptible to noise as the two arms are able to accumulate noise individually. Possible noise sources are of acoustic nature, mechanical vibrations, pressure changes, and thermal drift. Minimization of unshared beam path allows a reduction of these to a good extent. While one option for reducing the unshared beam path is to introduce a relative delay of the orthogonally polarized f and $2f$ components by implementing a birefringent crystal after the second harmonic step [139], it is more straightforward to employ instead a quasi-common path setup as has been carried out in this thesis. This interferometer design reduces the unshared beam path to the smallest possible extent that still allows to compensate the group delay [12, 118]. To this end, a dichroic beam splitter is used to reflect the short wavelengths and transmit the long wavelengths. The latter region is subsequently reflected upon incident on a metallic mirror after about 1 mm of propagation through air. Especially, the $1/f$ contribution at low frequencies (0.1 Hz -10 Hz) is subsequently strongly reduced [118, 140]. Only true common-path interferometers are able to exceed this phase noise performance by simultaneous spectral broadening and difference-frequency generation (DFG) in one crystal. This is readily carried out in periodic-poled lithium niobate (PPLN), which exhibits a high conversion efficiency and strong reliability [141]. Unfortunately, this truly common-path interferometer requires a spectral width straight from the oscillator of more than 300 nm to extend the spectrum sufficiently in the PPLN. This broad initial spectral bandwidth has been found hard to be reached for most Ti:sapphire laser, including the one employed in this work.

Third, second harmonic generation is necessary, where the phase adds a constant $\pi/2$ offset and doubles itself. However, additional noise seems not to pose a problem during this step [20].

Finally, noise may be further inflicted during the detection by a photodiode, too. Here, the fundamentally limiting noise floor is given by the fast avalanche photodiode under very low light conditions, also called the noise-equivalent power (NEP). The NEP is a composition of several white noise sources, such as leakage currents[13], avalanche-induced noise[14] and thermal Johnson-Nyquist noise[15] within the

[13]Photodiodes consist of a p-n junction that has a dark or leakage current. Even without incident light, electrons or holes tunnel through potential barriers.

[14]When weak incident photon numbers are present, amplification is typically necessary. Avalanche photodiodes make use of avalanche amplification, where one photo-electron created by the incident photon is accelerated within a field and subsequently, electrons are additionally freed by means of impact ionization. Both electrons are further accelerated and generate multiple additional electrons, which effectively increases the strength of the original signal.

[15]Johnson-Nyquist noise describes the electronic noise caused by thermally-induced excitation of electrons in a resistive element, which is typically stochastic and hence white noise.

electronics. Once illumination exceeds the NEP, optical shot noise is prevalent within the white noise floor, which reduces the achievable signal-to-noise ratio (SNR) of included signals strongly. Although average powers directly out of oscillators can readily exceed 100 mW translating into the order of 10^{10} photons per pulse, it seems surprising that shot noise could pose a problem. Nevertheless, extending the spectral width above one octave with common techniques such as the earlier addressed PCFs reduces the amount of available photons already by at least three orders of magnitude at the continuum's edges. Especially in the case of PCFs at low input energies, soliton fission combined with intra-pulse Raman scattering leads to energy loss that then results in the spectrum being pushed further into the IR. This renders the process of spectral extension weakly efficient. In the best case scenario, about 10^7 photons are left in the narrow spectral range used for second harmonic generation. Making use of highly-efficient quasi-phase matched crystals such as PPLN for frequency-doubling, conversion efficiency is still found by a marginal 1 %, leaving 10^4 to 10^5 photons for interference. This results in a SNR of only a minor 100. The effect of these low photon numbers on the performance of the CEP detection in oscillators is discussed numerically in the upcoming section.

In the case of low photon numbers, optical shot noise, as an inherent consequence of the photon nature of light fields, may lead to additional noise appended during measurement. Statistically, in the context of classical light, shot noise is a result of the completely uncorrelated detection of each photon, which reveals its underlying pure Poissonian statistics. In general, the detection events are randomly distributed according to the Poissonian probability mass function given by

$$p(k) = \frac{\lambda^k e^{-\lambda}}{k!}, \lambda > 0, k \in \mathbb{N}, \tag{1.66}$$

where λ is the expected value and variance. Hence, if on average $\langle N \rangle$ photons are detected, the uncertainty or standard deviation is given by $\sqrt{\langle N \rangle}$. This clearly shows the importance of high photon numbers to be present during detection to avoid the impact of shot noise on the measurement performance. As this effect is present in all optical measurements, it is referred to as the quantum limit or shot noise limit and is of stochastic nature. In the upcoming part, the effect of shot noise on the CEP detection is simulated.

Numerical Investigation of Shot Noise in Oscillator CEP Detection

Following Borchers et al. [24], the effect of shot noise is numerically simulated by interfering a train of pulses with an average photon number $\langle N \rangle$ per pulse at the detection front-end of the f-$2f$ interferometer. The beat signal $N(k)$ with k elements is sampled at the lasers repetition rate and includes a modulation of both components, f and $2f$, to account for the amplitude modulation measured by the heterodyne method. It reads

$$N(k) = \left| \sqrt{\langle N_f \rangle} + \sqrt{\langle N_{2f} \rangle} e^{i\varphi(k)} \right|^2, \tag{1.67}$$

where $\langle N_f \rangle$ and $\langle N_{2f} \rangle$ are the average photon numbers in the respective spectral regions and $\varphi(k) = 2\pi k f_{\mathrm{CE}} / f_{\mathrm{rep}}$. By adding Poissonian noise with a spread of $\sqrt{N(k)}$ to the beat signal, shot noise is introduced.

The simulation parameters are comparable to typical Ti:sapphire-based oscillators. The repetition rate and the carrier-envelope offset frequency f_{CE} are set to 80 MHz and about 2 MHz, respectively. The

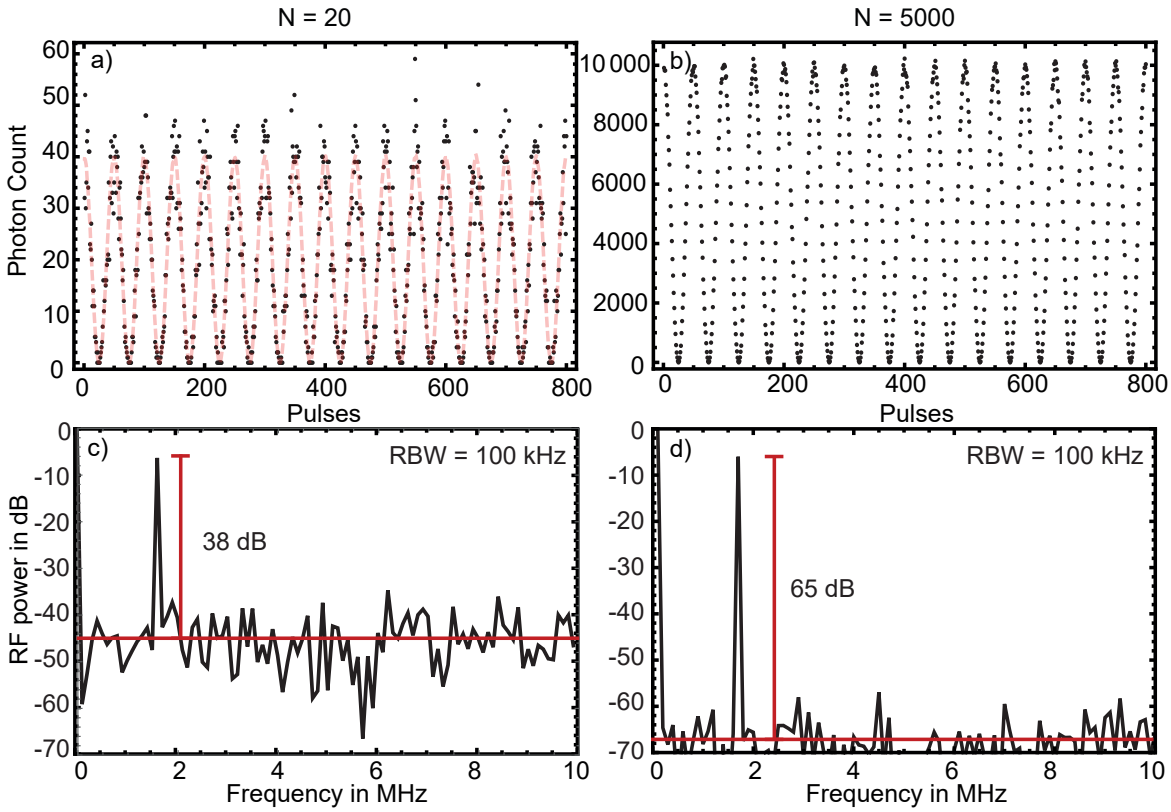

Figure 1.14: Following Borchers et al. [24], the simulated heterodyning of the fundamental and the second harmonic at $f_{\mathrm{rep}} = 80\,\mathrm{MHz}$ with a CEO frequency of $f_{\mathrm{CE}} = 2$ MHz for an average photon number on the photodiode of $\langle N \rangle = 20$ is shown in a), and $\langle N \rangle = 5000$ in b). c) and d) show the corresponding RF power spectra until 10 MHz.

Figure 1.15: Simulated CEP jitter as a result of shot noise with respective incident photon numbers and signal-to-noise ratio of the beat signal at the full bandwidth of 80 MHz. The best reported beat note strength of 60 dB are marked, which indicates a residual shot noise-induced CEP jitter of 20 mrad.

simulation comprises 800 subsequent pulses, as can be seen in Figure 1.14 a) and b). Here, only the balanced case is present, where the amplitude modulation has 100 % modulation depth and is formed by an equal number of photons in both interfering parts $\langle N_f \rangle = \langle N_{2f} \rangle = 10$. Hence, a total of $\langle N \rangle = 20$ photons are present. This corresponds to a beat note peak at -6 dB relative to the intermode beat in a 100 kHz resolution bandwidth (RBW), which is used throughout this thesis if not otherwise stated. As the red dashed line is a guide to the eye, it is clearly visible that shot noise is strongly present, although this already translates to a signal-to-noise ratio (SNR) of the beat note of 38 dB. In b) and d), the average photon number is 5000, which results in a clear oscillation with a beat note strength above 65 dB. The SNR for a perfect detector without spurious noise can be given by

$$\mathrm{SNR} = \frac{2\langle N_f \rangle \langle N_{2f} \rangle}{\langle N_f \rangle + \langle N_{2f} \rangle} \cdot 800\,, \tag{1.68}$$

with $\langle N_f \rangle \langle N_{2f} \rangle$ the mean square of the beat signal and $\langle N_f \rangle + \langle N_{2f} \rangle$ the variance of the Poissonian noise. While the former can be explained to be proportional to the signal strength, the noise scales with the latter. To account for the resolution bandwidth[16] of 100 kHz and the integration over 800 shots, the additional factor is required. Clearly, low photon numbers can have an effect on the beat note strength as seen in 1.14, but how does this translate into shot noise-induced CEP jitter? First, the phase of the Poissonian noise-induced pulse train is extracted using the Takeda algorithm[17] [142] and then directly compared to a perfect pulse train that is free of any noise influence. Figure 1.15 shows the effect of shot noise on the residual CE jitter. In a double-logarithmic plot a slope of -1/2 is found, representing a tenfold decrease of the shot noise floor translating into a 20 dB increase in beat note SNR, in agreement with the dependence on $1/\sqrt{\langle N \rangle}$ found for Poissonian noise. Best reported signal-to-noise ratios of 60 dB imply a residual shot noise-induced CEP jitter of around 20 mrad. For simplicity, additional noise

[16] The resolution bandwidth determines the smallest resolvable frequency during the measurement. Therefore, it defines the resolution and is crucial for estimating the signal-to-noise ratio. The longer the acquisition time, the more features of a signal can be resolved.

[17] The Takeda algorithm enables the Fourier-transform-based extraction of a fringe pattern. Here, it is used to extract the phase noise density by means of isolating the carrier-envelope phase noise from the continuous evolution of the CEP.

sources during detection that would reduce the achievable phase jitter such as the NEP are neglected. Furthermore, asymmetric photon numbers in fundamental and second harmonic, respectively, that would lead to a reduction in performance are neglected here, too [24, 119]. Overall, although photon numbers are relatively low in f-$2f$ interferometry, strong and tight feedback can be achieved even at beat strengths above 35 dB generated by the interference of only about 10 photons per shot. A similar analysis for the generation of a fringe pattern and subsequent CEP detection of amplified pulses based on spectral interferometry is presented in section 3.1.1.

Chapter 2

Linear and Nonlinear Analysis of Carrier-Envelope Phase Noise

Further progress in fields such as precision frequency metrology and attosecond pulse generation requires precise control of the carrier-envelope phase and frequency. While especially Ti:sapphire-based laser systems have been found to allow well-performing CEP stabilization schemes that enable control over the CEP of below 10 as timing jitter, other laser sources have shown extensive carrier-envelope phase noise and hence are not readily stabilized. In order to improve the understanding of parameters that affect the carrier-envelope phase inside a laser cavity, this chapter extends common tools that are employed for analytic noise investigation, such as the power spectral density or amplitude spectral density, with two novel approaches. The first involves a correlation analysis of amplitude and frequency noise by using a time-resolved Kendall correlation methodology, which, in principle, can be employed for any other two correlating variables. The second approach extracts the inherent statistical properties within the measured time series. Thereby, it allows to identify and differentiate deterministic and stochastic noise on different time scales. In the case of carrier-envelope phase noise, the former, deterministic noise, is in most cases not a fundamental limit and can be circumvented, while stochastic noise either originates from a fundamentally limiting process, e.g., amplified spontaneous emission or shot noise.

This chapter begins by introducing bivariate correlation analysis with a particular focus on Kendall's τ correlation coefficient. Subsequently, a methodology for a time-resolved Kendall correlation assessment is presented and is applied to a sinusoid covered in a stochastic time series to assess the validity of this approach. Then, principles of nonlinear time series are presented, and illustrated with the famous Lorenz attractor. Subsequently, the correlation histogram and the surrogate method are introduced. Based on these concepts a novel methodology is developed in this work that facilitates the analysis of the statistical properties as a function of time and is thus applied to a purely stochastic and strongly deterministic time series. After presenting four different laser sources and their CEP measurements, a comparative study on their noise characteristics is carried out, where the above introduced methods are employed to gain insight in why some lasers are readily CEP stabilized and others show tremendous fluctuations inhibiting proper stabilization. Finally, a possible origin of a found broadband coupling mechanism between amplitude and frequency noise in one of the lasers is attributed to its mode-locking method.

2.1 Bivariate Correlation Analysis

Correlation analysis is particularly useful for examining the dependence of two or more variables. A related concept in optics is coherence, which basically describes the correlation of electric fields and phases in time and space. Here, the dependence of multiple variables in general is assessed. For simplicity, only bivariate analysis is considered. To this end, linear relationships between two variables or data sets are quantified by means of a measure that is typically bounded to be ranging from [-1,+1]. While both extremes indicate perfect correlation (+1) and anti-correlation (-1), respectively, zero refers to no relationship present. With growing deviation from zero, the degree of (anti-)correlation is quantified. The simplest correlation coefficient is the Pearson's product-moment coefficient r [143], which is described in an empirical approach between two data sets X and Y by

$$r = \frac{\sum_{i=1}^{N}(x_i-\bar{x})(y_i-\bar{y})}{\sqrt{\sum_{i=1}^{N}(x_i-\bar{x})^2 \cdot \sum_{i=1}^{N}(y_i-\bar{y})^2}}, \tag{2.1}$$

where N is the total number of elements in each data set. $\bar{x} = {}^1\!/_N \sum_{i=1}^{N} x_i$ and $\bar{y} = {}^1\!/_N \sum_{i=1}^{N} y_i$ represent the respective means. While Pearson's correlation coefficient is only applicable to linear relationships, it needs to be interpreted with caution regarding possible nonlinear dependencies. Pearson's correlation coefficient is indeed zero when no correlation exists between the data sets. However, this does not imply that there is no correlation when it is equal to zero. Furthermore, Pearson's coefficient is a parametric measure[1] and therefore assumes normally distributed variables, while, in reality, the actual distribution of the data sets is typically unknown. In combination with a weak robustness (increased impact of outliers), the usability of Pearson's correlation coefficient in many cases is limited.

Therefore, deviating to non-parametric rank-based correlation coefficients such as Spearman's ρ or Kendall's τ is straightforward in the presented analysis. Rank-based correlation coefficients do not rely on interval-scaled data but on their ranks. Ranks are assigned by allocating to each value its position within the whole value range of the data set. Then, the ranks are used instead of the values to classify the strength of the correlation, which is termed ordinal association. These coefficients assume no probability distribution of the original data sets. A rather robust non-parametric correlation estimate that has been used widely in physical science is obtained by employing Kendall's τ [144], which is able to detect also higher-order correlations. Kendall's τ is computed by allocating to each element of the data set a rank for its position within the whole value range. This is carried out separately for both data sets, leading to a set of value position, i.e, $X = [x_1, \cdots, x_N]$ and $Y = [y_1, \cdots, y_N]$. Then, comparing the order of consecutive elements within one data set relative to the other enables to measure the monotonic association between both. A pair is called concordant, if the relative ordering of elements within X increases (decreases) with the one of two elements within Y, i.e., $x_i > (<) x_j \wedge y_i > (<) y_j$. A disconcordant pair is referred to if the ranking inside each data set is opposite, i.e., $x_i > (<) x_j \wedge y_i < (>) y_j$ holds. In this regard, the two data sets are compared, and the concordant pairs N_c and disconcordant pairs N_d are counted. With N elements in either data set, ${}^1\!/_2 N(N-1)$ pairs of data points exist. Possible ties, where $x_i = x_j$ or $y_i = y_j$, are summed up in t_x and t_y, respectively. From there, the Kendall-τ coefficient can be calculated. While

[1] A parametric measure, as opposed to a non-parametric measure, assumes an underlying probability distribution within the analyzed time series.

different definitions exist the simplest approach excludes ties and is termed Kendall-τ_a

$$\tau_a = \frac{N_c - N_d}{N(N-1)/2}\,. \tag{2.2}$$

Nevertheless, it can occur that the same values in a data set exist and hence, the same position within the value range is assigned multiple times. Therefore, ties need to be taken into consideration, which leads to the definition of the Kendall-τ_b

$$\tau_b = \frac{(N_c - N_d)}{\sqrt{(N_c + N_d + t_x)(N_c + N_d + t_y)}}\,. \tag{2.3}$$

In this way, the correlation between two data sets is given by a value of Kendall's τ that ranges from -1 for complete anti-correlation to +1, when complete correlation is present. If Kendall's τ is close to 0, no correlation is present. Within this thesis, the Kendall-τ_b definition is used as it includes ties. This is typically necessary when real measurement sets are analyzed since discretization by digitalization and a limited measurement range lead to values being measured manifold.

2.1.1 Time-Resolving Kendall-τ Correlation

In most measurements not only the interval-scaled information is obtained (e.g. temperature, pulse power, pulse duration), but also the difference in time between these single measurements, termed sampling time, is available. While Kendall's τ_b correlation coefficient is in general indifferent to any interval scaling due to its rank-based assessment, the sampling time can be taken into consideration by a deliberate choice of single measurements that build the data sets to be assessed. To this end, the two different data sets or time series $x(t) = [x(t_0), x(t_1), \ldots, x(t_N)]$ and $y(t) = [y(t_0), y(t_1), \ldots, y(t_N)]$ are individually resampled. The resulting data series or vectors $\vec{X} = [X_1, \ldots, X_j]$ and $\vec{Y} = [Y_1, \ldots, Y_j]$ are each comprised of j elements, while each element within is created by the average over M single measurements under the condition of $j \cdot M \leq N$. This yields

$$\vec{X}_j = \frac{1}{M} \sum_{i=(j-1)M+1}^{jM} x(t_i)\,, \tag{2.4}$$

where i is indexing each element in the original time series, j the index of the averaged element, M is the length of the segments over which it is averaged and where $\Delta t = |t_2 - t_1|$ is the sampling interval. The same approach is applied to the second time series, which leads to $\vec{Y}$. Then, once the data is resampled, Kendall-τ_b is calculated for the newly generated vectors $\vec{X}$ and $\vec{Y}$.

$$\begin{aligned}\tau_b(\vec{X}, \vec{Y}) = \mathrm{corr}\,[&(X_{j+1}, X_{j+2}, \ldots, X_{j+N})\,,\\ &(Y_{j+1}, Y_{j+2}, \ldots, Y_{j+N})]\,.\end{aligned} \tag{2.5}$$

To verify the limits of this approach and the required minimum number of elements in each data set for a reliable calculation of the Kendall-τ_b coefficient, one data set of 25 million true random numbers extracted from Johnson noise and obtained at random.org [145] is used. These numbers are guaranteed to not bear any hidden correlation. A second data set is obtained by randomly scrambling the previous random data set. These data sets provide no information on the sampling. However, an artificial sampling

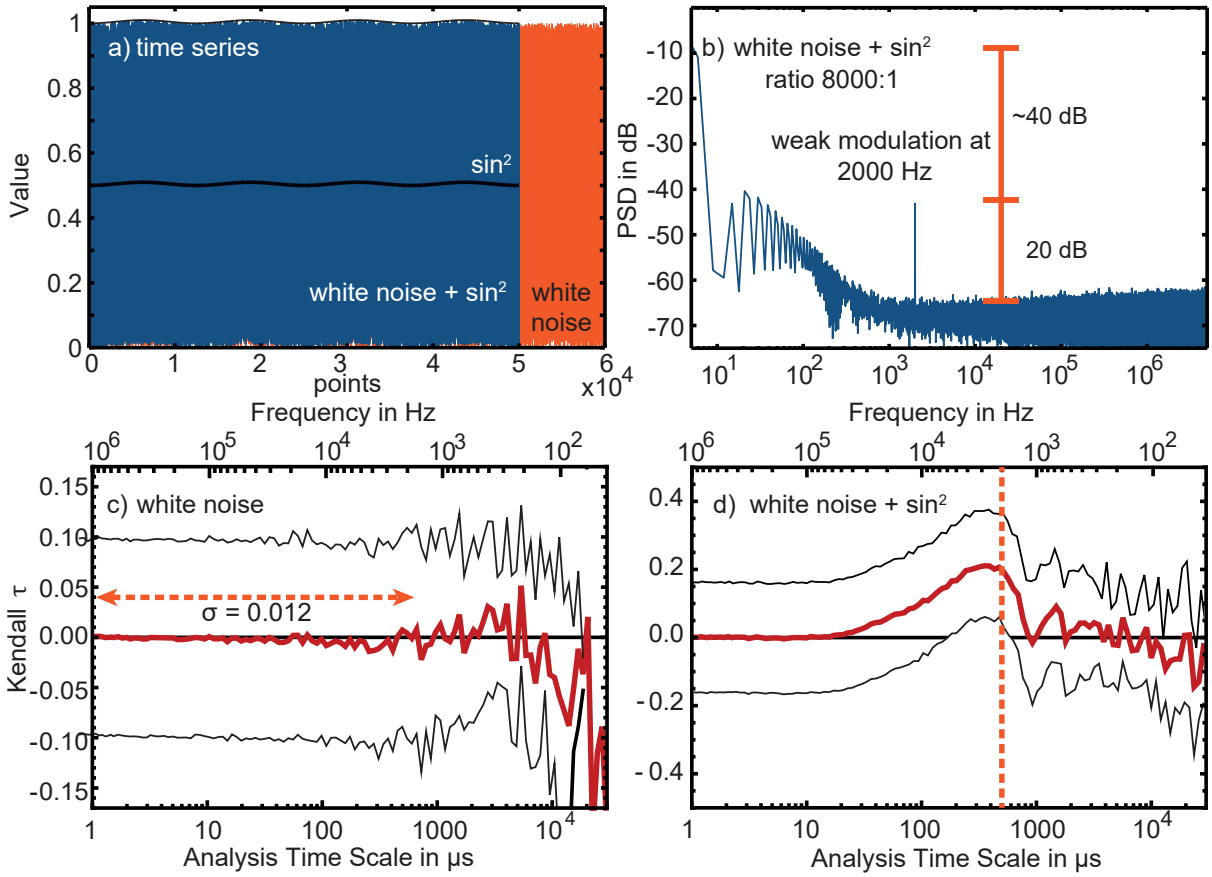

Figure 2.1: Principle of the proposed time-resolved Kendall-τ_b analysis. a) Time series of white noise (orange), sine-squared time series (black) and the product of both (blue). b) shows the PSD of the mixed time series with a weak, 2.000 Hz modulation. c) Using proposed time-resolved Kendall analysis, the Kendall-τ_b coefficient is calculated between two resampled white time series. As no sampling time was given in the original time scale, an artificial time scale is provided that directly compares to the one presented in the analysis of noise in sec. 2.3.3. Here, an acceptance range of up to 10,000 µs on this artificial time scale can be assumed, where the error and hence the deviation from expected zero correlation is within 5 %. This enables to estimate the minimum required number of elements to be compared. d) shows the result of the time-resolved Kendall analysis when applied to two mixed time series created from a sine-squared and different white noise. The respective oscillation at 2.000 Hz is clearly visible in the analysis. In c) and d), the standard deviation is given as the black line.

time is established here that enables to give a region of trust and allows a direct comparison to the results presented later on in section 2.3.3. Adding this artificial time scale has no effect on the correlation strength and only enables a comparable discussion to the application of this methodology later on.

Figure 2.1 a) shows several time series, including the one from above originating from random numbers or white noise (orange), one obtained from a weak simulated squared sinusoid (black) as well as their product (blue). In Fig. 2.1 c), the earlier mentioned white time series are evaluated according to their Kendall-τ_b by following the above methodology. Up to a mere 700 µs time, the deviation from zero and therefore, from the expected lack of correlation between both, stays at roughly 1 % ($\sigma = 0.012$). Between two white time series, no correlation is expected and hence the Kendall-τ_b stays around zero. Nevertheless, above 700 µs, the error continuously increases due to the strongly reduced time series elements that are being compared. Therefore, a region of trust of up to 10.000 µs is given, where the deviation from the expected Kendall's τ_b value of zero is within 5 %. Furthermore, the product of white noise with a weak squared sinusoid is shown in Fig. 2.1 a) (blue) with a respective power spectral den-

sity as shown in b) with a 2.000 Hz modulation. A ratio strength of 8.000:1 can be seen between the white noise and the sinusoid. However, the Kendall-τ analysis is able to resolve the correlation between two of the mixed time series by revealing the sinusoid oscillation through providing a correlation on the respective time scale of 500 µs. This can be seen in Fig. 2.1 d). This assures the validity and sensitivity of this approach.

Compared to traditional Fourier analysis, i.e., the analysis of the power spectral density (PSD), the presented methodology enables also to analyze broadband noise sources such as relaxation oscillations. In particular, while the PSD only enables interpretation and guessing the connection between two similar looking spectral densities by, e.g., assuming a connection between isolated peaks or by attributing peaks to a common particular source, such as lines in the acoustics in a noise spectrum, broadband sources or correlations remain hidden. These can be resolved with the Kendall correlation methodology.

In the noise analysis in section 2.3, the presented methodology for assessing correlation is employed to frequency and amplitude noise extracted from free-running carrier-envelope phase measurements. While this correlation analysis can provide information about interaction of certain parameters, however, the statistical nature of this data is not accessible. To this end, nonlinear time series analysis is introduced further on.

2.2 Principles of Nonlinear Time Series Analysis

Nonlinear time series analysis was developed in the realm of chaos theory, where chaos describes systems in which the future states strongly depend on even small perturbations of the initial conditions. In principle, it is possible to separate systems according to their respective statistical origins, either as a result of a deterministic or a stochastic process. While all future states of a deterministic system can be theoretically described by observation of any single state, for stochastic systems only probabilities for future states can be given [146, 147]. For the former, a typical example is provided by a simple harmonic oscillator that is described by a differential equation. A typical stochastic system, however, is described by probabilities, such as, e.g., a quantum mechanical process that leads to white noise like spontaneous emission, where each event is independent of prior ones.

In reality, a measured times series will always include measurement uncertainty and hence never appear fully deterministic. Measurement uncertainty can be introduced by, e.g., white detection noise as was elucidated in section 1.5.3. Many systems have been found to be rather chaotic in nature and thereby to appear random. However, in principle, these systems are still governed by deterministic processes such as a set of differential equations. Chaos theory enables to differentiate these systems by means of various methods, with the ones presented here relying on phase space reconstruction of the system. This phase space represents all possible - past, present and future - states of the system and is reconstructed from an univariate time series. Considering the phase space of a harmonic oscillator and a damped harmonic oscillator as is shown in Fig. 2.2, the former experiences no loss and represents a closed set of possible states or closed phase space trajectory. The damped harmonic oscillator is characterized as a dissipative system, where the degrees of freedom are minimized as energy is lost over time. This effectively isolates the system's possible evolution to a smaller set of states, which is referred to as an attractor of the system under investigation. Chaos theory characterizes attractor geometry in order to make statements over the system's properties and its future course. One of the most important measures in chaos theory is the correlation dimension D. While the correlation dimension is found to be an integer for a conservative classical system, it is a non-integer in the case of a dissipative or irregular system describing chaotic behavior [148, 149, 150]. In this way, it provides a measure of dimensionality of the system. Interestingly, for a system of purely stochastic behavior, no finite correlation dimension is found. This parameter and others that are used in chaos theory have strict requirements on the properties of the analyzed time series to enable proper interpretation and meaningful phase space reconstruction. As these conditions cannot be guaranteed for the measured time series here, the calculation of those parameters is not carried out for the systems under investigation. Nevertheless, the methods of nonlinear time series provide a qualitative approach that enables a framework for the later applied methodology of differentiating between stochastic and deterministic carrier-envelope phase noise. To this end, a brief introduction into nonlinear time series analysis is provided, in which one of the most famous systems from chaos theory, namely the Lorenz system, is discussed. Further, phase space reconstruction from a measured time series, correlation sum and correlation histogram are introduced. To provide measures to assess the systems' traces of determinism, the method of surrogate data is elucidated.

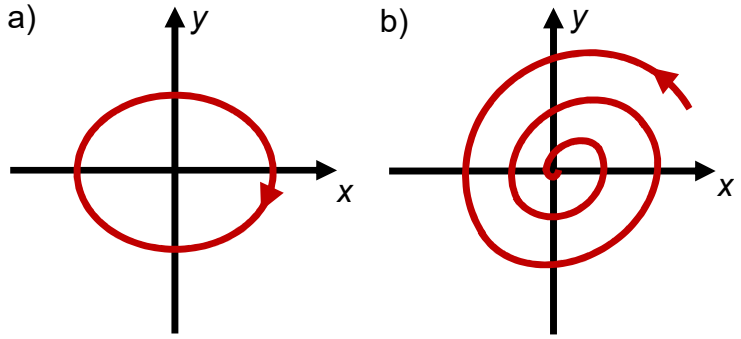

Figure 2.2: Phase space representation of a) a harmonic oscillator and b) a damped harmonic oscillator. While the trajectory of the former circles in a closed loop, the latter represents a dissipative system, which effectively leads to a minimization of the degrees of freedom.

2.2.1 The Lorenz Attractor and Chaos

The most prominent example for a deterministic chaotic system was derived by Lorenz [151], which describes a fairly simple model of a hydrodynamic system that involves a set of coupled differential equations

$$\dot{X} = -\sigma X + \sigma Y \tag{2.6}$$

$$\dot{Y} = rX - Y - XZ \tag{2.7}$$

$$\dot{Z} = -bZ + XY \tag{2.8}$$

where $\sigma, r, b > 0$. Commonly chosen values are $\sigma = 10, r = 25$ and $b = 8/3$. In this case, the above equations define a system that is deterministically chaotic. The respective Lorenz attractor features a warped bow-tie shape as is shown in Fig. 2.3 for two initial states (blue and red). Then, already a small variation in the initial states leads to deviating trajectories in the phase space. Similar to the earlier presented 2D damped harmonic oscillator, which is ending in a single point (1D), the 3D coupled Equations (2.6)–(2.8) lead to a Lorenz attractor that is characterized by isolating its trajectory in a dimension between 2 and 3 and therefore restricts itself slightly out of a plane. The actual non-integer attractor dimension can be calculated and is roughly 2.06 [152], which depends on the choice of parameters σ, r and b. Furthermore, in both mentioned systems, the evolution into a sub-space that forms the attractor implies a reduction of degrees of freedom due to the dissipative evolution of the system [152]. While the phase space was introduced on the example of the harmonic oscillator and the Lorenz system, it is not guaranteed that it can be reconstructed for any given time series, especially from a measured one. This is further elucidated in the upcoming section.

2.2.2 Phase Space Reconstruction

Based on the idea of Packard et al. [153], Takens was able to formalize the phase space reconstruction that enables to reconstruct the dynamics of a system from a measured, univariate time series [154]. Despite the measurement of only a single quantity, it could be shown that the phase space reconstruction is topologically identical to the complete dynamics of the system. This can be illustratively explained by considering the coupled Equations (2.6)–(2.8) of the Lorenz system. With evolving dynamics of the system, X contains also information about the change of Y and Z. This connection provides already

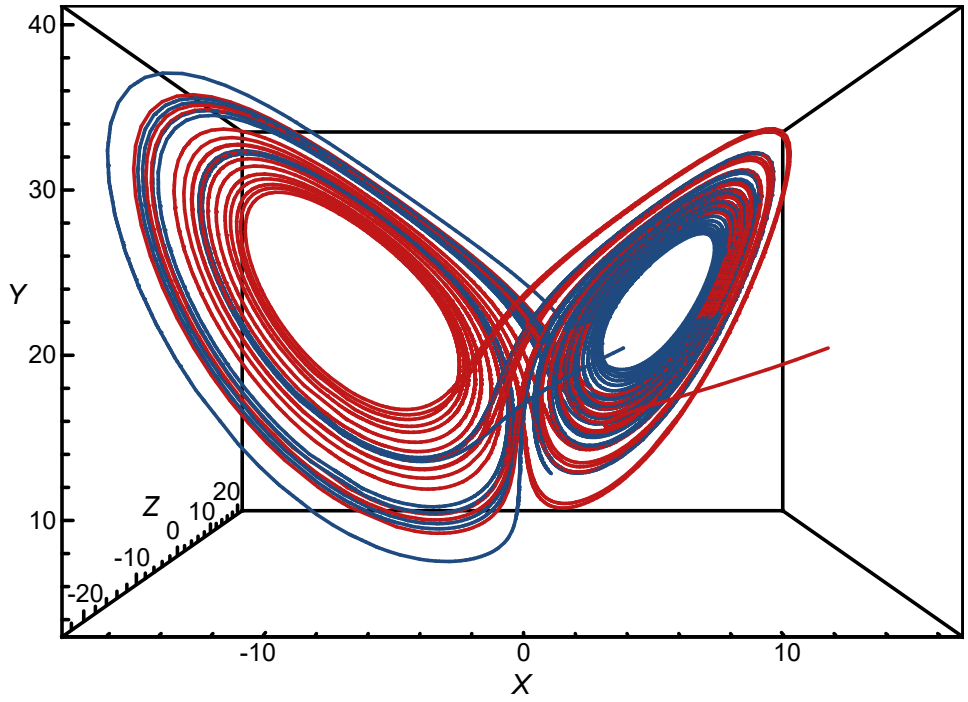

Figure 2.3: Phase space representation of the Lorenz attractor trajectory for two different initial conditions (15,-5,20) in red and (5,-5,20) in blue with parameters $\sigma = 10, r = 25, b = 8/3$.

enough information to distinguish between stochastic or deterministic dynamics within the system [154]. Hence, reconstruction of the phase space can be realized by measuring a single variable of a system. For real systems, this is not straightforward.

Suppose a system under investigation that is expressed by a time series $y(t)$ consisting of N sampled points separated by the sampling time Δt

$$y(t) = \{y(0), \ldots, y(k\Delta t), \ldots, y((N-1)\Delta t)\} \qquad \text{with} \quad (k = 1, 2, \ldots, N-2). \tag{2.9}$$

The phase space is then reconstructed by the formation of a collection of embedding vectors $\mathbf{y}_i$ of length m, with m being the embedding dimension and with embedding delays τ_{embd} such as

$$\mathbf{y}_i(t) = \{y(t), y(t+\tau_{\text{embd}}), y(t+2\tau_{\text{embd}}), \ldots, y(t+(m-1)\tau_{\text{embd}})\}, \tag{2.10}$$

where each of the i embedding vectors $\mathbf{y}_i$ consist of m elements from the original time series $y(t)$ that were originally separated by τ_{embd}. The collection of embedding vectors is then created by starting each embedding vector at a different time t. In this way the phase space is reconstructed by describing the system evolution in form of a trajectory as can be seen for the case of the Lorenz attractor in 2.3,

Choosing the proper embedding delay τ_{embd} and embedding dimension m defines the quality and resolution of the phase space representation of the time series and is crucial for a successful reconstruction. To find an appropriate τ_{embd}, the first minima of the autocorrelation [147] and mutual information [155] can be used. To obtain a proper embedding dimension m usually the false nearest neighborhood method [156] is employed as an indicator. The choice of m and τ_{embd} is of crucial importance for applications within chaos theory, such as the calculation of the correlation dimension. Nevertheless, it is also argued that the data covered by the product of the embedding dimension and delay $m \times \tau_{\text{embd}}$, also referred to

as the time window length, is of higher relevance [157, 158] for a suitable reconstruction of the phase space and interpretation of statistical properties. In this thesis a similar approach to the latter is taken in combination with the restriction on identifying traces of determinism or the lack thereof. Hence, the choice of m and τ_{embd} is not of definite importance by the design of the analysis. This is explained in detail in 2.2.5.

Another important requirement for enabling the phase space reconstruction from a single, univariate time series is the need for stationarity. In order to describe the full dynamics of a system the time series has to be long enough to incorporate even the slowest changes of the system [147]. In this sense, the time series needs to be stationary to allow differentiating between randomness and determinism. To assess the stationarity of the time series a running mean is typically calculated that should not deviate from the full time series mean by more than 3 standard deviations. A similar approach is used during the preparation of the employed time series of CEP noise in 2.2.5. Once these conditions are fulfilled, the next step is to make use of the reconstructed phase space.

2.2.3 The Correlation Histogram

The earlier shown phase space representation of the Lorenz attractor clearly shows the distinct uniqueness of each trajectory point or state as no crossing can be seen. This conditions is fundamental to deterministic systems as it unambiguously defines the direction of evolution of the system. In a stochastic system, however, trajectories can cross and multiple outcomes are possible. For simplicity, considering a three-dimensional phase space, a deterministic system shows trajectories that are much closer to each other compared to a stochastic system. The latter has many more possibilities to extend through space, and therefore, it does not confine itself in some lower dimensional sub-space. In this sense, when considering sub-spaces of the full phase space, a sphere around a state in the deterministic system includes more neighbors as in a stochastic system. This idea is quantified by the correlation histogram, where the phase space trajectories are assessed according to their similarity and hence how far the states are from each other. With increasing distance r from one starting state, the correlation sum $C(r)$ is calculated [152] for all states of the system, which results in

$$C(r) = \frac{1}{N^2} \times \{\text{pairs}(\mathbf{y}_i, \mathbf{y}_j) \quad \text{where} \quad r \geq |\mathbf{y}_j - \mathbf{y}_i|, (i \neq j)\}, \tag{2.11}$$

with the embedding vectors from Eq. 2.10 are used and $|\mathbf{y}_j - \mathbf{y}_i|$ represents the Euclidean difference between $\mathbf{y}_j$ and $\mathbf{y}_i$. Equation 2.11 provides access to the similarity of phase space trajectories by evaluating the probability of finding two embedding vectors within a m-dimensional sphere of radius r around a state of the system.

When only spherical shells with width δr around a state along the trajectory are considered, the correlation histogram enables to count only small increments or shells around a particular state, which leads to

$$C_H(r) = \frac{1}{N^2} \times \{\text{pairs}(\mathbf{y}_i, \mathbf{y}_j) \quad \text{where} \quad r \geq |\mathbf{y}_j - \mathbf{y}_i| \geq r - \delta r, (i \neq j)\}. \tag{2.12}$$

When considering the phase space distribution of system states it has to be ensured that temporal neighbors, which lead to short Euclidean distances, are not included and thereby do not contribute to the correlation histogram for small r. To this end, the minimum distance w is introduced to enable exclusion

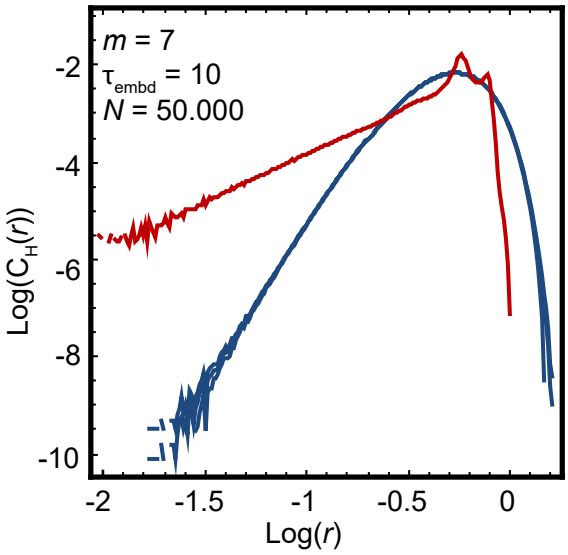

Figure 2.4: Correlation histogram of the X-component of the Lorenz time series(red) with $m = 7$, $\tau_{\text{embd}} = 10$ using effectively 50.000 points. In blue, 10 stochastic surrogates of the original Lorenz series are shown.

of temporal neighbors along the trajectory path. In general, this distance w is chosen to extend over several autocorrelation lengths. Using the same approach of phase space reconstruction and assessing the metric differences between embedding vectors enables to analyze the correlation histogram

$$\tilde{C}_H(r) = \frac{1}{(N-w)^2} \times \{\text{pairs}(\mathbf{y}_i, \mathbf{y}_j) \quad \text{where} \quad r_{\text{bin}} = |\mathbf{y}_j - \mathbf{y}_i|, (j-i > w)\}\,. \tag{2.13}$$

Here, the distance r_{bin} is set to be of discrete nature, which can be carried out as the original data is limited in resolution and binning of various values of r is conventionally done to minimize computational complexity. For simplicity, r_{bin} is further referred to as r. Based on the correlation histogram from Eq. 2.13, Grassberger and Procaccia [159, 160] developed a methodology, namely the Grassberger-Procaccia algorithm, that allows to characterize attractors by means of a single time series by using the correlation sum

$$C_{\text{GPA}}(r) = \frac{1}{(N-w)^2} \sum_{i=j+w}^{N} \Theta(r - |\mathbf{y}_i - \mathbf{y}_j|)\,, \tag{2.14}$$

where Θ is the Heaviside step function. While for small metric differences r, the correlation sum shows a power-law dependence for a deterministic signal with $C_{\text{GPA}}(r,m) \propto r^{D_c}\ \forall\ m$, where D_c is the correlation dimension, a stochastic signal gives a $C_{\text{GPA}}(r,m) \propto r^m\ \forall\ m$ behavior that increases with the embedding dimension. Nevertheless, for estimating statistical properties of a time series the correlation histogram can also be used. Similar to this approach, the number of counts in the correlation histogram at short distances is used to compare deterministic and stochastic signals. Fig. 2.4 (red) shows the correlation histogram of the Lorenz system for $\tau_{\text{embd}} = 1$ and $m = 7$ calculated by employing the above mentioned correlation histogram. A clear trend of the counts is seen for increasing r. Therefore, the phase vector representing the system in the phase space already provides enough information to distinguish between deterministic and stochastic dynamics by employing part of the Grassberger-Procaccia algorithm, provided that some reference exists. This is the topic of the next section, where the method of surrogate data

is introduced.

2.2.4 The Surrogate Method

In order to classify the statistical properties of a time series by means of the correlation histogram at least one known reference, either of purely deterministic or stochastic nature, is required. It was elucidated before that a deterministic system shows a higher probability of close-proximity points or states within its phase space representation and thereby results in a higher count in the correlation sum compared to a stochastic time series. A way to classify this difference is given by the surrogate method. To this end, a baseline is established by means of creating a purely stochastic system that originates from the original time series. In this sense, a null hypothesis is formulated that declares the original time series to be originating from a stochastic Gaussian process [161, 162]. In this case, the original times series has an underlying stochastic probability distribution that is normally distributed in the limiting case of infinite elements. Then, an attempt is made to reject this null hypothesis by the method of surrogate testing, where surrogates are created with data from the original time series, but are randomly shuffled and hence purely stochastic. The null hypothesis is rejected if the correlation histograms differ significantly for small Euclidean differences.

To ensure direct comparability of the surrogates and the original time series, certain requirements for creating surrogates need to be set. First, linear attributes of the original need to be maintained within the surrogates. This requires identical linear descriptive statistics, linear histograms and nearly identical power spectra to the original time series. However, while these statistical properties need to be maintained, any determinism that is present in the original is removed. To this end, phase randomization of the original data is carried out. This process may induce changes of the above mentioned linear statistics during the creation of the surrogates. Therefore, power spectral density as well as the autocorrelation of the surrogates are adjusted to match the ones of the original time series in an iterative process [42, 161]. The creation of the surrogates includes three steps. First, amplitude-adjusted Fourier transform of the original time series is carried out [161]. After Fourier transformation, each complex amplitude is multiplied by a random phase factor that is extracted from true random Johnson noise [145] mapped onto the interval $[0, 2\pi[$. Subsequently, inverse Fourier transformation is done, while previously maintained phase symmetry warrants a real-valued result. To obtain the same power spectrum of the randomized phases, the previously carried out rescaling needs to be reversed. Second, once randomization is completed, an iterative approach repeating the previous steps is taken to adapt the power spectral density of the surrogate to the one of the original. Once sufficiently realized, the third step involves the matching of the autocorrelation function of both by simulated annealing. A more rigorous and detailed description on the surrogate formation method can be found in the dissertation of Birkholz [42] and the original paper by Theiler [161]. The methods of nonlinear time series are further extended to enable time-resolved analysis of CEP noise.

2.2.5 Time-Resolving Nonlinear Time Series Analysis to Distinguish Statistical Properties

In this thesis, the nonlinear time series analysis is further extended in order to analyze CEP noise on different time scales. To this end, a methodology is established that is later used to analyze free-running

CEP noise of various oscillators with the goal of differentiating deterministic and stochastic noise with time resolution. This is exemplary carried out for the earlier introduced X-component of the Lorenz time series as well as a purely stochastic time series.

In the first step several time series are obtained, of which each covers a different time span. To this end, the original series $x(t_i)$ of length N is resampled by averaging over segments of length M_j, which leads to the formation of a new time series

$$\hat{X}_j = \{X_1, \ldots, X_z, \ldots\} \quad \text{with} \quad X_z = \frac{1}{M_j} \sum_{i=(z-1)M_j+1}^{zM_j} x(t_i) \quad \forall z \in \mathbb{N} \leq N/M_j \tag{2.15}$$

$$\text{where} \quad M = \{1, 2, \ldots, 19, 20, 30, 40, \ldots, M_j, 200, 250, \ldots, 500\}\,. \tag{2.16}$$

In this way, here, e.g., 38 different time series of the original one are generated, where each time series is resampled on a different time scale. By subsequently removing the moving average over each point z in each time series by considering 250 points prior and 250 points after (acausal moving average), a stationary time series is established that can be used for reconstruction of the phase space. This means

$$X^*_{j,z} = \hat{X}_{j,z} - \text{Mean}\left\{\hat{X}_{j,z-250}, \ldots, \hat{X}_{j,z}, \ldots, \hat{X}_{j,z+250}\right\}. \tag{2.17}$$

Then, nonlinear time series analysis in combination with the surrogate method is applied to each time series as was presented in section 2.2.3 using Eq. 2.13. This results in a total of $m \times M_{\text{total}} \times (N_{\text{surr}} + 1)$ histograms $C_{\text{H}}(r)$ to be computed. One such histogram with its respective 10 surrogates can be seen in Fig. 2.5 c) for the Lorenz time series with M = 10, where also the selection range at small Euclidean distances is indicated by the green area. Subsequently, each histogram is accumulated starting at short Euclidean distances. This leads to the correlation sum. Then, the statistical significance is calculated in an interval as marked by

$$S = \frac{C_{H,r} - \overline{C}_{H,\text{surr},r}}{\sigma_{\text{surr},r}} \quad \text{with} \quad r \in [\bar{r}_{\text{surr}} : C_{H,\leq \text{r}} = (0.2 + 0.002 \times m) C_{H,\text{r}_{max}}]\,, \tag{2.18}$$

where m is the embedding dimension, $\overline{C}_{H,\text{surr,r}}$ the mean of all surrogate counts at the particular distance r and $\bar{r}_{\text{surr}}$, the distance r at which all surrogates have been found to result in counts as they do not necessarily start at the same bin. The range of selection is indicated in Fig. 2.5 c). While the lower border is set to vary with the beginning of all surrogate counts $\bar{r}_{\text{surr}}$, the upper limit is essentially dynamic and is initially placed where 20% of all counts $C_{H,\text{r}_{\text{max}}}$ are found. The upper limit is set to increase with the embedding dimension to account for changes in the histogram. In this manner, the calculation of the statistical significance is found reliable over the strongly varying phase space characteristics seen when reconstructing the phase space for increasing embedding dimensions. The extraction range of the statistical significance varies with the system under investigation and hence the resulting histogram. Therefore, it is later chosen during the investigation of CEP noise in between 1% and 10% of the maximum count found in the correlation sum.

By repeating this assessment of the statistical significance for all computed histograms, a time scale can be established, as each time series is segmented by different temporal parts of the original. This time scale ranges from the minimum sampling time dt up to $m \times dt \times M_{\text{max}}$, where M_{max} is the highest element of M used in the analysis. Normally, it is necessary to discard results from small values of m, the

embedding dimension, as the vector is too short to properly resolve the systems properties in the phase space. Then, by subsequently averaging over all values of statistical significance for one particular time unit, an estimate of the stochastic properties of the time series on this time scale can be given, such as is presented in Fig. 2.5 d), where the mean statistical significance is given as a function of an artificial time scale with $dt = 0.01$. This methodology has been carried out for the Lorenz system as well as pure stochastic noise taken from real random numbers [145] as can be seen in Fig. 2.5. It is shown that a distinct difference in statistical significance between the deterministic Lorenz time series and the stochastic noisy time series exists. While for the former the statistical significance stays well within the range of 10^3-$10^5 \sigma_{\mathrm{surr}}$ over more than 10 time units, it clearly stays below 5 σ_{surr} in the case of the stochastic time series. This confirms the validity of this approach despite the strong averaging present.

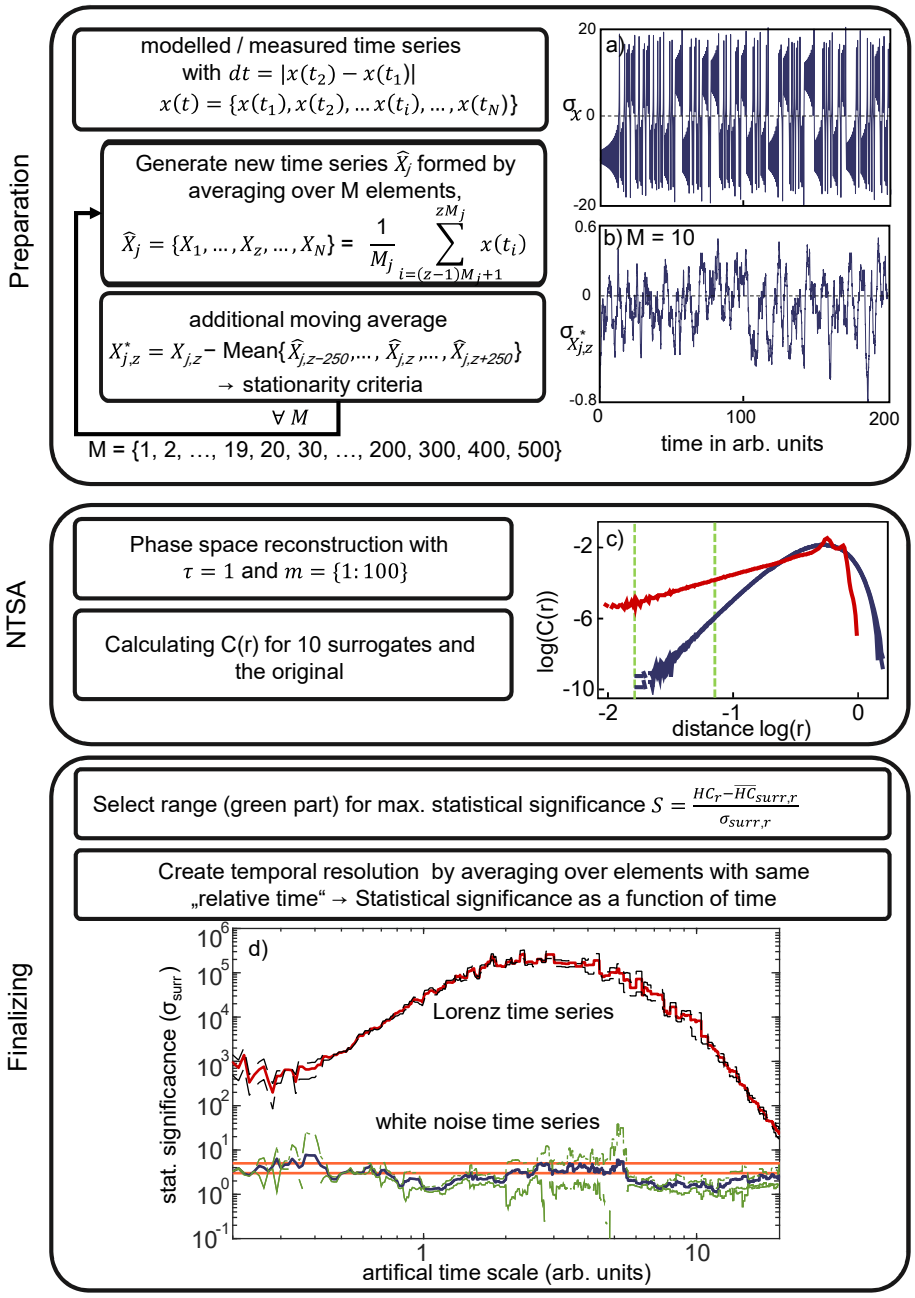

Figure 2.5: The three main steps for the proposed analysis methodology on the example of the Lorenz time series and a stochastic time series are shown. Out of the original time series (see a)), by averaging over M elements, subsets are established that effectively describe the system on a different time scale. To ensure stationarity moving average is carried out as can be seen in b) for $M = 10$ for the case of the Lorenz system. Then, nonlinear time series analysis is achieved as presented earlier in section 2.2.3, which results in a total of $m \times X_j^* \times (N_{surr} + 1) = N_{total}$ histograms to be computed. One such histogram is the one shown in c), where also the selection range at small Euclidean distances is indicated by the green area. Subsequently, for each histogram the statistical significance is calculated. By repeating this step for all computed histograms, a time scale is established. Furthermore, averaging over all statistical significances at one particular time unit as well as for all computed histograms falling into that range thus enables representation over time as is shown in d). Clearly, the difference in statistical significance for both time series can be seen. While the statistical significance resides within a range from 10^3 to $10^5 \sigma_{\text{surr}}$ for the Lorenz system, the purely stochastic time series stays below 5 σ_{surr}.

2.3 Comparative Noise Analysis of Different Laser Sources

Earlier introduced methodologies are further applied to the free-running residual CEP noise of various laser oscillators in order to gain insights into the intra-cavity sources that govern the CEP. In addition, traditional noise analysis by power spectral density as well as amplitude and frequency noise densities is carried out. In this sense, a deeper understanding of why some lasers are readily CEP stabilized and others show severe residual phase noise inhibiting proper stabilization is established. This facilitates a greater range of potential sources for frequency comb applications and as a front-end for high-power amplifiers.

After introducing the analyzed laser sources and providing their measured f_{CE} beat note, the preparation of the time series is given. Subsequently, the coupling between the carrier-envelope frequency and amplitude noise is analyzed using presented time-resolving Kendall-τ_b methodology from 2.1.1. Then, the nonlinear time series results are provided, which is followed by a discussion of possible coupling mechanisms. Finally, one particular laser is investigated, in which the source of broad CEP noise is attributed to its mode-locking mechanism.

2.3.1 Analyzed Laser Sources

The comparative study involves the measurement of the free-running CEP of three differently mode-locked fiber lasers and a Ti:sapphire oscillator based on Kerr-lens mode-locking. While two of the employed fiber lasers are based on artificial saturable absorbers, the third actually incorporates an additional device, namely a saturable absorber mirror (SESAM) to regulate self-amplitude modulation. The first oscillator is a home-built Yb:doped fiber laser [163] that achieves mode-locking by nonlinear polarization rotation (NPR) [82], similar to the principle presented in section 1.3.1. However, the employed NPR laser is actually comprised of two lasers, where the repetition rates of both are stabilized against each other by balanced optical cross-correlation [164]. While the first Er:doped fiber laser employs the earlier mentioned SESAM (Er:fiber A), the second one (Er:fiber B) incorporates a figure-of-eight cavity design [165] for mode-locking, where an additional nonlinear amplifying loop mirror (NALM) acts as an artificial saturable absorber and effectively limits self-amplitude modulation of the pulse. Nevertheless, the mode-locking designs presented here are principle-based only, as the latter two are commercial products, which do not reveal their technical details. However, the insights gained by this analysis can be nevertheless manifold as will be shown later. Table 2.3.1 provides an overview of common laser parameters for all presented laser sources.

The CEP is easily compromised by different noise sources as has been introduced in section 1.5. Referring to the laser by its mode-locking mechanism is only for convenience and does not imply that, e.g., a NPR laser built with Yb:doped fiber or Er:doped fiber share similar noise characteristics. Nevertheless, as is shown in this systematic investigation, the mode-locking mechanism plays a key role.

2.3.2 Extraction of the CEP Noise

With the exception of the Yb:doped fiber laser, where only the differential CEP between two lasers was measured by the optical heterodyne beat method [98, 166], the CEP of the three other oscillators was obtained by employing f-2f interferometry. In the former case, optical heterodyne beat detection

Laser		Ti:Al_2O_3	Yb:fiber	Er:fiber A	Er:fiber B
Repetition rate	f_{rep} (MHz)	84	157	80	250
Average power	P_{out} (mW)	520	70	1	3
FWHM pulse duration	τ (fs)	10	70	500	72
Upperstate lifetime	τ_{rad} (ms)	0.004	1-2	8-10	8-10
Mode-locking		KLM	NPR	SESAM	NALM
CEP measurement		f-$2f$	HD	f-$2f$	f-$2f$
6 dB noise bandwidth	$\Delta\nu$ (kHz)	50	300	1200	50
Time-bandwidth product	$\Delta\nu \times \tau_{\mathrm{rad}}$	0.2	450	11000	450
Sampling rate	τ_s (MHz)	25	25	50	50

Table 2.1: Common parameters of the employed lasers and the CEP measurement in the comparative study.

provides information about the optical phase noise that is only unambiguously CEP noise within the locking bandwidth of the repetition rate lock of both oscillators. In this sense, if the repetition frequency f_{rep} of both combs $f_1 = f_{\mathrm{rep}} + f_{\mathrm{CE_1}}$ and $f_2 = f_{\mathrm{rep}} + f_{\mathrm{CE_2}}$ is perfectly locked, the measured beat note is actually comprised of the difference of both $f_{\mathrm{CE,measured}} = f_{\mathrm{CE_1}} - f_{\mathrm{CE_2}}$. The avoidance of nonlinear processes in this approach leads to a strongly reduced influence of shot noise, which can be detrimental in f-$2f$ interferometry. Nevertheless, despite the potential drawbacks of those nonlinear processes, in particular supercontinuum generation has been seen to be actually beneficial for noise analysis as it is known to strongly amplify amplitude fluctuations at the input [167], which enables to detect even weak correlations between amplitude and phase.

The free-running CEP beat note of all four lasers systems was situated at roughly 10 MHz and subsequently oversampled by at least a factor of 2.5 for 1 s, leading to 25 or 50 million data points, respectively. Using f-$2f$ interferometry provides an amplitude modulation $u(t)$ with the carrier-envelope offset frequency f_{CE}. After Fourier transform and normalization, this leads to the beat notes as is shown in Fig. 2.6, where the 6 dB width of these rf beat notes represents the optical full width at half maximum (FWHM). The beat notes strongly vary in widths ranging from 50 kHz for the Ti:sapphire laser and beyond 1 MHz for the SESAM mode-locked Er:doped fiber laser A. Interestingly enough, the NALM mode-locked Er:doped laser's beat note width is comparable to the one obtained with the Ti:sapphire laser, which was seen before for other fiber lasers [168, 169]. Subsequently, the beat notes are isolated within a range Δf until the beat note reaches the noise floor. This width Δf determines the resolvable frequency contributions. The Fourier filtering, also referred to as the Takeda algorithm [142], can be described by

$$v(t) = \int_{f_{CE}-\Delta f}^{f_{CE}+\Delta f} \exp(2\pi i f t) \int_0^T u(t') \exp\left(-2\pi i f t'\right) \mathrm{d}t' \mathrm{d}f, \tag{2.19}$$

where T represents the duration of the time series. Then, $v(t)$ provides access to the instantaneous amplitude and frequency

$$a(t) = 2|v(t)| \quad \text{and} \quad f(t) = \frac{1}{2\pi} \frac{\mathrm{d}\arg[v(t')]}{\mathrm{d}t'}\bigg|_t = \frac{1}{2\pi} \frac{\mathrm{d}\varphi}{\mathrm{d}t'}\bigg|_t, \tag{2.20}$$

respectively. These two time series provide the basis for the upcoming correlation analysis employing

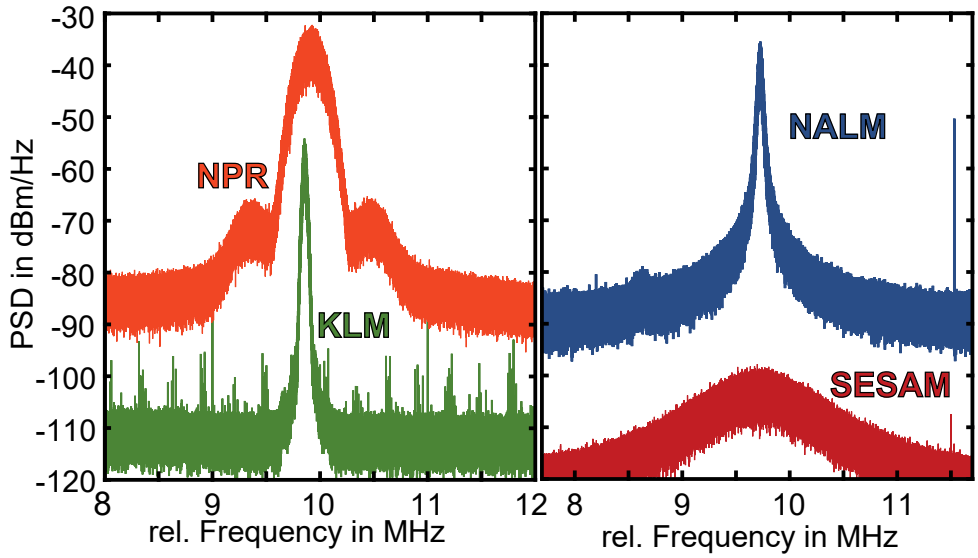

Figure 2.6: Power spectral density of the free-running beat notes of presented lasers, which are identified by their respective mode-locking method. With the exception of the NPR beat note that was obtained by the optical heterodyne beat method, the other three were measured using f-$2f$ interferometry. Here, the normalized noise equivalent bandwidth[3](NENBW) = 1.5 Bins and resolution bandwidth (RBW) = 5.33 Hz is given.

the Kendall-τ_b rank coefficient. However, the phase term $\varphi = \arg[v(t')]$ is further used for the nonlinear time series. To this end, the phase is concatenated by correcting the 2π shifts and subsequently, the linear trend is removed. Furthermore, the first and last 200 points are discarded, as Fourier transform ringing needs to be avoided due to possible artifacts.

[3]In order to avoid ringing during Fourier transformation as a result of a limited measurement time, the use of filters is typically required. The normalized equivalent noise bandwidth (NENBW) is used to account for a window-dependent signal-to-noise ratio and ensures equal noise powers of both, filtered and unfiltered signal. It is expressed in terms of frequency bins and defines here the use of a Hanning window filter.

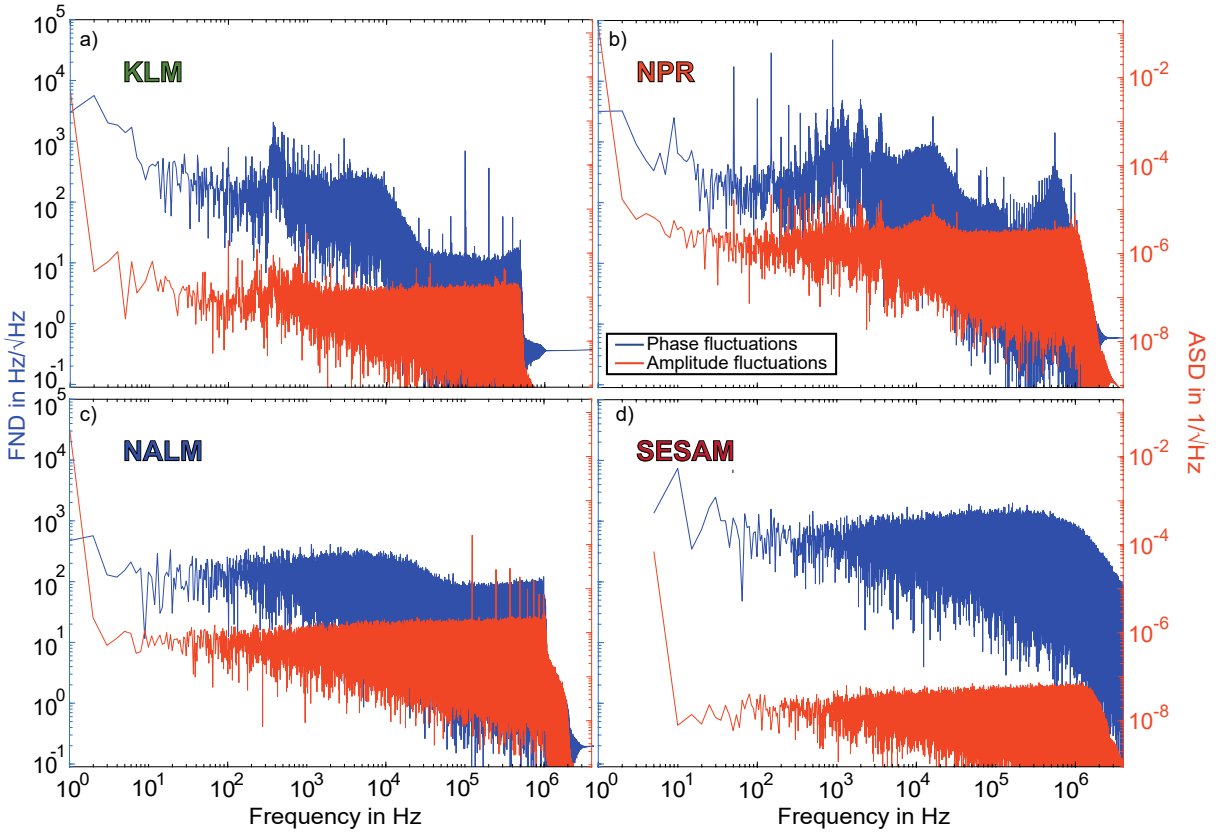

Figure 2.7: Frequency noise density (blue) and amplitude noise density (orange) of all isolated beat notes. a) Ti:sapphire oscillator based on Kerr-lens mode-locking, b) Yb:doped fiber laser based on nonlinear polarization rotation, c) Er:doped fiber laser mode-locked by a NALM and d), SESAM mode-locked Er:doped fiber laser.

2.3.3 Carrier-Envelope Amplitude and Frequency Correlation Analysis

Employing the time-resolved Kendall-τ_b correlation analysis approach (see section 2.1.1), the correlation between carrier-envelope amplitude $a(t)$ and frequency noise $f(t)$ is analyzed. By separately resampling both time series according to Eq. 2.4, the Kendall-τ_b is calculated for a time frame ranging up to nearly 10 ms as can be seen in Fig. 2.8. While with increasing time scales, the number of elements compared by the Kendall-τ_b algorithm is reduced, values over 1 ms are increasingly unreliable. Nevertheless, restricting the discussion to time scales below 1 ms essentially reveals two different trends. For the KLM and NPR oscillators a strong, on increasing time scales strengthened correlation is found that quickly rolls off above the millisecond time scale. However, for the Er:doped laser systems based on SESAM and NALM mode-locking, a weak and negligible correlation nearly independent of frequency is observed, respectively. The former trend of the KLM laser especially pronounces the low-pass filtering effect of the Ti:sapphire gain medium, where fluctuations below the upper-state lifetime of about 4 µs cannot be followed by the laser anymore. In the case of the NPR laser, strong correlation is reaching well below the upper-state lifetime, which is around 1-2 ms. However, one reason for high-frequency and amplitude correlation can be the earlier explained laser response bandwidth. This bandwidth can be larger than the upper-state lifetime and depends on the nonlinear loss induced to saturate the self-amplitude modulation (SAM) that enables to form a stable net gain window [127]. Another potential reason are thermally-induced refractive index changes in the gain medium. Interestingly, such coupling effects are not seen

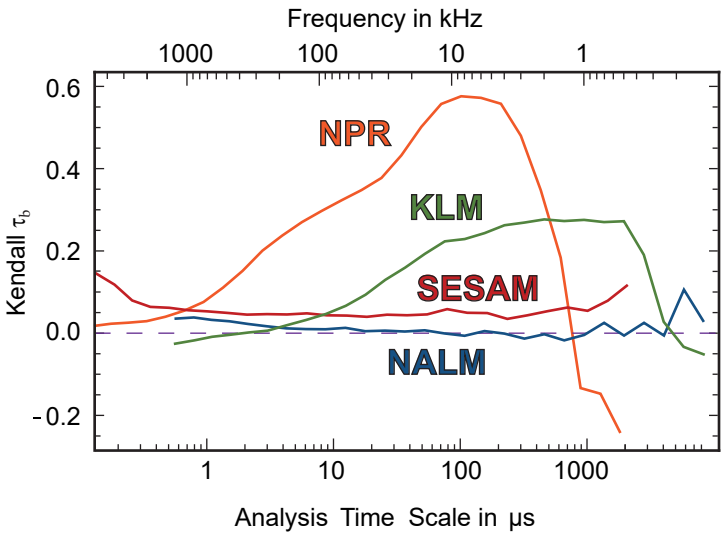

Figure 2.8: Kendall-τ_b analysis carried out for introduced oscillators. Two trends are essentially visible. While the NPR and KLM laser show a frequency-dependent relatively strong correlation, the SESAM and NALM-based Er:doped oscillators show only weak or no correlation, independent of frequency.

in the Er:doped fiber lasers. While the SESAM-based oscillator shows a constant 5% correlation almost over the whole analyzed time period, the NALM oscillator result indicates no correlation to be present at all. The found correlation of the former is further analyzed in the later part of this chapter, where the SESAM is suspected to facilitate conversion of intra-cavity amplitude noise to phase noise.

2.3.4 Nonlinear Time Series Analysis of Residual CEP Noise

After gaining insight into frequency to amplitude coupling of the lasers involved in the comparative study, the statistical nature of the carrier-envelope phase noise is further analyzed. To this end, the carrier-beat note is isolated by the Takeda algorithm according to Eqn. 2.19 and subsequently, the noise is extracted as discussed in section 2.3.2. This is followed by resampling the time series and additionally, averaging by employing a moving window (see section 2.2.5 for details). Histograms for the original time series and 15 surrogates are calculated and subsequently, the statistical significance is extracted for a fixed range of 1 % to 10 % accumulated counts beginning from the shortest distance in the phase space. After averaging over statistical significances resulting from different data series within the same respective time range, the graphs shown in Fig. 2.9 are obtained. In order to differentiate between rather stochastic and fairly deterministic nature, a transition region needs to be established. To this end, the commonly chosen 3-5 σ_{surr} range is selected that enables at least 99.73 % probability (assuming a normal distribution) to reject the null hypothesis that the original time series is originating from a stochastic process. Therefore, above and beyond this range determinism can be concluded to be present in the time series and is gaining strength with increasing σ_{surr}. This helps to guide to the origin of noise sources as deterministic noise is typically a result of a technical origin, while, e.g., quantum noise would reveal itself as stochastic contributions. It is important to note that even a purely deterministic system in the presented experiments will show some traces of stochastic behavior as the measurement-induced uncertainty originating, e.g., from white detection noise inevitability leads to spurious white contributions. The statistical evidence over time shown in Fig. 2.9 for the four different oscillators' residual CEP noise bears two interesting trends. While the Er:doped oscillators (SESAM, NALM) are mostly well below a statistical significance

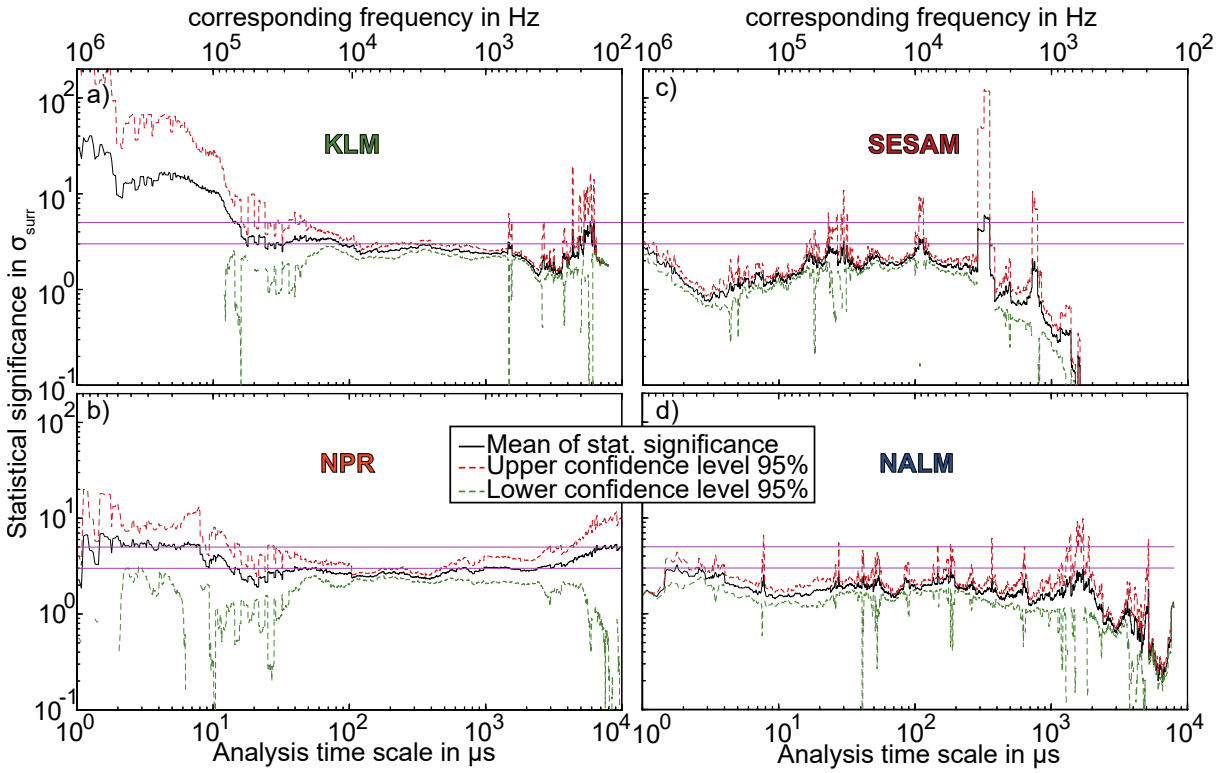

Figure 2.9: Calculated statistical significance over time with corresponding frequencies for in a) the KLM, b), NPR, c) SESAM, and d) NALM laser. Additionally, the 95 % confidence intervals are indicated.

of 3 σ_{surr}, with both showing severe stochastic behavior above 1 ms, this result is not seen for the NPR and KLM laser, where regimes above this limit of $\sigma_{\text{surr}} > 3-5$ exist. Especially the SESAM-based oscillator shows a strong indication for broad stochastic noise with a severe roll off to purely stochastic noise above a millisecond.

2.3.5 Noise Analysis Discussion

The presented results of the novel approaches in combination with the common spectral densities of the CEPs' amplitude and frequency lead to several conclusions. The Ti:sapphire laser clearly confirms the expected low-pass filtering effect in the time-resolved Kendall analysis, where no correlation above the upper-state lifetime of roughly 4 µs can be seen between amplitude and frequency noise. Furthermore, the correlation is receding above several milliseconds. The same picture emerges in a trend of correlation between both amplitude spectral densities in Fig. 2.7, where especially in the acoustic range (50 Hz - 1 kHz) several peaks coincide. These acoustics are even visible in the nonlinear time series analysis in Fig. 2.9 a) indicating a deterministic origin. Even if the statistical significance is not reaching well above 3-5 σ_{surr}, determinism can be hidden below strong stochastic noise originating from ASE or even shot noise occurring during detection. Nevertheless, the strong beat note exceeding 50 dB substantially lowers the influence of the latter. Contribution from (amplified) spontaneous emission in the form of Schawlow-Townes frequency noise can be estimated using Eq. 1.61 to within $8\times10^{-4}\,\text{Hz}/\sqrt{\text{Hz}}$, while additional timing jitter frequency noise according to Eq. 1.65 [87, 132] is limited to roughly $2\times10^{-2}\,\text{Hz}/\sqrt{\text{Hz}}$. Both are well below the measured frequency noise density shown in Fig. 2.7 a) by several orders of magnitude. Despite adding technical noise sources typically revealing themselves as having a rather

limited bandwidth, white noise is seen to be present. Hence, detection noise could still pose a problem. Nevertheless, the estimated shot noise limitation is only strong enough for high Fourier frequencies above 3×10^5 Hz.

Another potential source of the strong noise in the free-running measurement is amplitude-to-phase coupling that well exceeds the quantum limitation. The origin of this are most likely pump-power fluctuations as has been seen in other cases [170, 171, 172]. These energy fluctuations couple to phase noise via the Kerr effect [173, 174] and can lead to substantial phase noise if not damped. However, damping occurs naturally at the relaxation oscillation in the laser gain media, thereby limiting amplitude-to-phase coupling. This may explain the seen time-bandwidth product coming close to a Lorentzian line shape as noise up to the relaxation oscillation [175] is dominated by amplitude noise. The time-bandwidth product is obtained by taking the 3 dB optical and hence 6 dB rf-bandwidth of 50 kHz and the upper-state lifetime of 4 µs, leading to roughly 0.2, close to a Lorentzian shape.

The NPR oscillator shows strong correlation of amplitude and phase up to the bandwidth of the feedback loop at 10 kHz of the timing jitter stabilization, which actually coincides with the peak of the Kendall-τ_b correlation analysis. Hence, this strong correlation could be simply a feedback loop artifact or originating from optical phase noise and is not necessarily carrier-envelope phase noise. Nevertheless, the nonlinear times series suggests rather stochastic noise in this frequency region.

The NALM-based Er:doped fiber laser shows mainly white noise in amplitude and phase, which is confirmed by the nonlinear time series analysis. Furthermore, no correlation of both, amplitude and frequency noise can be seen in the time-resolved Kendall analysis. Together, this indicates operation at the fundamental limit of amplified spontaneous emission. Another possible source of this trend could be additional white noise from the measurement process itself, namely shot noise. Nevertheless, this is rather unlikely as the strong beat note of roughly 48 dB implies high photon numbers during measurement.

The second Er:doped fiber laser, which is mode-locked by a SESAM, provides an exceptionally broad beat note of 1200 kHz at 6 dB rf-bandwidth. In combination with the spectral densities and the nonlinear time series result this clearly indicates a broad white noise origin. While the reason for this strong white noise could also be due to detection-induced shot noise, however, the unexpected 5 % broadband correlation seen between amplitude and frequency well beyond the possible laser bandwidth above about 1 ms in the Kendall-τ_b analysis strongly supports the assumption of a coupling mechanism that connects amplitude and frequency variations. As no traces of determinism and correlation above the laser response bandwidth should be expected, this coupling mechanism could be originating from the mode-locking mechanism itself, hence the SESAM. This is further investigated in the next part.

Overall, despite the limited number of analyzed lasers, essentially the mode-locking mechanism seems to be of higher importances compared to the actual gain medium. This is supported by the difference seen in the mode-locked Er:doped fiber lasers, where two severely differing broad beat notes have been observed.

2.3.6 Broadband Coupling Mechanism in the SESAM-based Oscillator

The observed broadband correlation between amplitude and frequency CEP noise in the SESAM-based Er:doped fiber laser can be explained by a conversion of ASE energy fluctuations into CEP fluctuations. In laser diodes, a similar coupling has been seen between the junction voltage and intensity fluctuations [176, 177], where the origin of this coupling has been attributed to the dipole interaction between the

internal field and electron-hole pairs.

To further verify the hypothesis of a broadband coupling mechanism that introduces additional CE phase noise well beyond the response time of the gain medium, the potential origin is investigated. One of the fastest intra-cavity responses is provided by the saturable absorber mirror (SESAM) that enables transient cavity loss control and thus the stabilization and initialization of femtosecond long pulses. In this way, the SESAM effectively provides saturation of the self-amplitude modulation and thereby allows the opening of a net gain window, which is required for the pulse formation. This fast interaction between pulse and SESAM can lead to a complicated temporal response of the pulse and thereby result in negative side-effects. One such effect is occurring when the SESAM is operated at or in the close proximity to a narrow excitonic resonance line, where the exciton's create an additional peak in the absorption spectrum within the band gap. Then, the related absorption dynamics and changes in refractive index may introduce additional CEP jitter.

When a SESAM is operated at a narrow excitonic resonance, the absorption change $\Delta\alpha$ can be strongly enhanced and couples via the Kramers-Kronig relation to a phase change $\Delta\varphi$ via

$$\Delta\varphi(\omega) = \frac{\omega}{\pi}\int_0^\infty \frac{\Delta\alpha(\omega')}{\omega'^2-\omega^2}\mathrm{d}\omega'. \tag{2.21}$$

This phase change results in a steep spectral dispersion slope at the excitonic resonance that induces a CEP change by

$$\Delta\varphi_{\mathrm{CE}}(\omega) = \omega\frac{\partial\Delta\varphi(\omega)}{\partial\omega}. \tag{2.22}$$

In order to reproduce such a response of the SESAM, an ensemble of pulses that form a pulse train is simulated. A Poissonian distribution of photon numbers within each pulse is assumed. Each pulse consists of $\langle E_P\rangle = 10\,\mathrm{pJ}$ energy and respective $\langle N\rangle = 8\times10^7$ photons, which corresponds to common scenarios in fiber lasers. The resulting absorption change is then calculated by using [178]

$$A = 1+\frac{F_{\mathrm{sat}}}{F}\log\left(1+(1-\Delta R)\left(\exp\left(\frac{F}{F_{\mathrm{sat}}}\right)-1\right)\right), \tag{2.23}$$

where F_{sat} is the saturation fluence, F the fluence and ΔR the modulation depth. In the above equation, non-saturable losses are neglected. Choosing $\Delta R = 30\%$, and an average fluence of $F = 3F_{\mathrm{sat}}$, the resulting absorption change is $\Delta\alpha = 1.1\times10^{-5}$, within the range of values found at an excitonic resonance line [179]. The resulting absorption change at a resonance centered at 1560 nm is shown in Fig. 2.10. Hence, an absorption change $\Delta\alpha = 1.1\times10^{-5}$ results in a phase change via Kramers-Kronig of $\Delta\varphi(\omega) \geq 20\,\mu\mathrm{rad}$. The strong dispersive slope induces via 2.22 a carrier-envelope phase change $\Delta\varphi_{\mathrm{CE}}(\omega) = -10\,\mathrm{mrad}$. Since the relaxation time of common SESAMs is readily within the picosecond range, a broadband coupling mechanism well beyond the gain mediums response time is possible as was seen in the experiments for Er:doped fiber laser A. This can be estimated to induce a broadening of the beat note by 200 kHz at 100 MHz repetition rate. Therefore, operation of a SESAM under certain conditions within a fiber laser may readily introduce additional broadband CEP noise in the presence of intra-cavity pulse energy fluctuations [180]. As this also interferes with the carrier-envelope offset frequency, it renders SESAM-based oscillators only partially suitable for frequency comb applications.

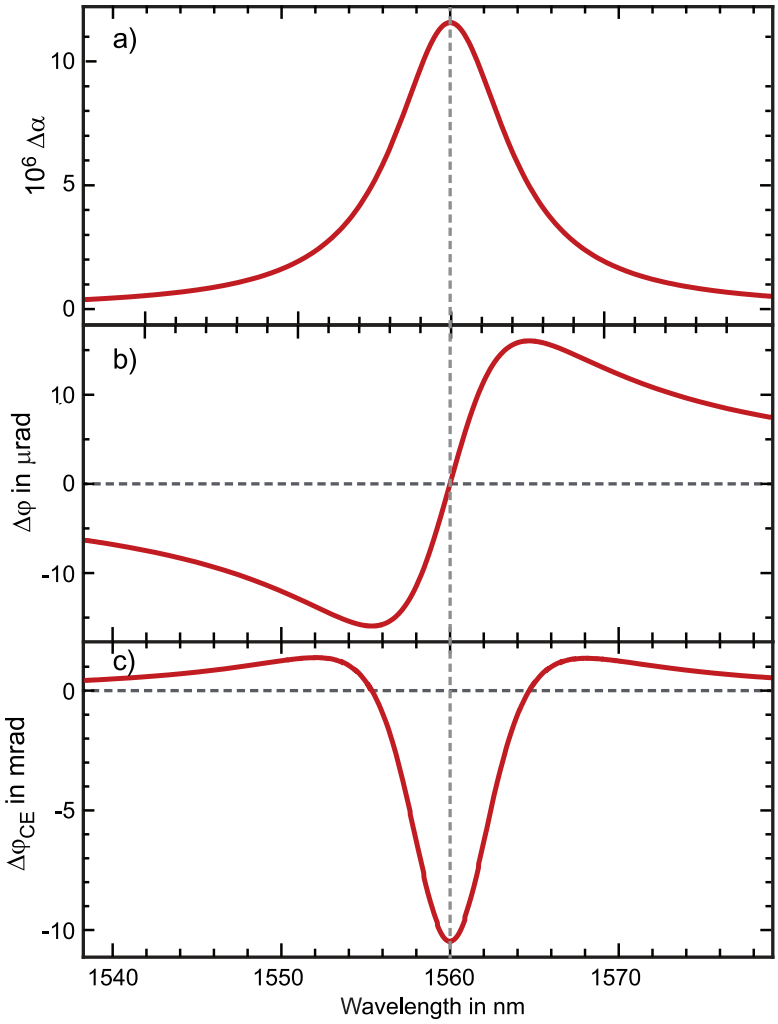

Figure 2.10: Simulation of the Kramers-Kronig relation that connects the absorption change to the phase change within the SESAM. a) Assumed absorption change $\Delta\alpha$ at an excitonic resonance, b) resulting phase change $\Delta\varphi$, and c) associated carrier-envelope phase change $\Delta\varphi_{CE}$.

2.4 Concluding Remarks

Inherent CEP noise properties of different laser oscillators were systematically investigated with conventional and novel tools. To this end, the free-running CEP obtained from three different fiber lasers and one Ti:sapphire laser were employed. While the novel tools, namely the time-resolved Kendall-τ_b correlation analysis and time-resolved nonlinear time series analysis were employed to investigate correlations between amplitude and frequency and the statistical nature of the noise, respectively, in combination with the power spectral densities of amplitude and frequency several conclusions can be made. First, the residual CEP jitter seems to depend on the employed mode-locking mechanism, as can be seen in the varying performance of the two Er:doped fiber lasers. While the SESAM within one Er:doped fiber laser can be suspected to introduce a coupling of intra-cavity power fluctuations to CEP noise well beyond the response bandwidth of the laser, the second Er:doped laser showed no correlation over the whole analyzed region at all. Hence, this suggests that avoiding SESAMs when it comes to optical frequency combs might be beneficial for the overall comb stability. To the contrary, the NPR-based system and Ti:sapphire-based laser both show a strong correlation around 1 ms rolling off to faster time scales. While the statistical noise analysis indicates white noise present in this frequency range, the frequency noise densities and amplitude spectral densities show isolated peaks in this region that might connect both amplitude and phase fluctuations to a technical source. Interestingly, for the NPR laser, the strong amplitude-to-frequency noise correlation seen in the Kendall-τ_b analysis peaks with the bandwidth of the repetition rate lock of both lasers. Essentially, in all lasers strong white noise signatures are observed. Especially in the Ti:sapphire and NALM laser, little indications for intra-cavity coupling mechanisms beyond the laser response time is seen.

To conclude, the results of the nonlinear time series analysis as well as the frequency spectrum indicate a different origin of the noise. It can be suspected that rather constraints during measurement may affect the performance. This is investigated in the next part with an emphasis on the CEP detection of amplified pulses, where strong white noise sources typically dominate. Overall, in order to gain a deeper understanding of CEP noise characteristics and their dependencies on the mode-locking mechanism and gain medium, presented novel tools need to be applied to a broader range of systems to allow further conclusions.

Chapter 3

Fundamental Limitations in Amplifier CEP Detection

In the previous chapter, CEP noise sources within various oscillators have been analyzed in order to understand why some lasers are readily CEP stabilized and others have been found to show severe fluctuations rendering stabilization troublesome. While continuous progress has been made in minimizing residual jitters to only 8 attoseconds (20 mrad) in oscillators [12], most experiments involving highly nonlinear interaction, such as the generation of (isolated) attosecond pulses employing HHG [5, 18, 91, 181], require high peak powers. To this end, chirped-pulse amplification is typically used to amplify the pulses. While being amplified, the pulse is exposed to noise of technical and environmental nature. Furthermore, fundamental limitations such as quantum mechanical effects act upon the CEP during, e.g., the amplification process itself [5]. Technical noise sources are introduced by beam pointing variations in stretcher and compressor [32, 133], pulse picking jitters [135] or pump feedback loops as has been discussed earlier. Comparable CEP stability to oscillators has not been achieved to date as residual jitters of around 150 to 200 mrad are typically obtained on a single-shot basis [16, 18, 19, 123]. In fact, it is quite common during measurement of the CEP of amplifiers to average over multiple laser pulses. This is required due to weak intensities at the back-end of the detection scheme. Then, averaging leads to an effective underestimation of the actual residual CEP jitter. Furthermore, these low photon numbers lead to an increased impact of electronic noise, which can additionally spoil the measurement. However, identifying and reducing potential noise sources requires precise single-shot CEP detection, which then enables meaningful interpretation of the power spectral density up to half of the repetition rate. First approaches in this direction with a common spectral interferometry setup revealed strong single-shot jitters above one radian [182]. Further steps to optimize single-shot CEP measurements and to expose additional noise features in the power spectral density were undertaken by Koke et al. [16], who developed and employed the measurement scheme named fast f-$2f$ interferometry. Single-shot results showed CEP fluctuations that substantially exceeded 0.5 rad [16], while the noise floor in the phase noise density was clearly dominated by white noise that was identified to originate from shot noise during detection. Therefore, it can be argued that shot noise hinders further minimization below the measured shot-to-shot 210 mrad residual CEP jitter. Additionally, a reduction of shot noise may uncover further noise sources that could be subsequently removed.

In this chapter limitations during detection of the CEP are addressed. Shot noise, as a fundamen-

tal limit, is further discussed in detail, while measures to minimize its extent are introduced. Then, the shot noise-inflicted CEP jitter is estimated, with subsequent stabilization of the CEP. Finally, further limitations introduced by the supercontinuum (SC) process are discussed where potential coherence degradation during filamentation is analyzed in the context of introducing additional uncertainty during the measurement of the CEP.

3.1 Limitations of Amplifier CEP Detection

CEP detection of amplified pulses has been carried out in various ways [16, 95, 102, 106] as has been described in section 1.4.1. Here, the discussion is focused on spectral interferometry-based CEP detection and its further developments. In these measurement schemes, the spectral extension is subsequently followed by frequency-doubling, both typically organized in a common-path arrangement. Within the detection scheme, additional noise can be added to the actual CEP jitter in manifold ways, with large contributions stemming from the interferometer design, the fringe contrast or resolution in the spectrometer, and possible latencies imposed by the CEP control due to limited bandwidth. These technical contributions are supplemented by fundamental constraints such as shot noise during detection.

This chapter is focused on minimizing the fundamental uncertainty during detection, which is said to be mainly caused by shot noise. Shot noise was identified by Koke et al. [16, 118] as the major limiting constraint due to the dominating white noise floor seen in the phase noise density of their measurement. Despite pulse energies in the order of 1 mJ, translating into roughly 10^{16} photons at 800 nm that are readily available from amplifiers, the critical power during supercontinuum generation (SCG) limits the participating photons before multi-filamentary break-up to about 10^{13} and 10^{11} at 800 nm in the case of gases and solids, respectively [119]. Furthermore, a reduction by two to three orders of magnitude found in the spectral region of interest at the edges of the SC is present. Combined with second-harmonic generation, this results in the formation of interference fringes that consist on average of only $\langle N \rangle \approx 10^4$-$10^7$ photons per pulse for solids and 10^6-10^9 for gases. In their experiment, Koke et al. estimated the residual photon numbers to be roughly 32.000 that form a single interference fringe in a fast f-$2f$ arrangement. This indicates a strong limitation due to shot noise when sapphire is used as a SCG medium. Additionally, at those low photon numbers, averaging over multiple shots m can be necessary in some situations. The shot noise effect during CEP read-out is numerically estimated in the next part.

3.1.1 Numerical Simulation of Shot Noise in Amplifier CEP Detection

With shot noise corresponding to the fundamental limit of resolution of the CEP when neglecting detector noise, it is well worth to analyze its effect on CEP stability.

Following the approach presented earlier by Borchers et al. for oscillators [24], each pulse of the noisy pulse train $N(k)$ from equation 1.67 corresponds to counts detected by one pixel of a pixel-based detector with L elements at the output plane of the spectrometer as it is sketched in Fig. 3.1 a). Here, a perfect fringe contrast with 100 % modulation depth is assumed that corresponds to balanced photon numbers within the second harmonic and fundamental region. Shot noise is introduced by adding Poissonian noise with spread $\sqrt{N(k)}$. The position of the fringe is extracted by FFT-based algorithms, or if the fringe period is known, via a method similar to lock-in detection where the phase of the Fourier component is readily accessible. Employing the latter approach, the Poissonian noise-covered oscillation

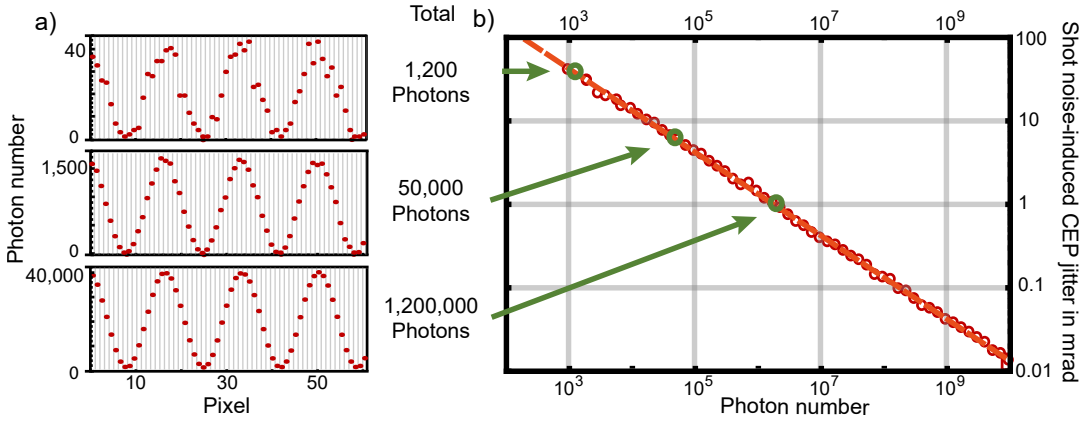

Figure 3.1: a) Numerically simulated fringe pattern $N(k)$ with Poissonian noise spread $\sqrt{N}$ that includes shot noise. Three different scenarios with a total number of photons N_{tot} are given. b) Simulated shot noise-induced CEP jitter in mrad for the case of spectral interferometry based on a CCD detector following Borchers et al. [24]. Here, unbalanced photon numbers as well as electrical contributions are excluded.

$N(k)$ is numerically mixed with a reference signal and subsequent integration over the fringe pattern is carried out for a sinusoid and cosine with spatial fringe frequency f_k, which leads to

$$X = \sum_k N(k)\cos(2\pi f_k k) \;\wedge\; Y = \sum_k N(k)\sin(2\pi f_k k)\,, \tag{3.1}$$

where the CEP of the fringe pattern φ_F is then available by the angle $\varphi_F = \tan^{-1}(Y/X)$. This detection method only provides access to the phase slippage from shot-to-shot, not the absolute phase. While simulations show that the number of pixels L has no impact on the CEP jitter, the total number of detected photons $N_{\mathrm{tot}} = \langle N\rangle \cdot L$ defines the shot noise-induced CEP jitter. Any averaging over multiple shots m can then be interpreted as a simple accumulation of photons and thereby effectively reduces the shot noise-induced CEP jitter by a factor of $\sqrt{m}$ [183]. This is only the case for a Gaussian noise distribution, while in experimental conditions, technical noise might deem the noise characteristics differently. The result of the simulation is shown in Figure 3.1 b), where the orange line indicates the found $1/\sqrt{N_{\mathrm{tot}}}$ scaling of the noise floor. Hence, a four orders of magnitude increase of photons results in a two order of magnitude reduction of the shot noise-induced CEP jitter. Borchers [119] additionally included technical noise sources such as electrical noise due to the dark current present in any semiconductor junction and additional read-out noise of the CCD caused by thermal noise. With a realistic read-out noise figure of about 30 electrons per pixel and frame, a severe contribution for photon numbers around and below 10^4 can be expected that leads to some tenth of mrad additional phase jitter. Above 10^5 photons the impact becomes increasingly negligible. Therefore, at low photon numbers, electric contributions may cause additional uncertainty, especially in the case of CCD detectors. Nevertheless, in photomultiplier tubes these technical contributions are largely minimized.

Overall, this numerical analysis clearly emphasizes the need for increasing photon numbers at the back-end of the detection scheme in order to minimize shot noise and potential electrical contributions to the shot-to-shot detection uncertainty.

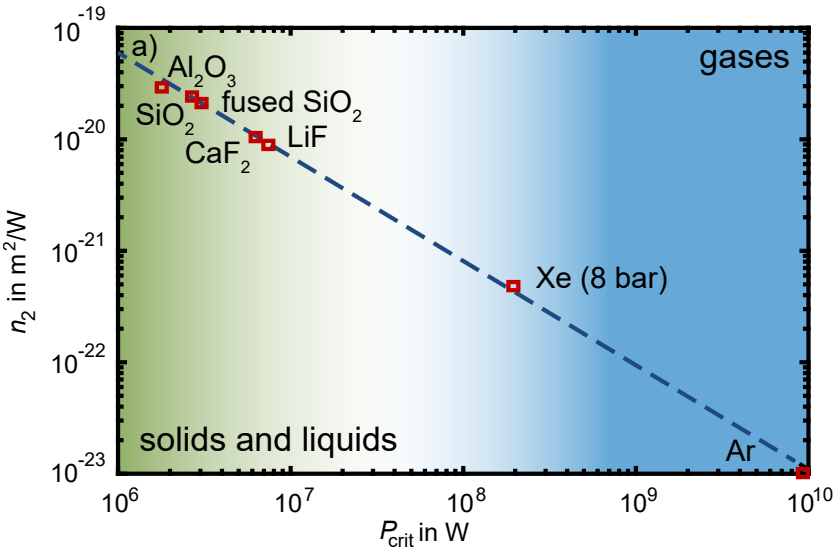

Figure 3.2: Nonlinear refractive index n_2 as a function of the respective critical power P_{crit}. While solids and liquids only allow limited incident powers up to several MW, gaseous media enable high peak power filamentation in the GW regime. In between those three phases of matter, a huge gap exists that can be filled with gaseous media at increased pressures such as xenon at 8 bar.

3.2 Reducing Shot Noise in Fast f-$2f$ Interferometry

In the previous section numerical investigations have shown that low photon numbers lead to strong contributions of shot and electric noise that can be responsible for part of the measurement-induced CEP uncertainty. Here, the influence of shot noise on the CEP detection is further experimentally verified and minimized to a negligible extent.

3.2.1 Identifying Potential Measures Against Shot Noise

The shot noise-inflicted CEP jitter can strongly influence the detection process and thereby decrease the resolution of the fringes. In order to avoid this uncertainty, the two nonlinear processes involved in f-$2f$ interferometry need to be optimized. While this includes the use of second harmonic crystals with an increased effective second-order nonlinear optical coefficient d_{eff} to maximize the frequency-doubled photons, new ways of generating the octave-spanning spectrum need to be considered in order to increase photon numbers at both edges of the extended spectrum, too. The latter can be realized by increasing the critical power limit P_{crit} relative to the commonly employed sapphire. Then, the spectral density is increased over the whole octave-spanning spectrum, which, in combination with an optimized second harmonic leads to a minimization of shot noise. Since the critical power follows $P_{\mathrm{crit}} \propto {}^{\lambda^2}/_{n_0 n_2}$, lowering the nonlinear and linear refractive index at constant wavelength enables to maximize the critical power and hence the possible fluence at either edge of the SC [24, 52]. The relationship of n_2 and P_{crit} is shown for various materials in Fig. 3.2.

While gases allow a critical power of several tenth of gigawatts, condensed media typically have a thousand times higher nonlinearity n_2 that limits the maximum P_{crit} to only a couple of MW [52, 184]. When the critical power is surpassed, the filament is limited by the clamping intensity I_{cl} from equation 1.25 and further spectral extension is inhibited. Increasing the incident power even further leads to modulation instability that ultimately leads to the opening of new filaments to avoid catastrophic

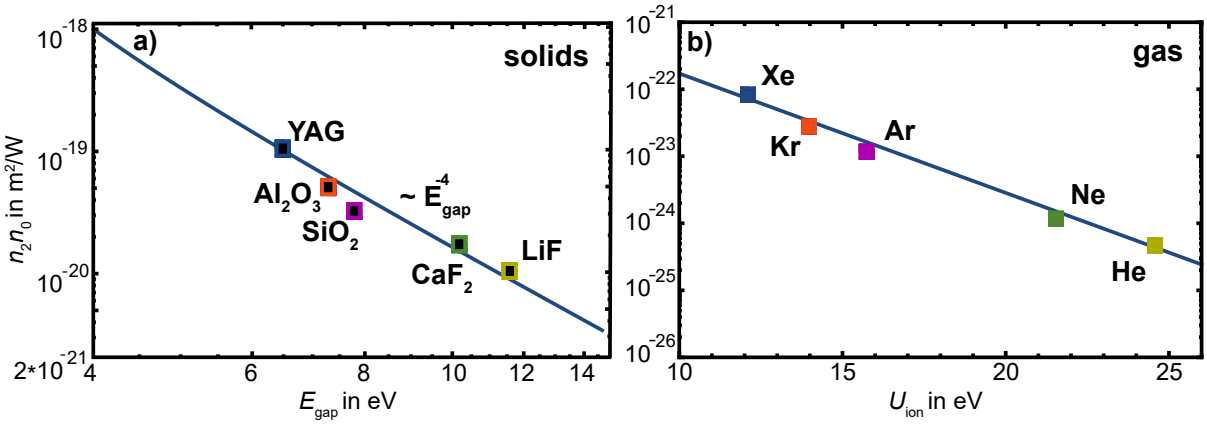

Figure 3.3: Product of nonlinear and linear refractive index n_2 and n_0, respectively, as a function of the respective band gap E_{gap} in a) or as a function of the ionization potential U_{ion} in b). In the former the expected E_{gap}^{-4} dependence can be seen.

damage, also referred to as multi-filamentation. As each filament accumulates its own nonlinear phase, an interference pattern emerges that renders the SCG unsuitable for further application in terms of CEP detection. Therefore, within this thesis, only single filaments are considered.

Brodeur et al. [51] showed that the nonlinear refractive index n_2 relates to the band gap E_{gap} of the medium and thereby determines its SCG properties, too. As can be seen in Fig. 3.3 a) for solids, the nonlinear refractive index decreases with increasing band gap, i.e., with $n_2 \propto {}^{E_{\text{gap}}^{-4}}/_{n_0}$. A similar picture emerges when plotting $n_0 n_2$ against the ionization potential of gases as shown in Fig. 3.3 b). This relationship has consequences for the supercontinuum process, too. For example, the spectral extent to the anti-Stokes side and additionally, the onset of filamentation shows a clear correlation to the mediums band gap E_{gap} [51]. For pulses with a central wavelength of 800 nm, a minimum band gap of $E_{\text{gap}}^{th} \approx 4.7$ eV is required. As this corresponds to three-photon ionization, the filamentation threshold can be explained by the need to balance $n_2 I$ by plasma generation that is typically achieved by multi-photon ionization for ultra-short pulses. At small band gaps below E_{gap}^{th}, the rate at which electrons are freed by either one or two photon absorption is high and reaches quickly the needed 10^{18} cm^{-3} electrons to cancel self-focusing, inhibiting the formation of a filament. In this case, no spectral extension is seen as the formation of an optical shock is inhibited due to the early onset of plasma generation. Furthermore, the spectral extension dependence on the band gap is actually contradicting the expected increase of the anti-Stokes extension with increasing n_2 from pure SPM theory presented in Eqn. 1.27. This may also be explained by considering the process of optical shock formation, i.e., self-focusing and its opponent plasma generation. With increasing band gap the plasma generation is delayed, which leads to increased propagation prior defocussing takes place. This results in an enlarged phase jump at the pulse peak, which then leads to an extension of the supercontinuum towards short wavelengths. The previous discussion of physical limitations seen experimentally is not only limited to solids. Gases and liquids have been employed as SC media, too, where similar physical constraints are seen. However, mostly solids have been observed to feature broad and smooth spectral densities as well as high stability [185, 186]. Their application within amplifier CEP stabilization schemes is therefore straight-forward.

After emphasizing the importance of physical limitations and relations to the band gap of the medium,

Source	E_{gap}/E_I (eV)	n_0	n_2 (10^{-20}m^2/W)	P_{crit} (10^6 W)	κ (300 K) (W/mK)
Al_2O_3	9.9	1.8	3.1	1.8	46
Fused silica	9	1.45	2.4	2	1.4
BaF_2	9.1	1.47	1.91	3.3	12
YAG	6.5	1.82	6.2	1.8	13.4
MgF_2	10.8	1.38	0.67 (532 nm)	19	21-30
CaF_2	10	1.43	1.05	6.2	9.7
LiF	13.6	1.39	0.81	7.5	14
β-BBO	6.2	1.66	5.2	1.1	1.2
Xe (1 bar)	12.12	≈ 1	0.0055	1750	0.00548
Xe (8 bar)	12.12	≈ 1	0.044	220	0.0058
Ar (1 bar)	15.76	≈ 1	0.001	9600	0.0179
l-N_2	15.58	≈ 1	0.0021	4500	<0.0094 (<100 K)
H_2O	6.9	1.33	5.7	1.2	$\sim$0.6

Table 3.1: Properties of various sources, including the band gap or the ionization energy, n_0 and n_2 at 800 nm central wavelength if not otherwise stated, the critical power P_{crit} and thermal conductivity κ. [24, 40, 52, 187, 188, 189, 190, 191, 192, 193]

the optimum choice for increasing P_{crit} and hence maximization of spectral densities over the whole octave can be discussed. Fluorides, in particular LiF and CaF_2 are media with the largest band gap found among solids and are therefore prime candidates for high-fluence SCG. However, as strong powers are required damages and thermal effects can play a role and hence, a high thermal conductivity is additionally needed. This limits the application of fluorides since they only have a third or quarter of the thermal conductivity provided by sapphire. The latter, Al_2O_3 exhibits a low n_2 and a high thermal conductivity, which renders it an optimal choice. Table 3.1 provides an overview of possible materials and their properties for seeded spectral extension of at least one octave initiated from 800 nm. While YAG has also been employed, its twofold nonlinearity compared to sapphire reduces its spectral extension into the UV. Additionally, a lower thermal conductivity may introduce further drawbacks. Gases are also of interest despite potential limitations caused by strong pulse-to-pulse fluctuations. As can be seen in Fig. 3.2 a big gap between solids and gaseous media exists when moving from lower to higher critical powers. That gap can be bridged by increasing the pressure of the gas. This is enabled by the fact that the linear and nonlinear refractive index scale with the density, which results in a critical power increase with increasing pressure [194, 195]. To this end, suitable critical powers can be obtained that lie in between the mega- and gigawatt range. Besides the spectral extent and strength of the generated SC, also shot-to-shot stability, coherence and polarization preservation are important aspects to consider when choosing a SC medium. These properties have been especially well maintained in solids.

Before looking into potential new sources with previously discussed properties, a literature overview on used supercontinuum sources in the context of CEP measurement and stabilization is given.

3.2.2 Supercontinuum Generation in the Context of CEP Detection

Supercontinuum generation within CEP detection schemes has been carried out in various media, including sophisticated wave-guiding structures such as photonic crystal fibers where enhanced modal confinement leads to increased nonlinearity and additionally allows an improved tuning of the SC properties [196, 197]. These fibers are easily damaged by high input powers and are therefore restricted to the

use for oscillator pulses as a means of effective spectral broadening under low light conditions [198]. In this regard, they have been used within the first f-2f interferometer schemes [110] and after optimization have enabled sub-10 as timing jitter stabilities of the CEP [12].

However, for low-repetition rate high peak power amplifiers, fibers with a greater core size have to be used in order to avoid damage. For the first implementation of spectral interferometry, a 70 cm long, 530 µm inner-diameter fused silica hollow-core fiber in a krypton gas filled cell at 3.5 bar was employed [95]. With 1 mJ and 65 fs long pulses, a spectrum ranging from 400 nm up to above 1000 nm was seen and used to stabilize the amplifier [95, 199]. An earlier approach by Mehendale et al. [102] where a similar hollow fiber was employed resulted in a spectrum that extended to about 200 nm FWHM width and subsequently, the second and third harmonic was generated by frequency-doubling in a 10 µm thick BBO and by near surface harmonic generation from Si(001). Despite of the early success of hollow fibers, the focus has shifted to bulk media due to their relatively high damage threshold, stable spectral density and polarization properties. Within spectral interferometry, the most commonly employed crystal nowadays is sapphire, which constitutes the reference in this analysis. First employed by Baltuska et al. [5], sapphire conveniently introduces additional group delay between either edge of the SC, which enables proper resolution of the fringes. In the context of CEP stabilization of OPCPA systems various crystals for SCG have been used to allow the generation of the signal and the pump from the same source, while obtaining a constant CEP within the idler as a result of difference-frequency generation in a $\chi^{(2)}$ crystal. In this regard, YAG, CaF_2 and BaF_2 [200] have been employed, the latter two typically in a moving arrangement. In general, these schemes require no octave-spanning spectrum, which makes a comparison with spectral interferometry only partly meaningful. Therefore, employed sources for SCG are as of now limited and new approaches need to be explored for the particular requirements of the employed Ti:sapphire-based CPA laser system in this thesis, which is introduced in the upcoming section.

3.2.3 Experimental Conditions

A Ti:sapphire-based oscillator is used as the front-end of the CPA scheme that delivers 10 fs short pulses at an repetition rate of 84.4 MHz with an average power of 510 mW. About two-thirds of this power are further used for subsequent amplification. The measurement of the oscillator CEP utilizes roughly 150 mW in a quasi-common path f-2f arrangement, which enables octave-spanning spectrum generation in a 1 cm long PCF. Subsequent second-harmonic generation in a PPLN renders the measurement process highly efficient, allowing signal-to-noise ratios of up to 60 dB [119].

At these strong beat notes, shot noise-induced CEP jitters are small according to previously presented numerical simulations in 1.5.3. The heterodyning of both, the second harmonic and fundamental on a photodiode results in an amplitude modulation that is further locked to a quarter of the repetition rate (21.1 MHz) within the locking electronics (Menlo Systems XPS 800). The electronics consist of a frequency divider, phase detector and a PID controller that enable the generation of an error signal. Subsequently, the error signal is used to control the acoustic wave within an AOM. Hence, the pump passing through the AOM is modulated in intensity, which leads to control over the power inside the Ti:sapphire crystal. This adjusts, among other processes, the intra-cavity dispersion. The feedback approach with roughly 100 kHz bandwidth achieves a measured CEP stability of below 100 mrad, while best reported values reach even down to 70 mrad [12].

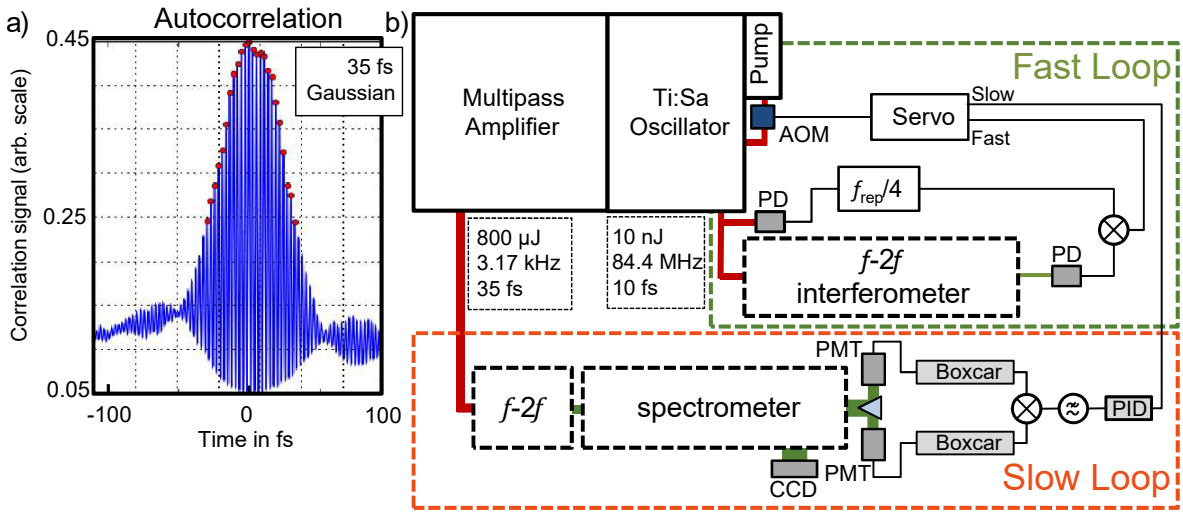

Figure 3.4: a) Interferometric autocorrelation of an optimized pulse. The measurement has been averaged over 5 shots and has been evaluated under the assumption of a Gaussian profile. A pulse duration of 35 fs is measured. Slight asymmetric measurement is caused by clipping and alignment mismatch. b) shows the electronic and optical laser setup. The Fast loop and the slow loop are shown with abbreviations of the acousto-optical modulator (AOM), the photo diode (PD), the proportional-integral-derivative controller (PID), the photomultiplier tubes (PMT) as well as the CCD detector.

The beam to be amplified is extensively stretched in a bulk stretcher. Additional chirp control is enabled by propagation through an acousto-optic programmable dispersive filter (AOPDF). The timing of the AOPDF is optimized to reduce additional timing jitter to below 100 ps. Transients are further amplified by the first four stages of a multi-pass amplifier prior to pulse picking in a conventional Pockels cell. At this point, the final repetition rate of the amplifier is set to 3168 Hz. When stabilizing the CEP, e.g., to a quarter of the oscillators repetition rate, the pulses need to be selected by the Pockels cell such that they are separated by a multiple of four to ensure the removal of the linear evolution from pulse-to-pulse. After amplification of the pulse during propagation through the Ti:sapphire gain medium for another five times, the pulse is subsequently compressed in a bulk prism compressor. This enables pulses of 800 µJ with 35 fs duration, which was measured using interferometric autocorrelation as is shown in Figure 3.4 a).

While the fast loop stabilizes the CEP of the oscillator, slow drifts caused by, e.g., environmental disturbances such as air pressure changes, humidity and temperature fluctuations that occur within the amplifier need to be additionally compensated. To this end, fast f-2f interferometry is carried out, while the details of the detection schemes in terms of SC media and SH are discussed in section 3.2.6. Hence, after supercontinuum generation and frequency-doubling, one fringe is selected at the back-end of a spectrometer and split in half upon incident on a metallic prism front edge. Subsequently, each half is detected by a photomultiplier tube (PMT), which enables efficiencies of up to 30 % in the bluish region. Each PMT signal is isolated using a triggered Boxcar and subsequently mixed. Low-pass filtering and appropriate amplification in a PID renders the error signal suitable for offsetting the oscillators CEP error in the servo unit (Menlo Box). In this manner, results were presented by Koke et al. that achieved a residual CEP jitter of 210 mrad on a single-shot basis [16].

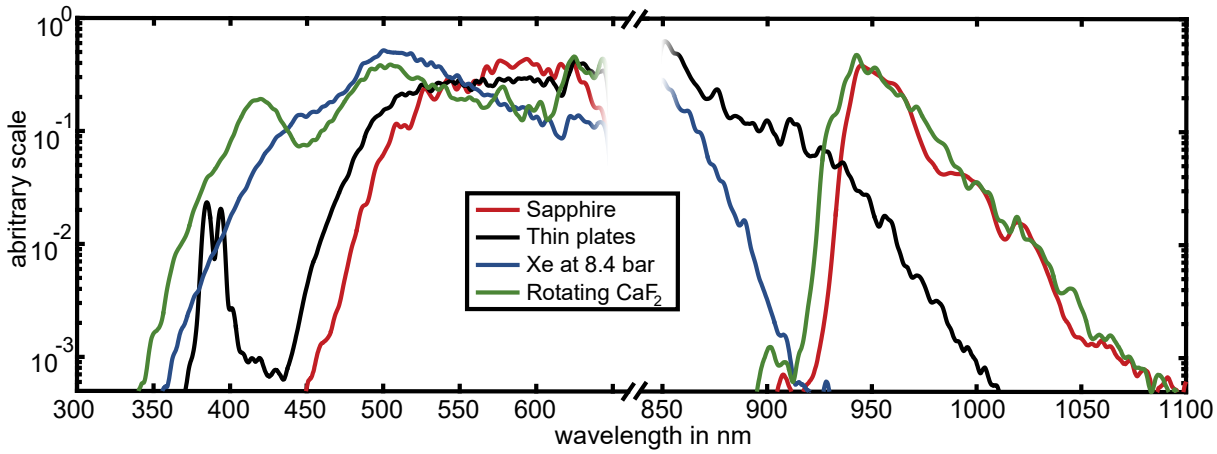

Figure 3.5: Measured spectra of employed supercontinuum sources. While sapphire and CaF_2 show a deep extension into the IR, the continuum generated by xenon and the thin plates arrangement only reaches down to about 900 nm and 1000 nm, respectively. On the anti-Stokes side, while sapphire reaches only down to 450 nm, calcium fluoride shows promising extension far deeper into the UV below 350 nm. Xenon and the thin plate arrangement reach down to 360 nm as well as 450 nm, respectively, while the latter shows surface SH generation of the seed at around 400 nm.

3.2.4 Employed Supercontinuum Sources

After motivating the need and approaches to minimize shot noise influence during detection to a negligible extent, four different supercontinuum sources are selected. These, with exception of the reference sapphire and most certainly CaF_2, have to the best of the authors knowledge not been employed in the context of CEP detection in spectral interferometry. While LiF would be the perfect candidate with the highest possible critical power, the formation of color centers typically renders the generated continuum unstable. Despite recent results [201] that indicate possible long-term operation, SC from LiF was not observed to be stable under the conditions present in this work. Within minutes, the SC flickered and vanished. Additionally, similar trends were observed for MgF_2 and BaF_2. However, CaF_2 under translating or rotating conditions has been seen to be a suitable sources for spectral extension, which is further explained in the discussion later on. Another approach to SCG in solids was recently introduced by Lu et al. [202], where thin silica plates are cascadedly arranged such that the beam can recover between sessions of highly nonlinear interaction, and thereby enables a thousandfold increase in the ratio of incident to critical power. This source has also been employed and is elucidated below. As has been discussed earlier, gaseous media offer a two to three orders of magnitude lower nonlinearity compared to solids with respective higher critical powers. To this end, noble gases are best suited. Within this work argon and xenon at several atmospheres have been tried. Whereas for argon, no stable conditions for the resulting conical emission were found in the presented arrangement, xenon at several bar pressure led to a brightly shining conical emission, which was observed visually.

Sapphire

Sapphire (Al_2O_3), with its high thermal conductivity and damage threshold, has found widespread applications as a supercontinuum source for seeding optical parametric amplifiers [20, 203], within pump SC probe experiments [204, 205, 206] and in spectral interferometry for measuring the CEP. Sapphire is commonly employed in the latter case in most products and therefore constitutes the reference SCG

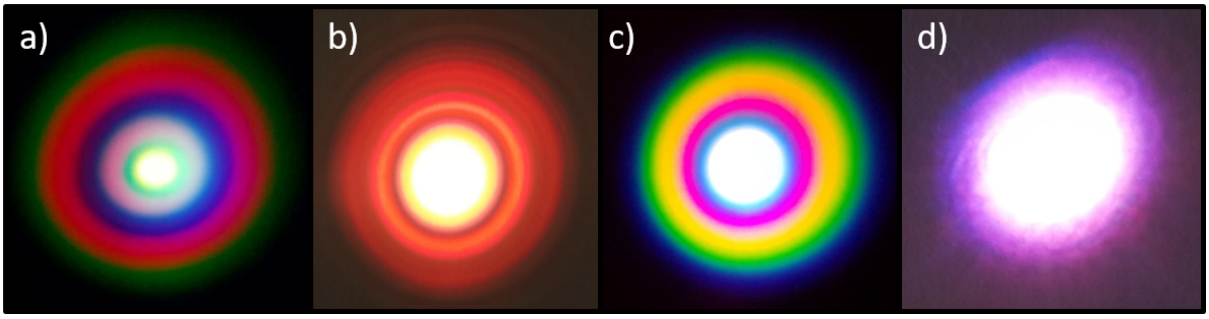

Figure 3.6: Far-field pictures taken from conical emission of chosen white-light sources. a) 2 mm thick sapphire, b) Arrangement of two 50 µm quartz and seven 100 µm thick fused silica plates, c) Rotating 2 mm thick CaF_2 and d), xenon at 8 bar. Here, the divergence of the latter is much smaller compared to the other three sources. Interestingly, the conical emission of a) and c) show opposing wavelength-dependent divergence.

source in the presented analysis. While most experiments involve rather short focal lengths below 50 mm [185, 187], here 100 mm is found to achieve better control over the SC with increased stability and the strongest observed spectral density. As can be seen in Figure 3.5, the spectrum reaches well below 470 nm in the UV and above 1050 nm in the IR with about 1 µJ input energies. Table 3.1 includes relevant properties of the SCG sources that are employed within this study.

Calcium Fluoride

With its band gap of close to 10 eV, calcium fluoride seems to be very suitable for broadband SCG. However, as with most fluorides, pulses with high peak powers induce irreversible optical damage to the crystal. To circumvent this, constant rotation or linear motion is required. Besides damage, the generation of color centers can lead to strong fluctuations of the SC [207]. While linear movement of CaF_2 has been found to depolarize the generated continuum around the pump wavelength and may result in elliptical light at the edges of the continuum [208], this work further focuses on the rotation of a CaF_2 plate. Together with a linearly polarized pump, polarization-dependent threshold energies for SCG have been found before [209] and observed here. Furthermore, depolarization of the SC caused by nonlinear anisotropic birefringence (NAB) [210] as well as intensity fluctuations depending on the crystal and pump polarization orientation have been seen. In the context of measuring the CEP, albeit assuming perfect coherence, polarization dynamics would drastically deteriorate the visibility of the resulting CEP fringes if they are present at all. Johnson et al. [209] have shown that a circularly polarized light beam together with a rotating [001]-cut 2 mm thick calcium fluoride plate can lead to a stable and constant SC without any long-term degradation of the material. Furthermore, the polarization of the pump is maintained. Therefore, an increase in photon numbers due to the higher critical power is possible, which enables to increase the visibility of the CEP-related fringes. In Figure 3.7, the measured fluctuations are shown over multiple periods of rotation for a 2 mm thick [001]-cut CaF_2 plate. After the SCG, a low pass filter transmitting only wavelengths below 650 nm is used. The fluctuation is measured by focusing the light slightly behind a biased silicon photodiode, which enables to collect all photons. Here, the coefficient of variation is employed, which is the standard deviation divided by the mean. Measurements of the pump without employing a filter show a fluctuation of 2.3 %. The supercontinuum of CaF_2 features an increased variation coefficient with a linearly and circularly polarized pump that results in 11.47 % and

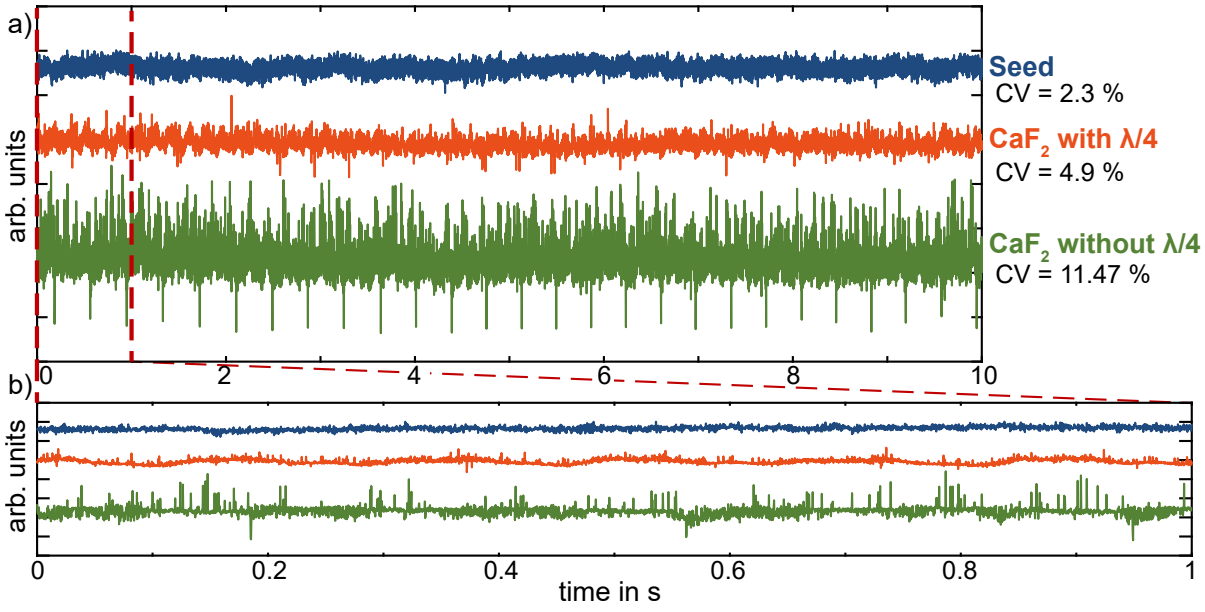

Figure 3.7: Measured fluctuation of the pump (blue), which is compared to the fluctuations of the supercontinuum obtained from CaF_2. Low-pass filtering at 650 nm is carried out. The seed was either linearly or circularly polarized and both SC were generated in a rotating plate scenario. a) Fluctuations over 10 seconds and b), one second detailed view that enables to see fluctuations with roughly 0.4 Hz periodicity at a rotation frequency of 1.6 Hz. The coefficient of variation CV is given.

4.9 % residual fluctuation over 10 s, respectively. Furthermore, the SC generated by the former clearly shows intensity modulation with the expected $\pi/2$ periodicity while rotating, which can be explained by the angular dependence of χ^3 [191, 209] and hence the varying critical power. In the presented case, the s- and p-polarized components that are fluctuating asynchronously due to birefringence have not been measured separately.

The modulation depth is quite strong but does not reach 100 % as might be expected as a result of the orientation-dependent critical power. This is caused by the generation of the SC close to the maximum clamping intensity as a result of a pulse energy of roughly 2.3 µJ. For circularly polarized light, the periodic fluctuations are almost completely suppressed, while some residual periodicity is probably caused by the limited conversion bandwidth of the employed quarter waveplate relative to the incident spectrum. Additionally, the rotational process itself is slightly varying the position of the focus. For wavelengths above 950 nm, a comparable result is found. In Figure 3.5, the spectrum for CaF_2 is shown that reaches far into the UV well below 400 nm. Additionally, on the infrared side, a spectral extension comparable to sapphire is found. Relative to the far-reaching spectral density observed into the IR, below 450 nm, an insufficient number of photons is present. Therefore, the second harmonic wavelength is chosen within the frequency range centered at 1000 nm.

Xenon

With the two orders of magnitude reduced nonlinearity of gases, they provide a reasonable choice for high-power supercontinuum generation [184, 194]. To this end, noble gases are commonly employed within a hollow-core fiber arrangement, especially in the context of pulse compression [211]. In this way, pulse compression close to the single-cycle regime [138] has been realized. Nevertheless, energy

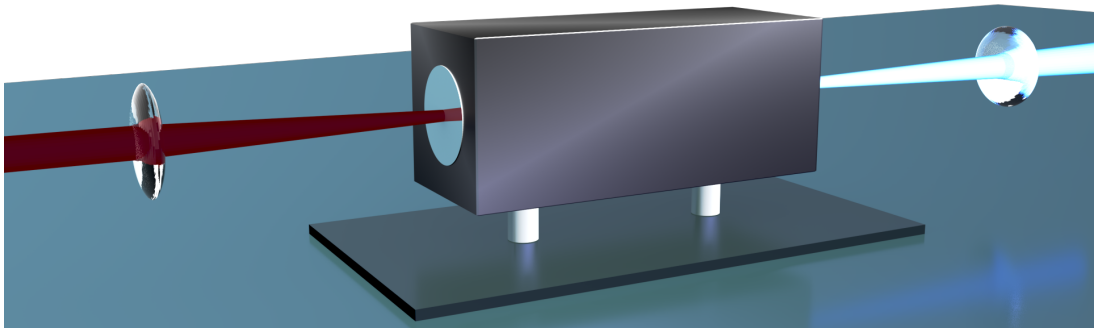

Figure 3.8: Sketch of a high-pressure gas cell used as filamentation source.

scaling seems to be an issue in these fibers due to a limited thermal conductivity. Additionally, increasing the pressure to multiple atmospheres seems troublesome. Therefore, a gas cell is better suited to enable high pressure up to 10 bar [212]. Filled with xenon due to its higher nonlinearity as compared to, e.g., argon, the gap between solids and gases in terms of critical power can be overcome (see 3.2). While argon at multiple atmospheres was also tried, no stable conical emission was found under similar conditions. Using xenon at 8 bar in a 20 cm long gas cell as is sketched in Fig. 3.8 has led to a higher spectral density over the whole supercontinuum. The generation of a stable filament in the gas drastically depends on the numerical aperture (NA) and the seed power. Three regimes are identified here: before filamentation sets in, no white light is visible. After the critical power of about 50 mW is reached for a NA of approximately 0.026, SCG by a single filament is clearly visible. Once the power is too high to sustain a single filament, multi-filamentation takes over. Due to the compactness of the gas cell and its thick windows of about 4 mm width that was necessary to withstand high pressure, only focusing with up to 20 cm focal length is possible to avoid SCG in the CaF_2 window. With the requirement of tight focusing, still a resulting SC is found as can be seen in Figure 3.6 d). Here, about 50 mW are focused by a 10 cm focal length lens with a beam diameter of 3 mm. While the divergence of the beam is marginal compared to other conical emissions seen in this work, the conical emission seems stable to the eye. A closer look at the spectrum reveals strong fluctuations as can be seen in Figure 3.17 for the high-energy wing below 650 nm. These extreme fluctuations can be explained by temporally-generated local pressure changes inflicted by the strong beam that can last for over a millisecond [213]. When the laser pulse is forming a filament, high intensities heat up the gas and can locally lead to a severe drop in density. In case of air, Cheng et al. [213] showed a drop of the neutral gas number density by over 1.6×10^{18} cm^{-3}, which required about 1 ms to relax by thermal diffusion. These gas density depressions lead to a local change of the refractive index and hence influence the dynamics of the filamentation process. The respective index drop was shown to be as high as $\Delta n \approx 6\times10^{-5}$, leading to a strong defocussing effect. This effectively changes the conditions from shot-to-shot, resulting in a strongly varying spectral density and additional strong noise on the phase. Hence, observing CEP-related fringes has been troublesome, but nevertheless successful with CCD detection. However, the signal was not suitable to be used as a feedback signal and hence not successfully stabilized. Nevertheless, despite enabling measurement of the CEP, these index fluctuations directly couple to the nonlinear phase accumulated in the filament via $\Delta\phi_{\mathrm{nl}} = \frac{2\pi}{\lambda}\Delta n$, which strongly induces additional uncertainty on the relationship between the fringe position and the CEP.

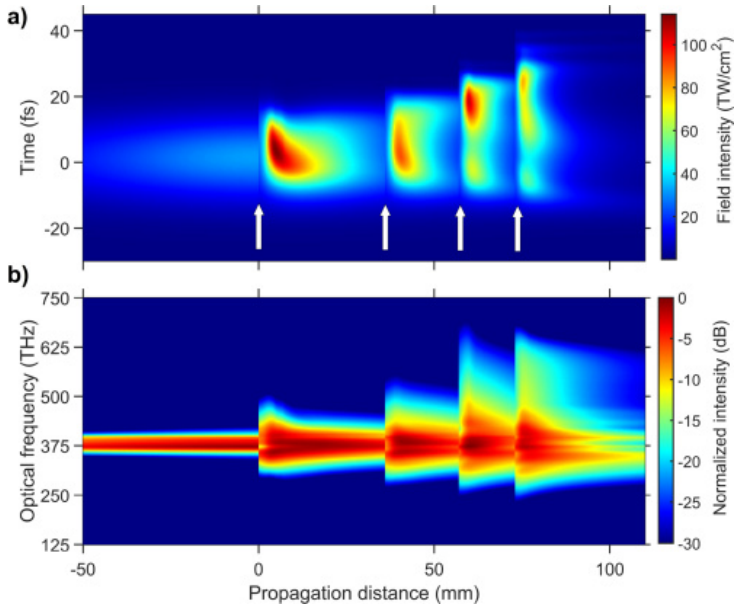

Figure 3.9: Reprinted with permission from [217], OSA, the spatio-temporal a) and spatio-spectral evolution b) is shown as simulated by solving the generalized nonlinear Schrödinger equation for a 25 fs pulse centered at 790 nm propagating through air and an arrangement of four 100 µm thick fused silica plates. Evolution inside the plates is not shown. a) Time evolution relative to moving frame of pulse as a function of propagation distance and the pulse intensity. b) Normalized spectral density while propagating through the arrangement of plates.

Arrangement of Thin Plates

Introduction and Considerations

Recently, Lu et al.[202] have shown that an arrangement of carefully placed thin fused silica plates allows the generation of a high-power supercontinuum with a high conversion efficiency and almost no degradation of the spatial beam quality, phase coherence and polarization properties. As the spectral extension precedes most other nonlinear effects on the pulse [214, 215], the arrangement of thin plates enables to minimize or even omit negative side effects occurring in condensed media above the intensity clamping point. These include the generation of multiple filaments, pulse breakup and finally, optical breakdown, all of which lead to a strong degradation of the spatio-temporal pulse properties including coherence. Hence, limiting the medium thickness and enabling the pulse to recover during propagation in air after highly nonlinear interaction [216], pulse powers and intensities well beyond the critical power and clamping intensity, respectively, can be exploited for SCG. This allows for a much higher fluence over the whole spectrum and is promising to reduce shot noise in the context of CEP detection using spectral interferometry. Three basic criteria are set by Cheng et al. [217] that need to be fulfilled. First, the incident intensity I_0 must not exceed the dielectric breakdown threshold and secondly, the intensity needs to be strong enough for sufficient broadening but nevertheless avoid excess conical emission and hence loss of energy. This can also be expressed in terms of the accumulated nonlinear phase ϕ_{nl} during transmission that should be close to π. Numerically, the optimum value for the accumulated nonlinear phase is found to be around $1.5\,\pi$. The third criteria addresses the need of the pulse to self-heal in order to avoid negative effects. The position of the plates is given by the recovery of the peak intensity to its initial value I_0, which is achieved by the beam divergence and spatio-temporal coupling. Lu et al. numerically solved the generalized nonlinear Schrödinger equation simplified for forward propagation

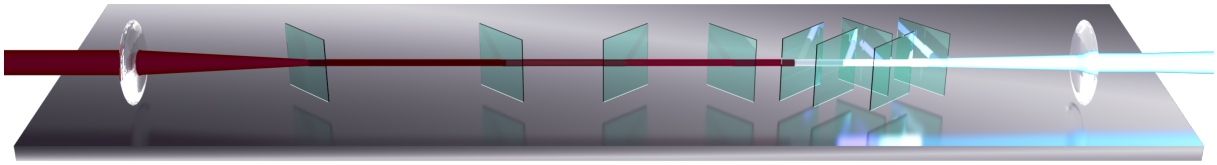

Figure 3.10: a) Thin plate arrangement: two 50 µm thick quartz plates at the front followed by seven 100 µm thick fused silica plates at Brewster angle.

with radial symmetry [26, 202]. In Figure 3.9, the propagation properties of an incident pulse with 25 fs at 790 nm central wavelength are shown.

During propagation through the first plate, the pulse is temporally stretched by roughly 11 % and acquires a nonlinear phase shift of $1.55\,\pi$. After exiting the plate, the pulse experiences self-focusing that leads to an increase in pulse intensity to more than 100 TW/cm^2 at a distance around 1 cm away from the plate. After further propagation, the pulse recovers to its initial intensity due to diffraction, where the next plate can be located. While in the first plate symmetrical spectral broadening caused by SPM is dominant, self-steepening leads to an asymmetric extension into the blue wing already within the second plate. Eventually, this enables the formation of a plateau within the bluish spectral region after multiple plates have been passed.

Experimental Approach

Within this work, a combination of two 50 µm thick quartz plates and seven fused silica plates of 100 µm thickness are used. The implementation of the two quartz plates is necessary to avoid long-term degradation over several tens of minutes that is found here and is probably caused by poor material quality. The latter is most certainly a result of an increased number of defects and color centers that lead to a reduced damage threshold and lower thermal conductivity. Figure 3.10 shows a sketch of the arrangement, which is similar to the previously presented conditions in theory [217] and experiment [202, 218]. Minimizing the reflection by using the plates under Brewster angle conditions (55.5 °), the effective thickness increased from 100 µm to roughly 120 µm for the fused silica plates and from 50 µm to about 60 µm in the case of quartz plates. Pulses with 220 µJ and a spatial beam size of 6.5 mm after an iris are focused by a concave mirror with $R = -5000$ mm. Here the pulse energy is one-third higher compared to [202], which is necessary to achieve similar peak powers as the Fourier-transform limited pulses are at least 35 fs long. AOPDF settings were optimized to achieve the broadest and most stable spectrum.

Despite the fact that the incident pulse has a rather asymmetric spatial beam profile, the resulting conical emission has been optimized to have a homogeneous far field as can be seen in Figure 3.6. Comparable to Lu et al. [202], peak powers P_p of 5.5 GW with pulses of 35 fs are achieved. These powers substantially exceed the critical power of fused silica $P_\mathrm{crit} \approx 2$ MW [38] with a ratio of $P_\mathrm{p}/P_\mathrm{crit} \approx 2750$. As can be seen in Figure 3.5 (black), the spectrum reaches over one octave and ranges from 450 nm up to 980 nm on a -20 dB level. Stretching over one octave, this spectrum is suitable for measuring the CEP. Additionally, a very strong second harmonic component generated at the surface of the thin quartz plates [219] is visible, which vanished upon removal of the quartz plates. In the next section, suitable choices for the second harmonic media are discussed.

SH crystal	800 nm		900 nm		1020 nm		Phase-matching
	d_{eff} (pm/V)	walk-off (mrad)	d_{eff} (pm/V)	walk-off (mrad)	d_{eff} (pm/V)	walk-off (mrad)	PM
KTP	-	-	-	-	2.53	5.2	type 1
KDP	0.3	29.5	0.28	28.9	0.26	28.2	type 1
LBO at 460 K	0.769	14.7	0.821	10.4	0.851	3.12	non-crit.
β-BBO	2	68	2.01	62.4	2.01	57.3	type 1
BiBO	3.72	59.38	3.47	46.75	3.12	31.7	type 1

Table 3.2: Comparison of conversion efficiency d_{eff}, walk-off and phase-matching type of various crystals. Values are calculated using the SNLO package [220].

3.2.5 Choice of Second Harmonic Media

After introducing the different SC media and their necessary conditions as well as resulting spectral densities, an appropriate frequency-doubling source needs to be chosen for the application in f-2f interferometry.

The purpose of SHG in f-2f interferometry is to convert the lower frequency wing of an octave-spanning spectrum to overlap with the higher-frequency part. Then, interference of two frequency combs offset by the carrier-envelope frequency is possible and results in a beating or formation of fringes. In order to ensure the highest possible fringe visibility or beat strength, the spectral density range that is frequency-doubled and the available photon numbers in the high-frequency range within the SC need to be considered. In contrast to the choice of materials regarding filamentation-based spectral broadening, an increased nonlinear coefficient is favorable in order to maximize the second harmonic photons. Other important parameters include the effective nonlinear coefficient d_{eff}, optical damage threshold, phase-matching or acceptance bandwidth, angular acceptance, and walk-off, where the latter three depend on the birefringence and chromatic dispersion of the crystal. The most common media for frequency-doubling include $KTiOPO_4$ (KTP), KH_2PO_4 (KDP) and borates such as LiB_3O_5 (LBO) and β-BaB_2O_4 (BBO). Table 3.2 provides an overview on the most common frequency-doubling crystals as well as BiB_3O_6 (BiBO), including the effective nonlinearity d_{eff} and respective walk-off for the wavelength range of interest.

Although KTP offers a relatively high nonlinear coefficient, which would make it a very good choice to increase photon numbers for wavelengths above 1000 nm, it suffers from a rather low optical damage threshold that limits its usability to weak incident intensities. KDP, on the other hand, features a much lower nonlinear coefficient, excluding it from the desired application completely. Borates however are very promising candidates as will be discussed further on.

In the context of amplifier CEP measurement, BBO is the one most widely used due to its high nonlinear coefficient, high optical damage threshold and its readily achieved critical phase-matching at room temperature. Yet, it is characterized by a relatively strong walk-off. Other common crystals include non-critically phase-matched lithium triborate (LBO) at 460 K with a strong conversion efficiency at low light levels [16]. Another regularly employed SH source is periodic-poled magnesium-oxide doped lithium niobate (MgO:PPLN or PPLN) [221], which enables the optimization of the conversion range by precise tuning of the poling period and the operation temperature. Although the latter crystal has a desirable high optical damage threshold, it nevertheless has only a small acceptance bandwidth $\Delta\lambda$ of roughly 0.5 nm.

SH crystal	Temp. (K)	λ_{SH} (nm)	$\Delta\lambda$ (nm/length)	l (mm)	d_{eff} (pm/V)	PM
LBO	460	1020	6	10	0.85	non-crit.
BBO	300	1020	18	2	2.0	type 1
BiBO	300	1020	8.7	2	3.1	type 1
PPLN	450	1020	0.5	0.45	16.0	QPM

Table 3.3: Direct comparison of the most common second harmonic crystals that includes their acceptance bandwidth $\Delta\lambda$. Values are calculated using the SNLO package [220].

This renders PPLN not suitable in the context of spectral interferometry as it is virtually impossible to resolve spectral fringes to a proper extent in the employed spectrometer. An overview on common SH crystals is given in Tab. 3.3. In earlier published results by Koke et al. [16] a LBO was employed as a second harmonic source. While walk-off effects can be largely minimized, the required heating to around 460 Kelvin renders the SC source rather unfavorable for commercial application. Additionally, frequency-doubling at lower wavelengths requires heating to even higher temperatures. Furthermore, the rather low conversion efficiency d_{eff} of below 1 pm/V also limits its application to maximize photon numbers.

In order to maximize the photon numbers at the end of the involved nonlinear processes, the spectrum of the supercontinuum source needs to be considered when choosing the second harmonic crystal. As can be seen in Figure 3.5, sapphire and CaF_2 are reaching far into the IR, allowing frequency-doubling at around 1020 nm, while the thin plates and xenon at 8 bar require a shorter wavelength range to be frequency-doubled, which is around 960 nm and 880 nm, respectively. Focusing the discussion on 1020 nm, where most borates such as BBO or BiBO [222] can be easily critically phase-matched at room temperature, reliable and strong second-harmonic generation can be possible [223]. Thicknesses of 2 mm are commonly used for SH generation with acceptance bandwidths of at least 10 nm, which enables to resolve several fringes properly. In the CaF_2 setup a 2 mm thick BiBO is used for frequency-doubling at 1020 nm, which has a 1.5 times increased nonlinear coefficient compared to BBO [222]. Additionally, this crystal features a relatively large spectral acceptance bandwidth, a reduction of the spatial walk-off compared to BBO by a factor of two and additionally, a low temporal walk-off [224, 225]. Hence, it provides nearly perfect conditions for frequency-doubling in spectral interferometry. To conclude, critically phase-matched borates are employed, where walk-off effects are found to be tolerable. While in the sapphire-based detection setup a BBO with a thickness of 2 mm is used, the higher peak powers available in the xenon and the thin plates arrangement require a much thinner BBO of only 0.5 mm thickness. Especially in the latter case, the increase in acceptance bandwidth due to the thickness reduction enables the formation of fringes.

3.2.6 Experimental Design

The different conditions essential for optimized SCG of the presented sources in section 3.2.4 make it necessary to adapt also the interferometer design to their requirements. To this end, four different optical detection schemes are presented in Figure 3.11, where the SH is chosen as elucidated before according to the varying asymmetry of the respective SC spectra. The first setup is the most commonly implemented scheme. It includes sapphire as a white-light source and BBO for frequency-doubling in a type 1 configuration. This requires subsequent projection of the s- and p-polarized components on the

Source	Thickness (mm)	Focus (mm)	SH	SH thickness (mm)
Sapphire	2	100	BBO	2
Xenon	1.6 × 8 bar	150	BBO	0.5
Thin Plates	7 × 0.1 f.silica+2 × 0.05 quartz	2500	BBO	0.5
CaF_2 (rot.)	2	100	BiBO	2

Table 3.4: Experimental conditions of SCG sources employed for CEP measurement and stabilization. Thickness of xenon is given by the product of Rayleigh length times the pressure.

same plane by employing a polarizer. The common-path interferometer enables to avoid noise pickup as would be present in an unshared beam path configuration comparable to noise reduction found in f-2f interferometry [140]. The fringe spacing can be controlled by adjusting the group delay between the bluish and infrared by inserting additional dispersion prior frequency-doubling. For all four schemes, the interference of the second harmonic and the fundamental is resolved in a half-meter spectrograph with a grating exhibiting a 500 nm blaze wavelength. Focusing conditions, employed thicknesses and further parameters can be found in table 3.4 for all setups.

The interferometer design for the CaF_2 plate-based detection scheme is shown in Figure 3.11 b). Although quite similar to the common sapphire plate arrangement, it includes additional polarization management, which is required due to the rotation of the CaF_2 plate to avoid damage and achieve reliable SC output. To this end, two quarter waveplates are employed. While the first one is situated prior to SCG, back-conversion from circularly to linear polarized light is carried out after SHG to minimize stray light in the spectrometer. With the higher nonlinearity compared to BBO, BiBO [222] is found to perform better under circular polarization conditions.

In order to allow a strong power increase from around 3 and 10 mW in the case of sapphire and CaF_2, respectively, to several tens and even hundreds of milliwatts, a change in the interferometer design is necessary. While sapphire and CaF_2 are used in a common-path configuration, a Mach-Zehnder design is better suited for high powers to avoid damage of the second harmonic crystal from the unconverted spectral part around the seed at 790 nm. Further, as the remaining octave-spanning spectrum can be very strong, higher-order effects such as SPM and four-wave mixing as well as optical damage within the SH crystal may occur. To avoid this, a high-pass filter arrangement is used. After supercontinuum generation in either the thin plates setup as explained in section 3.2.4 or in a gas cell filled with xenon at 8 bar the spectrum is separated at 900 nm in the former and 850 nm in the latter case. With the longer wavelength range further focused in a BBO of 0.5 mm thickness, the remaining seed around 790 nm together with the spectral extension into the UV is propagating through a delay stage and is subsequently separated by a high-pass filter in the residual pump beam above 600 nm and the blue wing of the SC. Then, the latter is reunited with the frequency-doubled part by a 50/50 beam splitter. After matching the polarization of the second harmonic and the fundamental using a polarizer, fringes are resolved in the spectrometer.

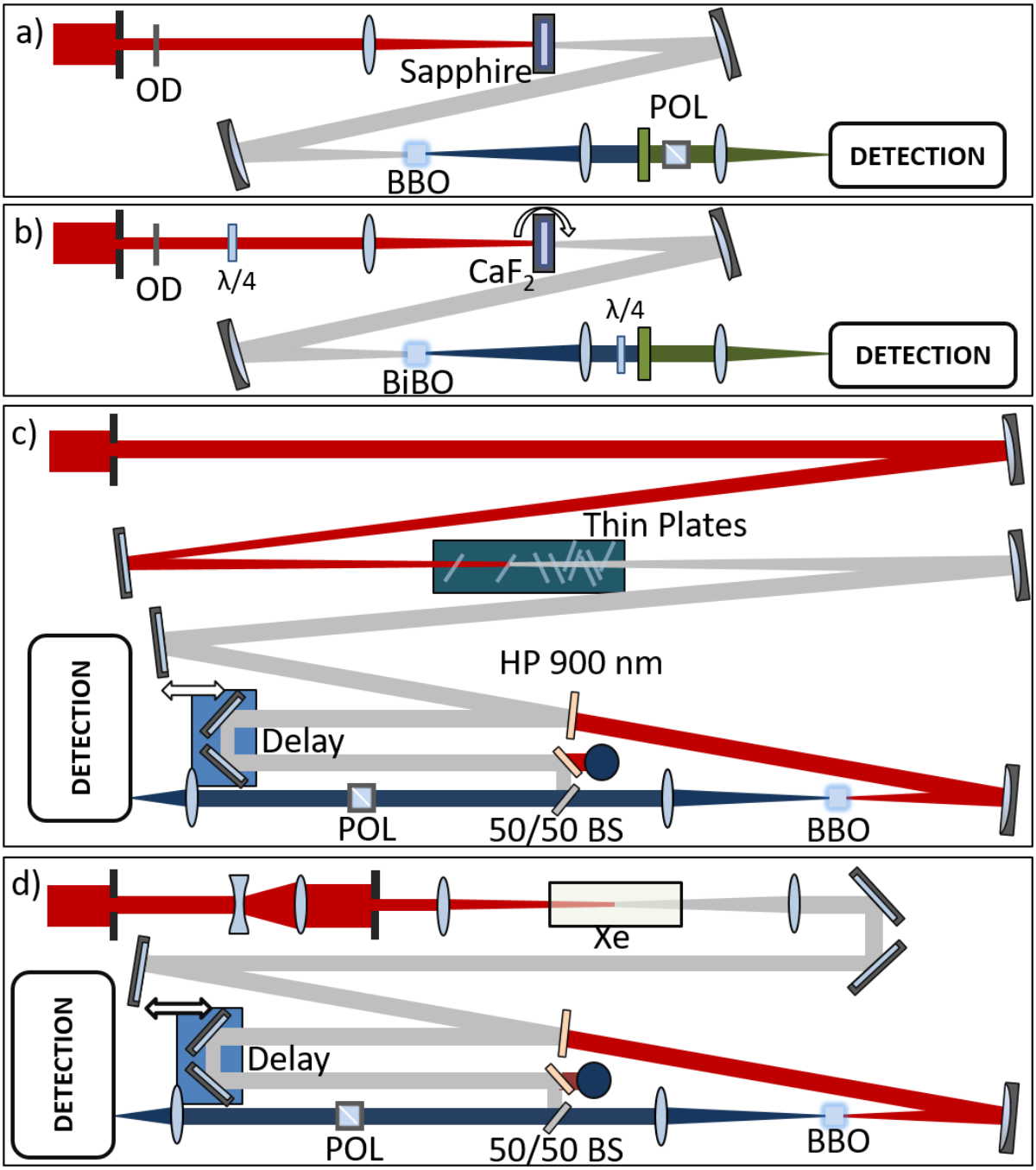

Figure 3.11: Employed f-$2f$ interferometer arrangements. a) Reference sapphire/BBO setup, b) CaF_2/BiBO setup, which includes one quarter waveplate prior SCG and a second one after the SH step. c) Thin plates arrangement consisting of two quartz (50 µm) and seven fused silica plates (100 µm). d) Xenon gas cell arrangement.

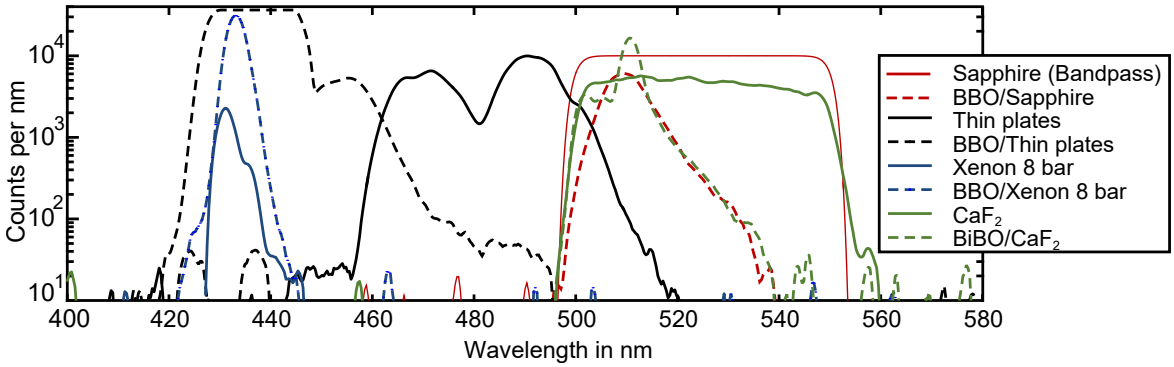

Figure 3.12: Spectral isolation via bandpass filtering (525±25 nm) for sapphire and CaF_2 and by a prism-based arrangement for xenon and the thin plates arrangement.

3.3 Optimized CEP Detection

Earlier established combinations of SCG medium and SH crystal are experimentally realized in order to first measure the available photon numbers and subsequently, estimate the residual CEP noise originating from shot noise. Then, the CEP of the oscillator is stabilized and the presented f-$2f$ detection designs are separately used to additionally stabilize the amplifier. Finally, the performance of the amplifier loop is discussed, including the resulting fringe visibility.

3.3.1 Shot Noise-Induced Residual CEP Jitter

In this part the shot noise-induced contribution to the residual phase jitter of the amplifier is estimated by measuring the available photons in the spectral regions of interest. Then, these numbers are compared to the numerically obtained values. Table 3.5 gives an overview of the measured photon numbers for each SC source and subsequent SH process, which have been corrected for the efficiency of the diode. In order to maximize the fringe contrast by increasing photon numbers and hence the precision to measure the CEP, the spectra of the supercontinuum sources as shown in Figure 3.5 are analyzed for the strongest spectral density, for both, the IR and the respective second harmonic region. The obtained regions of interest as well as the central wavelength λ_c are given in table 3.5. Furthermore, the selected spectral regions are shown in Figure 3.12. For sapphire and rotating CaF_2 as well as their respective second harmonic sources the isolation of the spectral bandwidth was carried out with a simple bandpass filter centered at 510 nm. Hence, the second-harmonic generation of both setups is carried out at around 1020 nm, which leads to 510 nm. In the case of the xenon and the thin plates arrangement, the actual photon numbers are measured by using a prism-based approach. The prism spectrally resolves the different components of the SC as well as the SH and subsequently, only a small region is incident on a diode, while the rest is blocked. In this way, the overlap of the SH and the fundamental spectral content is achieved, which allows to measure their respective photon numbers.

While the second harmonic of both, CaF_2 and sapphire agree well in spectral shape, the actual photon count resulted in a ten times increase in favor of the former. This strong gain in second harmonic photons compared to the reference setup relying on sapphire and BBO is most certainly due to the higher available fluence at 1020 nm as a result of the increase in overall supercontinuum fluence with the higher critical power of CaF_2. Additionally, the increase can be attributed to the 1.5 times larger nonlinearity of BiBO

Source	λ_c (nm)	Filtering	SCG($\times 10^6$)	SH($\times 10^6$)	one fringe ($\times 10^6$)
Sapphire & BBO	510	510 ± 25 nm	700	300	5
Xe (8 bar) & BBO	437	Prism-based	180	8.800	-
Thin Plates & BBO	475	Prism-based	15.000	9.400	26
CaF_2 & BiBO	510	510 ± 25 nm	12.000	4.600	100

Table 3.5: Measured photon numbers per pulse in the employed schemes around their respective region with center wavelength λ_c for the supercontinuum, second harmonic and one selected interference fringe.

compared to BBO. Hence, these advantages also translate to an increase of the detectable single fringe photons. Despite the fact that the thin plates arrangement leads to a comparable number of photons relative to CaF_2 and a twice as high SH photon count, the actual fringe contrast is degraded. This is most certainly a result of beam spot degradation, which deteriorates spatial and temporal overlap. Beam spot degradation is probably caused by the additional optics that are necessary to handle high peak powers. These include a beam splitter and two high-pass filters.

Figure 3.13 provides the shot noise-induced CEP jitter for the traditional digital FFT-based phase extraction algorithm commonly applied in spectral interferometry, where multiple fringes are detected by a CCD camera. The expected $\pi/\sqrt{N}$ behavior of the shot noise-inflicted CEP jitter within the employed all-analog fast f-$2f$ interferometer is given. Furthermore, single fringe photon numbers for the newly presented schemes and their respective shot noise-induced CEP jitters are provided. In earlier results obtained by Koke et al. [16] that employed sapphire in combination with LBO for generating the supercontinuum and the second harmonic, respectively, an estimated 32.000 photons [16] within a 1 nm wide fringe were detected that readily translate to roughly $\pi/\sqrt{32.000} \approx 20$ mrad for the shot noise-induced residual CEP jitter. Nevertheless, this estimation does not include imperfect interference and unbalanced photon numbers of the second harmonic and fundamental. Therefore, the shot noise contribution is expected to be even higher. Additionally, at such low photon numbers, electric contributions during detection may further increase the single-shot jitter. Koke et al. [16] estimated the spurious noise contribution to be approximately 40 mrad in this fast f-$2f$ interferometer scheme.

With the reference setup based on sapphire and BBO, however, the measurement of a single fringe results in 5×10^6 photons, which is an increase of about two orders of magnitude in photons as compared to 32.000 photons earlier presented by Koke et al. Hence, a reduced shot noise-induced CEP jitter within the lower single digit milliradian is expected. For the thin plates and CaF_2 the shot noise influence can be estimated to reach even below 1 mrad. While the presented photon numbers do not account for the earlier mentioned fringe contrast degradation effects due to polarization mismatch and coherence loss, this strong increase in photon numbers nevertheless reduces the influence of shot noise and electric contributions to a negligible extent. Therefore, the influence of shot noise on the CEP detection should be small and an improved overall CEP stability performance can be expected.

To summarize, the shot noise and related contributions such as the effect of asymmetric f and $2f$ photon numbers are minimized to the possible extent by increasing photon numbers well above one order of magnitude compared to earlier presented results. Therefore, a strongly reduced shot-to-shot jitter to about 160 mrad can be expected. The phase noise density and hence the integrated phase noise are both expected to be only weakly affected by shot noise. Additionally, in a second step, noise features previously hidden are expected to be revealed, which enables a subsequent minimization of the overall shot-to-shot jitter. By making use of this two-step approach, sub-100 mrad jitters within the range of the

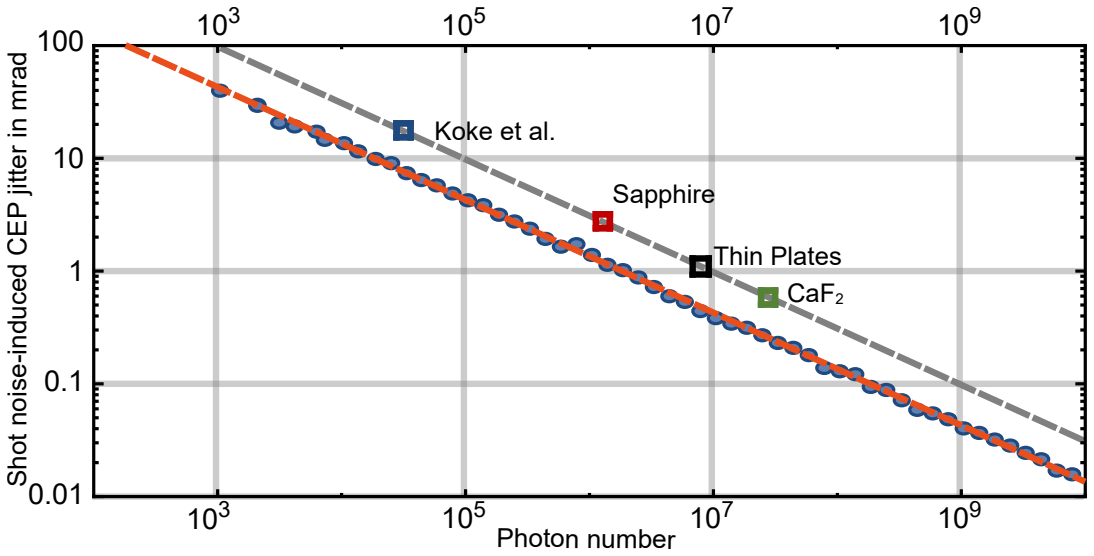

Figure 3.13: Expected shot noise-induced CEP jitter in mrad, for the fast f-$2f$ interferometer approximately scaling with $\pi/\sqrt{N}$ (grey dashed dashed) and the numerical simulation of CCD-based detection (orange dashed line). While Koke et al. estimated the detection of 32.000 photons by the PMT's at the back-end of the fast f-$2f$ interferometer, here an increase to roughly 5×10^6 is found that leads to a shot noise-induced CEP jitter of only a couple mrad. In the case of the thin plates arrangement and CaF_2, the residual jitter is estimated to below 1 mrad. In all cases, the efficiency of the PMT's of roughly 30 % is taken into account. Additionally, imperfect interference and asymmetric photon numbers between second harmonic and fundamental may further reduce the fringe visibility and hence increase the detection uncertainty.

oscillator performance should be within reach.

3.3.2 CEP Measurement and Stabilization

Employing the spectral interferometry designs presented in section 3.2.4 with a feedback CEP stabilization as explained in part 3.2.3, the CEP is measured and subsequently controlled. With the given capabilities of the detection scheme, single-shot evolution of the CEP is resolved, while subsequent low-pass filtering with a 1 kHz filter is required when used for stabilization. Low-pass filtering was necessary to avoid switching artifacts of the boxcars and hence a deterioration of the CEP stability. The measured and 1 kHz filtered signal of the reference scheme that relies on sapphire and BBO is shown in Fig. 3.14 a), where an jitter of 109 mrad over more than 200 s is achieved. Assuming a Gaussian error distribution, the actual jitter requires a multiplication by the square root of 3.168, which results in 195 mrad. When analyzing the signal in the Fourier domain, a corrected integrated phase noise (IPN) of 185 mrad is measured, which is below the earlier presented 210 mrad [16]. The difference can be attributed to the increase in photon numbers. The histograms in Figure 3.14 show a close to Gaussian error distribution that allows the earlier argued single-shot correction. The Gaussian error distribution can be a result of residual shot noise influence or any other white noise source. Another possibility is that it stems from pump-power fluctuations as was indicated by [182]. Nevertheless, provided that it is not of technical origin, which would increase the correction factor further, the above assumption is expected to be valid. Interestingly, compared to Koke et al., only a small improvement could be seen in the performance of the stabilization scheme, despite a two orders of magnitude increase in detected photon numbers. Compared to the stabilization with the reference, CaF_2 in combination with BiBO shows a similar performance, where a

corrected IPN of 190 mrad is measured. As can be seen in Figure 3.14 b) multiple single-shot excursions in combination with the need to rotate the CaF_2 plate most certainly have deteriorated the effectiveness of the CEP detection and hence stabilization. This resulted in a slightly non-Gaussian error distribution, which makes it necessary to interpret the corrected IPN of CaF_2 with caution. Nevertheless, the effect of the rotational movement seems to have a rather weak influence on the performance, as can be seen from the practically invisible contribution within the integrated phase noise in Figure 3.15 at around 6-7 Hz. Despite the strong increase in photon numbers compared to the reference, no severe improvement in the performance of the stabilization scheme could be seen and a white noise floor is observed, while most noise is accumulated above 1 kHz.

Utilizing the thin plate arrangement to stabilize the CEP results in a higher corrected residual noise, accumulating to a corrected IPN of 280 mrad over 120 s. This rather large difference in performance compared to the reference can be of multiple origin, while the unprotected, strongly increased beam paths as a result of the adapted interferometer designs are one potential origin. The increased beam paths were necessary to obtain the required focusing conditions. Table 3.6 provides an overview of the stabilization performance of all employed schemes.

The integrated phase noise shown in Figure 3.15 clearly emphasizes that in all schemes most noise is accumulated above 1 kHz despite filtering. This indicates the limited performance of the oscillator on the amplifier stabilization. Furthermore, high-frequency pump fluctuations and additional noise that is accumulated due to the boxcars and low-pass filtering can explain the high-frequency contributions to the overall CEP jitter. The phase noise densities of the stabilized amplifier measurements are dominated by white noise that, according to previous estimate, should not be originating from shot noise. A technical origin is unlikely too, as this would lead to noise of limited bandwidth. This is in accordance with the observations seen in the previous section, where white flat frequency noise that is dominating the noise floor is potentially originating from the detection.

Nevertheless, various contributions by electronics in the frequency range of 50 Hz to 1 kHz are visible in all schemes that are line harmonics and aliases. Additionally, selective broader acoustics are visible in all measurements, contributing particularly strong to the IPN at 200 Hz in the thin plates arrangement. The phase noise density (PND) clearly shows the performance of the combined stabilization of oscillator and amplifier, where the $1/f$ or flicker noise, which is present in all measurement schemes, is strongly reduced up to roughly 500 Hz or even beyond. The $1/f$ noise is also particularly strong when only the oscillator is stabilized. Furthermore, it is reaching far into the high-frequency region, which also emphasizes the reduction of white noise that would otherwise cover the $1/f$ noise. Nevertheless, the strong $1/f$ noise can be of various origin, but due to the short timescale covered by the measurement rather points into the direction of a coupling mechanism within the laser. Furthermore, the periodic opening of the water valves in the cooling circuit at roughly 0.4 Hz can be seen in all measurement schemes. Especially in the Mach-Zehnder configuration that was used for the thin plates arrangement, angular walk-off and spectral modulation of the SC impeded to make use of the full second harmonic bandwidth during detection. Then, maximizing the photons within the fringes by reducing their numbers to a few is not always possible.

Overall, substantially increasing photon numbers and minimizing related influences on the CEP such as shot noise during detection enabled a performance improvement in the reference measurement based on sapphire/BBO. Nevertheless, the obtained results for the other detection schemes are at best compara-

Source	rms (mrad)	corr. rms (mrad)	corr. IPN (mrad)	length (s)
Sapphire & BBO	109	195	185	250
CaF_2 & BiBO	113	201	190	270
Thin Plates & BBO	150	270	280	120

Table 3.6: Measured and corrected stabilization performance of all three fast f-$2f$ interferometer designs with different combinations of SCG and SH. The single-shot equivalent or corrected noise can be estimated for dominating Gaussian error distribution by multiplication with $\sqrt{3.17} \approx 1.8$.

ble in performance. This is in contradiction to the expectations. Furthermore, the measurements are still dominated by white noise that shows dominating contributions above 1 kHz. Isolating single contributors to the overall residual single-shot jitters was therefore not directly possible. Additionally, performance-related fringe contrasts and strong shot-to-shot fluctuations of the supercontinuum are observed. Hence, further analysis into the latter two observations is conducted in order to investigate the constraints that hinder sub-100 mrad CEP stability on a shot-to-shot basis.

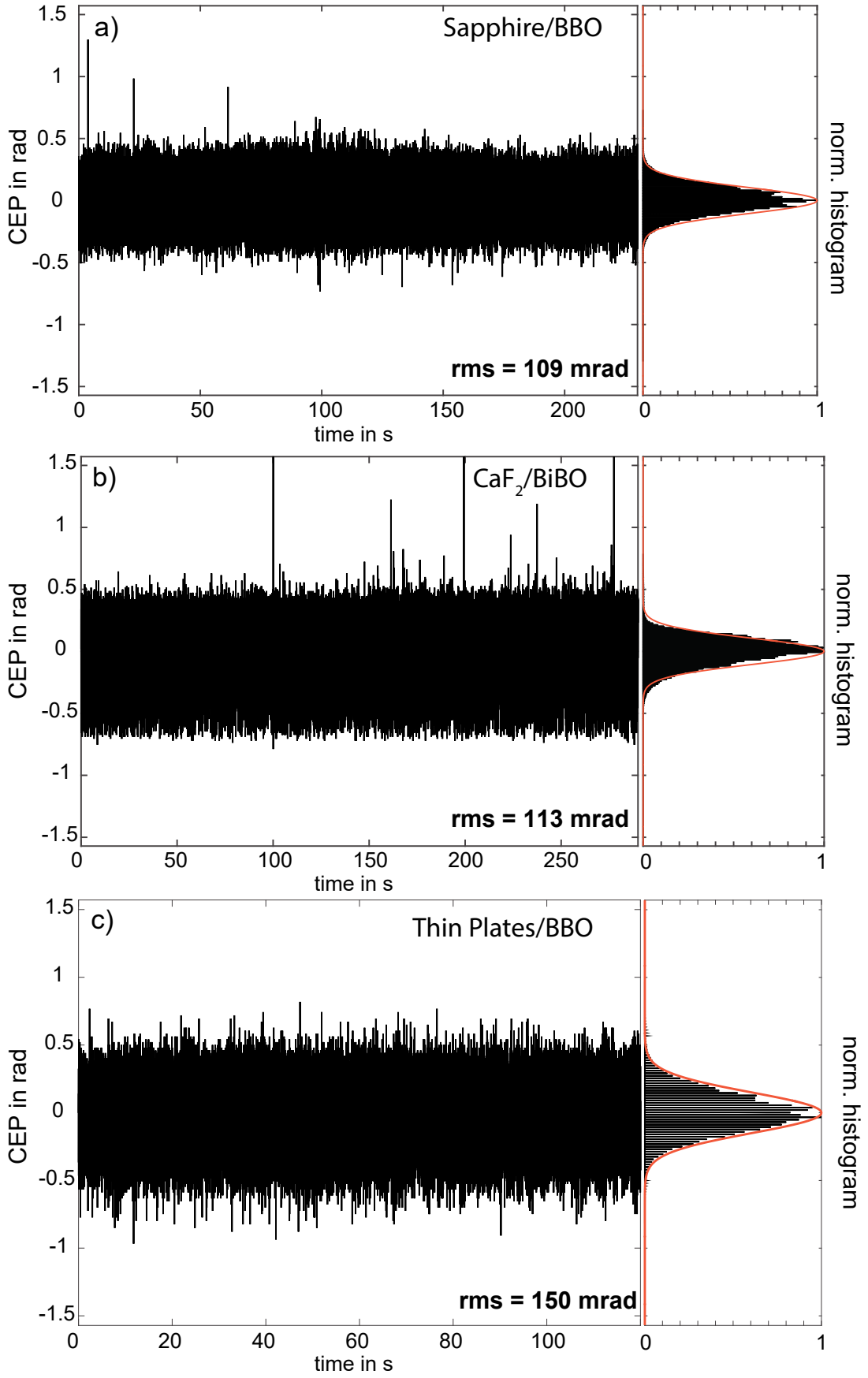

Figure 3.14: Residual CEP jitter obtained from the difference voltage signal, which is then filtered by a 1 kHz low-pass. Additionally, the normalized CEP error spread is compared to a Gaussian distribution (red). In a), the reference setup employing sapphire and BBO, in b), a combination of CaF_2 and BiBO and, in c), the thin plates arrangement with a 0.5 mm BBO is shown. The root-mean-square of the time series is given.

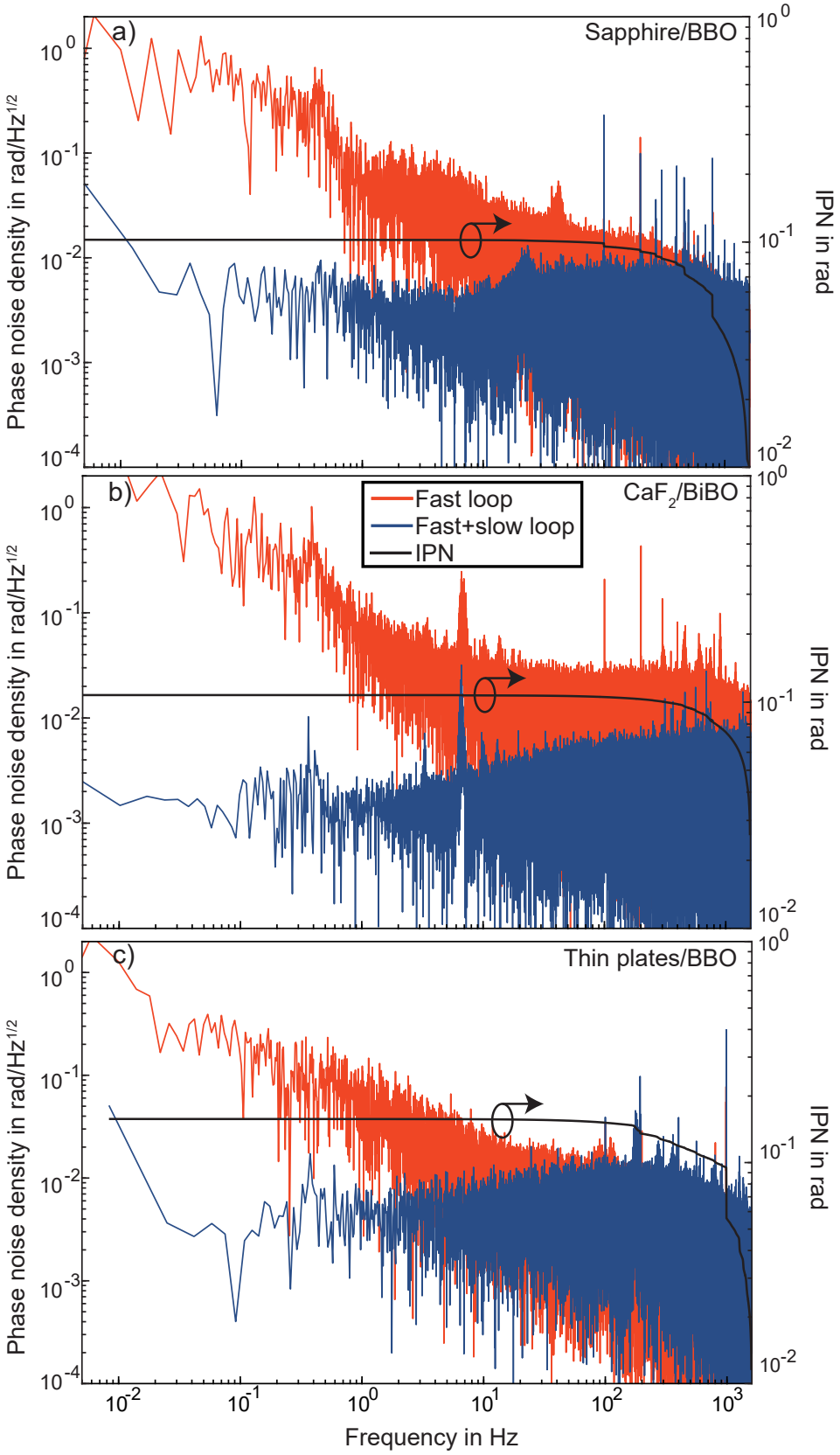

Figure 3.15: Phase noise density (PND) of the stabilized oscillator only (orange) and combined with amplifier stabilization (blue). Furthermore, the integrated phase noise (IPN) (black) of the 1 kHz low-pass filtered CEP is given. The measurements in a) for sapphire/BBO, in b) for CaF_2/BiBO and c), for the thin plates arrangement combined with a thin BBO are shown.

3.3.3 Fringe Visibility and Fluctuation of the Supercontinuum

In order to understand the observed performance limitation in more detail, the fringes were resolved over 2000 shots by using a CCD camera. Employing Fourier filtering, the modulation sideband and the background were extracted and subsequently deducted from each other, which resulted in the absolute fringe strength. Additionally, the standard deviation for each pixel is calculated. Finally, the normalized fringe contrast is obtained by taking the ratio of the absolute fringe strength to the standard deviation as can be seen in Fig. 3.16.

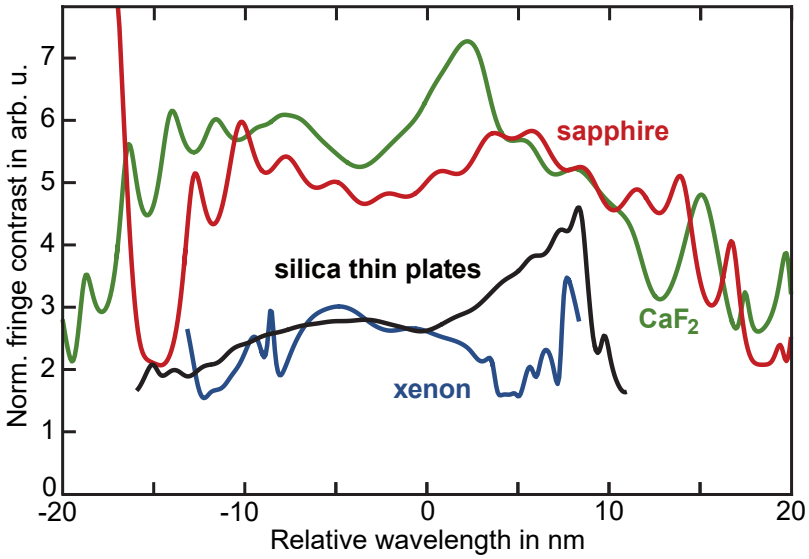

Figure 3.16: Normalized fringe contrast at the back-end of the detection scheme. 2.000 shots have been measured for all four SC sources and their respective second harmonic. The absolute values were obtained by Fourier filtering, which removed the background. Subsequently, the standard deviation at each pixel was calculated and the ratio of both is taken.

The normalized fringe contrast agrees well with the measured performance of the CEP stabilization schemes and indicates a potential correlation. While sapphire and calcium fluoride show a comparable contrast, the thin plates arrangement provides similar results only within a small wavelength range, where the spectral overlap is strong and fluctuations are small. Fringes from xenon, however, clearly show the expected weak normalized contrast over the whole frequency-doubling bandwidth. One possible explanation for the reduced normalized fringe contrast is found if the pulse-to-pulse variations of the SC sources are analyzed. The incident seed from the amplifier was measured to have a coefficient of variation of 2.3 % within 10 s. Earlier presented results for the same system showed fluctuations of below 1.8 % [16]. This discrepancy probably is a result of the aging pump laser. Noise amplification during spectral broadening is analyzed by measuring the high-frequency edge below 650 nm by introducing a low-pass filter with cut-off at 650 nm prior measurement by a photodiode. The SC process has led to a reasonable amplification of spectral density fluctuations for sapphire and CaF_2 with 4.6 % and 4.9 %, respectively. The difference between CaF_2 and sapphire most certainly is due to the required rotation of the former, which can be seen in the Figure 3.17. Furthermore, for the thin plates arrangement fluctuations of 9 % were measured in this spectral region. The gas cell filled with xenon at 8 bar shows severe fluctuations exceeding 50 %, which makes it unsuitable for CEP stabilization. This has been explained in section 3.2.4, where this unexpected behavior is concluded to result from the necessary tight focusing required for using a small, high-pressure gas cell. As the spectral density is not perfectly constant over the entire

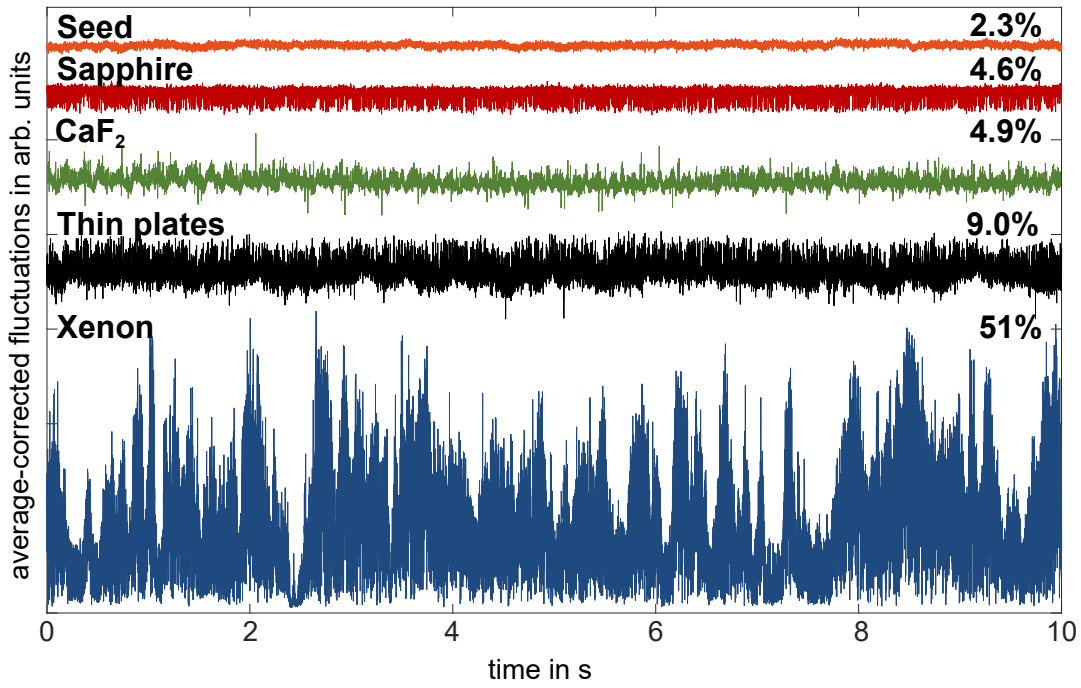

Figure 3.17: Average-corrected 10 s fluctuation of the seed and the employed SCG sources, while for the latter a SP650 low pass filter with cut-off at 650 nm was used. The coefficients of variation are given in percent.

measurement period in all sources, fluctuations will lead to additional noise as the responsivity of the detector varies with frequencies. Nevertheless, using a bandpass at 525 $\pm$25 nm results in comparable variation coefficients, which indicates the validity of the presented variation coefficients.

The question remains to what extent these power fluctuations lead to additional CEP uncertainty that is introduced by the measurement process, i.e., the degradation of the fringe contrast as seen in Fig. 3.16. This is addressed in the next section.

3.3.4 Power Fluctuations and CEP Stability

Noise and fluctuation amplification during SCG has been intensively studied in the realm of SCG in optical fibers, where a strong, nonlinear amplification of input noise is found to cause drastic shot-to-shot intensity fluctuations [226, 227] and even inhibit proper compression into the short few-cycle regime [138]. The nonlinear noise amplification has also been employed to detect faint signals [167, 228, 229]. However, in the context of bulk supercontinuum generation the effect of input noise is still under active research. Majus et al. [230] have evaluated the rms error of spectral intensity fluctuations of a SC generated in 3 mm thick sapphire using a 1 kHz Ti:sapphire-based system with 130 fs pulse duration for 2000 consecutive shots. In Figure 3.18 four regimes are given, ranging from the initial stage **A** to the fully saturated regime **D**. The latter is similar to the region where this work is carried out. Here, reaching for the broadest spectral extent with the highest spectral density is necessary to minimize shot noise. With only 0.4 % intensity fluctuation of the seed, Majus et al. see a 1-4 % fluctuation in the SC. Considering the much higher seed fluctuation found in the experiment here, an averaged value of 4.6 % compares favorably well.

In literature, several values for energy-to-CEP coupling can be found. For example in a hollow-core fiber broadening scenario a CEP shift of 128 mrad/1% energy change was measured [231]. In

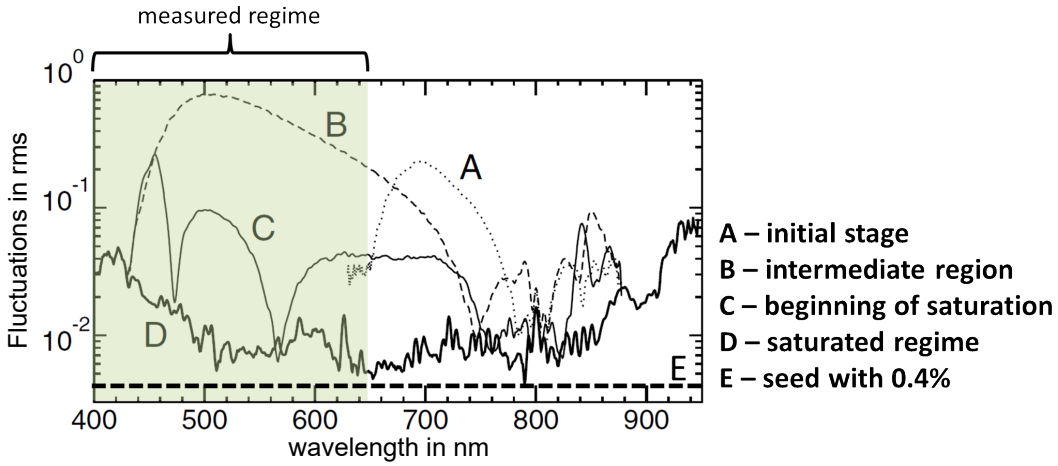

Figure 3.18: Adapted with permission from [230], OSA. SC spectral intensity fluctuations for sapphire with an incident 130 fs long Gaussian pulse measured over 2 s. The corresponding input regimes are given.

sapphire, energy-to-phase coupling was estimated to be 160 mrad/1% change [25]. Another measurement conducted at 800 nm central wavelength indicated an amplitude-to-phase coupling of around 84 mrad [5]. These values, however, do not fully agree with the measurements conducted here, as they imply at least 200 mrad additional jitter in the most favorable case due to the strong fluctuations present. Furthermore, these values cannot describe the fringe degradation that is observed in Figure 3.16.

3.3.5 Discussion

While investigations revealed a strong dependence of the CEP stability loop performance on the fringe contrast, the overall measurement precision may very well be limited. Many authors have indicated strong incident power fluctuations to CEP coupling in different measurement scenarios [5, 25, 231]. However, these can not completely explain the observed performance limitation of the 185 mrad corrected integrated phase jitter. Other possible sources for fringe contrast degradation need to be considered. While the interferometer design can lead to strong additional noise due to beam path variations if unshared paths are large, in most cases, this can be circumvented by using a quasi common- or truly common-path interferometric designs as has been carried out for the sapphire and CaF_2 schemes. This is not applicable in the case of xenon and the thin plate arrangement, where the peak powers are high and damage of optics after supercontinuum generation otherwise occurs. However, the interferometer contributions are mainly limited within the lower frequency region and cannot readily explain contributions accumulating above 1 kHz. Another potentially limiting constraint is the design of the spectrometer. It is of fundamental importance to minimize aberration in order to obtain clear, undistorted fringes. To this end, true Czerny-Turner designs are best suited, where disturbances of the wavefronts (astigmatism) can be partly corrected due to appropriate arrangement of spherical mirrors [232]. This has been realized by the use of a commercial spectrometer. Additionally, environmental noise sources could be responsible for performance degradation, too. However, these noise sources would need to show severe contributions to the integrated phase noise that is not seen in Fig. 3.15 and would depend on the measurement scheme. Only in the case of the thin plates arrangement a strong contribution is present at 1 kHz, which most certainly stems from boxcar glitches.

Decreasing fringe contrast in interferometric measurements has been traditionally explained by a

loss of temporal or spatial coherence. Degrading coherence properties have also been observed during supercontinuum generation. For example, temporal coherence has been found to be readily diminished during spectral broadening in fibers [137, 233], where subsequent compressibility of the pulse train has been limited to well above the bandwidth limit [138]. In general, for filamentation-based broadening no such effect has been found [234]. Nevertheless, as it is important to differentiate between temporal, spatial and spectral coherence, while temporal coherence might be unaffected, spectral coherence can still be degraded. In this sense, the phase relationship within parts of the octave-spanning spectrum may be compromised and their interference after frequency-doubling deteriorated. This would lead to additional white noise during detection of the CEP in f-$2f$ interferometry on a shot-to-shot basis and could explain the observed high-frequency white noise. Therefore, investigations focusing on the possible loss of coherence are carried out in the second half of this chapter, where the actual induced uncertainty during spectral extension in relation to the dominating broadening process under the influence of energy fluctuations is analyzed.

3.3.6 Concluding Remarks on the Reduction of Shot Noise Influence in f-$2f$ Interferometry

It was originally expected that the limited number of available photons at the back-end of the f-$2f$ interferometer, especially after the second harmonic step, restricts CEP detection precision. While the pulse energy after subsequent amplification is much higher as straight out of the oscillator, the usable fraction for supercontinuum generation is limited by the critical power and finally, optical damage. In order to lessen this problem, the use of dielectric media for spectral extension with lower effective nonlinearities thus enabled to increase available photon numbers well beyond one order of magnitude compared to earlier results. To this end, three novel ways of generating an octave-spanning spectrum were explored, which included the use of CaF_2, a thin plate arrangement as well as a high-pressure xenon cell. Despite a significant increase in photon numbers, the expected performance increase is not seen and only slightly reduced jitters are found for the reference scheme relying on sapphire and BBO. This finding indicates that shot noise can pose a problem in inefficient interferometric setups, where photon loss readily occurs. However, novel materials that lead to increased spectral densities over the octave-spanning spectrum do not necessarily improve the situation drastically as they typically come with other drawbacks.

The phase noise density given in Figure 3.15 clearly shows increased $1/f$ noise dominating up to high frequencies in the case of an unstabilized amplifier. This indicates a severe reduction of white detection noise, namely shot noise. Nevertheless, while the $1/f$ noise dominance can be caused by a variety of processes, it is believed to be rather of technical origin arising within the kHz laser system. From this observation it seems as if an increase in photon numbers actually spoils the measurement by leading to an increased coupling of laser noise into CEP noise. Additionally, the suspected coupling mechanism is further supported by the finding of a reduced fringe contrast at the back-end of the detection scheme. While the experimental conditions, i.e., the laser source and stabilization loop performance, can be expected to show comparable output in all measurement schemes and only the detection is changed, the fringe contrast varied by close to a factor of 3 for the different detection schemes. Traditionally in optics, a reduction of coherence is quantified by the loss of the fringe contrast within an unbalanced Michelson interferometer. While in this scenario, coherence is considered for the same wavelengths with a non-zero delay, f-$2f$ interferometry involves the interference within an octave-spanning spectrum, where super-

position of the second harmonic and the fundamental at zero delay is of interest. This is later introduced as intra-pulse coherence, which fundamentally differs from inter-pulse coherence. The latter is typically used to assess the compressibility of pulses close to the Fourier limit. To preliminary conclude, increasing the number of photons at the back-end of the detection may further introduce increased coupling of laser pulse energy fluctuations into CEP noise. Thereby, it may lead to additional $1/f$ noise and a strongly varying fringe contrast. These findings are further illuminated in the upcoming section.

3.4 Coherence within f-2f Interferometry

One of the most important properties of laser radiation is the presence of strong coherence that decisively sets lasers apart from other light sources. The main idea of coherence is to classify the mutual relation between electric fields, or more precisely the phase relationship within one or multiple electric oscillations. Here, the discussion is limited to linearly polarized light. Fundamentally, two different approaches can be made to the concept of coherence. On the one hand, the temporal evolution of multiple waves and their phase relationship can be compared, which is referred to as temporal coherence and can be experimentally observed, e.g., in a Michelson interferometer. On the other hand, spatial coherence correlates the phase relationship of two waves of different origin at a specific position. A typical experiment to observe spatial coherence is Young's double-slit experiment, where two sources lead to interference at a specific point. Traditionally, coherence is defined by a correlation function

$$\Gamma(\boldsymbol{r},\Delta t) = \frac{\int E(\boldsymbol{r},t)E^*(\boldsymbol{r},t+\Delta t)dt}{\int E(\boldsymbol{r},t)E^*(\boldsymbol{r},t)dt}, \tag{3.2}$$

where $E(\boldsymbol{r},t) = E_0 \exp(i[\omega(t-\boldsymbol{r}/c)+\varphi(t)])$ represents the complex electric field at position $\boldsymbol{r}$ at time t, with temporal delay Δt and phase $\varphi(t)$. For delays in the order of the pulse duration, an intra-pulse coherence function is observed that is identical to an ideal bandwidth-limited pulse shape, which can be shorter than the real pulse duration. This is a common phenomenon in pulse characterization, where the measured coherence function has been mistakenly interpreted as the effective pulse shape. Typically referred to as the coherent artifact, it results in a severe underestimation of the pulse duration [235, 236]. Contrary to intra-pulse coherence, the phase relationship between successive pulses of the same origin is termed inter-pulse coherence.

This phase relationship can be expressed by the modulus of the complex degree of first-order coherence [137, 237, 238]

$$|g_{12}^{(1)}(\lambda,t_1-t_2)| = \left| \frac{\langle \tilde{E}_i(\lambda,t_1)\tilde{E}_j^*(\lambda,t_2)\rangle_{i\neq j}}{\left[\langle|\tilde{E}_i(\lambda,t_1)|^2\rangle\langle|\tilde{E}_j(\lambda,t_2)|^2\rangle\right]^{1/2}} \right|, \tag{3.3}$$

where angular brackets indicate an ensemble average over independently ($i \neq j$) generated pairs. Eq. 3.3 can be reduced to the case of zero delay $t_1 - t_2 = 0$ to give the fringe visibility $V = V_0|g_{12}^{(1)}|$ with $V_0 = 2(I_1I_2)^{1/2}/(I_1+I_2)$, where I_1 and I_2 are the intensities of both interfering components. For example in Young's double slit experiment with zero path difference it can range from 0, indicating complete incoherence, to 1, which refers to perfect coherence and fringe visibility.

Of major importance is also the coherence length l_c, which relates to a reduction of the fringe visibility by $1/e$ in interferometer experiments. While incandescent light sources only have a micrometer long coherence length, e.g., single-longitudinal mode HeNe lasers allow a delay of well above several hundred meters. The coherence length is proportional to the inverse spectral bandwidth of the single modes of the laser resonator that is limited by Schawlow-Townes noise [128]. This also applies to mode-locked lasers, where the resulting inter-pulse coherence also inversely correlates with the spectral width of a phase-locked individual needle of the frequency comb.

As the transfer of coherence properties during spectral extension is of interest, a deeper picture into earlier investigations into this topic is given in the next section.

3.4.1 Coherence During Supercontinuum Generation

In the discussion in section 3.3.5 it was suggested that the seen fringe degradation might be a loss of intra-pulse coherence caused by the SCG process. The effect of spectral broadening on coherence has been analyzed before. In those investigations filamentation has been found to maintain strong spatial [239] and temporal coherence [240] of the broadened pulse. Surprisingly, the former is also maintained between different filaments that are a result of modulation instability. High temporal coherence is also maintained, which enables compression close to the bandwidth limit [241]. On the contrary, temporal coherence is found easily diminished in pulses that are spectrally extended within a PCF, which renders subsequent compression troublesome [138]. Further analysis of the coherence properties were conducted by Bellini and Hänsch [234], who interfered two supercontinua that were generated in different positions of a CaF_2 plate with zero delay. This resulted in stable fringes, which indicates strong inter-pulse coherence. In this sense, the coherence transfer function of the generated supercontinuum maintains a high degree of mutual coherence and enables assessment of shot-to-shot phase stability. In contrast to the traditional experiments carried out by Michelson and Young, this direct transfer of coherence properties during the highly nonlinear supercontinuum process was not expected, but additionally confirmed in a collinear generation of time-delayed SC pulses by Corsi et al. [242].

In the context of CEP measurements, however, Equation 3.3 falls short of describing the coherence evolution of the phase transfer process within f-$2f$ interferometry. In order to determine this transfer it is necessary to include the correlation within the spectrum of each individual pulse and the subsequent frequency-doubling step. Hence, a new coherence transfer function is established in the upcoming section, that enables to assess the intra-pulse coherence evolution in f-$2f$ interferometry. Once the transfer function is established, the coherence evolution is analyzed as a function of the spectral broadening process. It can be expected that a connection between coherence preservation and the mechanisms that rule spectral extension exists. Then, the effect of coherence degradation during the extraction of the CEP as well as on the phase relationship of the newly generated frequencies is discussed. The results are put into perspective to the experiments carried out earlier in this chapter as well as its implications for spectral broadening in general.

3.4.2 Coherent Phase Transfer in f-$2f$ Interferometry

The evolution of the phase transfer within f-$2f$ interferometry is assessed in a general context that focuses on the dominating spectral broadening mechanism. To this end, a suitable coherence function is established that describes the phase evolution in f-$2f$ interferometry by

$$\Gamma^{\mathrm{CEP}} = \frac{|\langle \tilde{E}_i^2(2\lambda)\tilde{E}_i^*(\lambda)\rangle|}{\langle|\tilde{E}_i^2(2\lambda)\tilde{E}_i^*(\lambda)|\rangle}, \tag{3.4}$$

where $\tilde{E}_i^2(2\lambda)$ and $\tilde{E}_i(\lambda)$ represents the electric field of the second harmonic and fundamental, respectively. The coherence function Γ^{CEP} assesses the correlation within the spectrum of the i-th pulse of an ensemble of pulses. As a subsequent frequency-doubling step is involved in spectral interferometry, the electric field needs to be squared to fully describe the phase transfer.

The denominator of $|\Gamma^{\mathrm{CEP}}|$ associates with the strength of the figure-of-merit (FOM) [12] in f-$2f$

interferometry, given by

$$\mathrm{FOM}_{(\mathrm{CEP})} = \frac{\tilde{E}_{\mathrm{fu}}\tilde{E}_{\mathrm{sh}}}{\tilde{E}_{\mathrm{fu}} + \tilde{E}_{\mathrm{sh}}}, \tag{3.5}$$

where $\tilde{E}_{\mathrm{fu}}$ and $\tilde{E}_{\mathrm{sh}} = d_{\mathrm{eff}}E^2_{(2\cdot\mathrm{fu})}$ represent the spectral density at the fundamental and second harmonic wavelength, respectively. Here, d_{eff} refers to the SH conversion efficiency. In the previous section 3.2, the main concern was to increase the FOM, i.e., to maximize the photon count at the back-end of the detection and either strengthen the beat signal or fringe visibility and hence, minimize the influence of shot noise.

However, one important aspect of this coherence transfer function Eq. 3.4 is not found in the denominator, but in its phase. More precisely, the phase difference $\Delta\varphi_i$ between the octave-separated parts of the continua, i.e.,

$$\Delta\varphi_i = \arg\left(\tilde{E}_i^2(2\lambda)\tilde{E}_i^*(\lambda)\right) = 2\varphi_i^{(2\lambda)} - \varphi_i^{(\lambda)}, \tag{3.6}$$

where φ_i represents the unwrapped phase of the electric field $\tilde{E}$ within one pulse i formed by the supercontinuum at both wavelengths, where a continuous function of φ_i in λ is assumed. As heterodyne methods do not allow access to the absolute phase, ensemble averaging over equation 3.6 leads to a constant offset [243]. Additional information is actually available within the ensemble spread,

$$\sigma_\varphi = \sqrt{\langle(\Delta\varphi_i - \langle\Delta\varphi_i\rangle)^2\rangle}, \tag{3.7}$$

that enables to evaluate the effect of noise during the supercontinuum generation on the coherence of the carrier-envelope phase and the shot-to-shot stability. To this end, Eq. 1.56 relates the additional phase noise during detection via spectral interferometry to the moving of the fringe and hence the reduced precision of the CEP detection. The phase transfer description is applied to three different approaches that describe spectral broadening in various media in the following part.

SPM-dominated Spectral Broadening

SPM-induced spectral broadening is of special relevance in the case of nanojoule oscillator CEP detection that employs fibers. In order to evaluate the loss of coherence, the accumulation of the nonlinear phase, as described in section 1.2.1, is numerically simulated by modulating the spectral phase of a 10 fs long pulse (FWHM). While this leads to a supercontinuum that is symmetric around the pump frequency of 775 nm as can be seen in Figure 1.2 b), an octave-spanning spectrum is only achieved after strong modulation. Connecting numerical simulation of self-phase modulation to the phase evolution within the SC reveals interesting characteristics and is shown in Fig. 3.19 a) and d). While the FOM continuously rises with increased input energy until a maximum is reached, a further growth in intensity and hence accumulated nonlinear phase actually reduces the FOM. This indicates that a further increase in intensity might be of disadvantage under the chosen conditions, which include frequency-doubling from 1064 nm to 532 nm. In this case, the maximum FOM is reached at 8 rad accumulated nonlinear phase. Amplitude fluctuations of the generated continuum at the f and $2f$ components are provided by the standard deviation of the FOM (green), which are at a minimum at this point. Furthermore, the found ensemble spread leads to rather low phase fluctuations of about 50 mrad (see Fig. 3.19 d)) at the maximum FOM. The SPM-

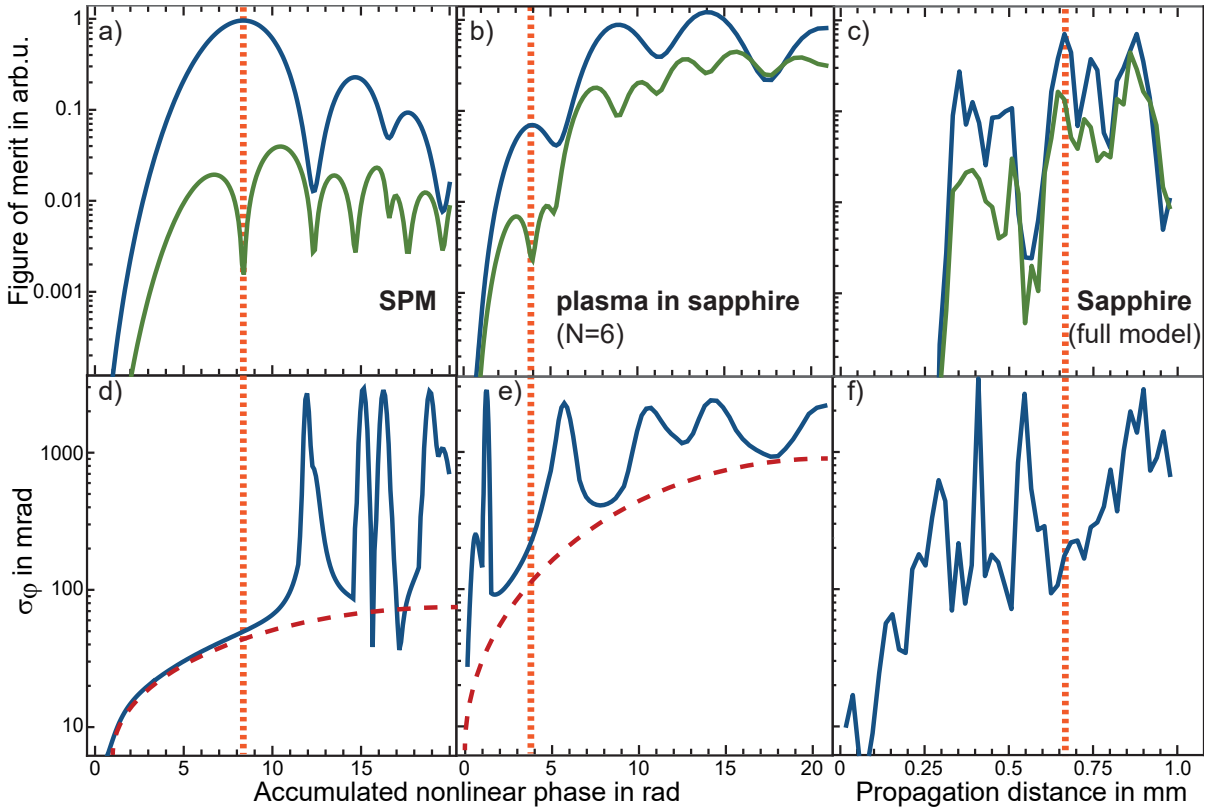

Figure 3.19: (a-c) Simulated mean (blue) and standard deviation (green) of the FOM. (d-g) Phase fluctuations in rad according to Eq. 3.7. While a) and d) show the results for SPM-dominated broadening, b) and e) give the results of plasma-dominated broadening with a 6th-order coefficient representing sapphire. c) and f) provide the findings of the Full (2D+1) model for sapphire. Pulse durations and input fluctuations are set to 10 fs and 1%, respectively.

dominated broadening process shows spikes in the phase jitter σ_φ at some local extrema of the FOM that can readily amount to over 1 rad.

With increasing pulse width, the need for higher modulation to achieve similar broadening is evidently following equation 1.27 and hence, with increasing pulse length, the FOM actually requires more and more SPM to achieve similar maxima. This results in a slightly increased phase noise floor with longer pulse lengths until a pulse duration of roughly 80 fs. From there, the phase noise substantially drops beginning at low accumulated nonlinear phases. As can be expected for a nonlinear process, intensity seed input fluctuations that readily exceed 1 % introduce much more phase decoherence, where, e.g., 5 % input fluctuations lead to a noise floor, such as the one indicated as a red dashed line in Figure 3.19, that is about five times higher. Besides the noise floor, seed intensity variations affect the phase fluctuations, too. For example, while already 0.1 % input intensity fluctuations renders phase coherence within the single milliradian regime, occasional excursions with increased accumulated nonlinear phase can exceed 1 rad. Furthermore, when seed intensity fluctuations of about 10 % are present, phase noise of less than 300 mrad is only achieved for small values of accumulated nonlinear phase. Hence, strong intensity fluctuations of the input pulses limit the accumulated nonlinear phase window where additional noise is minimized during CEP detection that employ an SPM-driven spectral extension approach.

Multi-photon Ionization Enhanced Spectral Broadening

The situation changes drastically if multi-photon excitation is considered. Plasma-dominated spectral broadening holds the optical shock that is caused by the space-time focusing and self-steepening, which is not taken into consideration here. Close to the peak of the pulse, the abrupt formation of the plasma effectively lowers the nonlinear refractive index. In combination with self-steepening, this gives rise to an abrupt change in the phase, resulting in the formation of a pedestal into the bluish region, and hence strong asymmetric broadening as can be seen in Figure 1.2 a). The Keldysh theory is combined with the Drude theory [59] as explained in section 1.2.2 to describe the multi-photon ionization dynamics. A sixth-order absorption coefficient is used, which simulates the need to absorb six photons as is the case for sapphire. Thus, with the same parameters as for the SPM scenario, the highest FOM is observed for an accumulated nonlinear phase of roughly 14 rad. As this would imply a CEP jitter of at least π, a better choice of input parameters is rather at a side maximum of the FOM at around 4 rad, where the phase is found to be fluctuating by about 200 mrad. In sharp contrast to SPM-dominated broadening, the additional contribution by the plasma leads to a quantitative four times increase in the observed phase fluctuations. In additional simulations, where the number of needed photons to bridge an increasing band gap material from four to eleven photons is simulated, a rise of phase uncertainty by increasing the lower limit noise floor (red dashed line) is seen. A similar behavior to SPM-dominated spectral broadening emerged when pulse length is considered. For increasing pulse durations the phase jitter grows, while at pulse durations of around 80 fs the induced phase uncertainty begins for small accumulated nonlinear phases to almost vanish. Comparable behavior to SPM-dominated broadening is also seen in terms of input intensity fluctuations, where the phase noise floor is raised with stronger fluctuations. As both, SPM- and MPI-dominated spectral broadening do not comprehensively describe the SCG process, the nonlinear envelope equation is used in the upcoming part to verify the found connection.

Full Unidirectional (2D+1) Model in Sapphire

Each of the earlier presented models focuses on only one dominating mechanism of spectral extension. Therefore, the analysis is extended to include a full unidirectional (2D+1)-model that employs the nonlinear envelope equation 1.38, which was earlier introduced in section 1.2.3. The analysis was conducted in collaboration with Dr. Carsten Brée [56] and includes the numerical simulation of SPM, plasma generation, self-steepening as well as spatial and dispersive effects in a 2 mm thick sapphire plate. The plasma contribution is implemented via PPT theory. The numerical investigation includes a large ensemble of input pulses with 1 % fluctuation. The results are presented in Figure 3.19 c) and f). Here, the propagation distance can be directly given instead of the accumulated nonlinear phase. The highest FOM is found for about 0.7 mm propagation, resulting in the strongest heterodyne signal between 532 nm and 1064 nm. At this point the signal shows strong amplitude fluctuations of roughly 20 % in combination with phase fluctuations of 150 mrad, which is comparable to pure MPI-dominated spectral broadening. Deviation from the point, where the FOM is maximized, may readily lead to phase fluctuations that are double as strong. The comprehensive treatment of the SC process confirms earlier results that an intra-pulse decoherence effect between the edges of the supercontinuum constrains the achievable precision of the CEP measurement and hence the overall stabilization.

Coherence Degradation under Experimental Conditions

The limited performance of the stabilization shown in section 3.3 resulted in roughly 185 mrad residual CEP jitter. Therefore, it is of interest to evaluate the effect of intra-pulse coherence loss under those experimental conditions. To this end, both extreme cases of spectral broadening mechanisms, namely SPM-dominated and multi-photon ionization ruled spectral extension are simulated. To obtain the highest FOM the pulse is assumed to be slightly positively chirped from its measurement limit of 35 fs to an estimated 60 fs. Additionally, in order to maximize the FOM, it has been observed before that the critical power scales quadratically with the chirp [244, 245] and thus, a chirp can also enable increased spectral density. The chirp has been adapted here by adjusting the acousto-optic programmable dispersive filter within the amplifier. With the measured incident fluctuation accumulating to 2.3 %, the resulting effect on the intra-pulse coherence for both cases, MPI-dominated and SPM-dominated spectral broadening in sapphire can be seen in Figure 3.20 for frequency-doubling from 1020 nm to 510 nm. With only a slightly accumulated nonlinear phase of several radian, a range between 70 to 200 mrad shot-to-shot phase jitter for pure SPM and plasma-induced phase fluctuations can be seen, respectively. Hence, shot-to-shot fluctuations that amount up to 200 mrad, as was seen in this work, can be readily explained by a degradation of the coherence during spectral broadening. Nevertheless, this also shows that despite relatively strong seed fluctuations of 2.3 %, reasonable results are still possible.

3.4.3 Discussion

The above analysis comprises of three different approaches to describe spectral extension and its implications for the intra-pulse coherence of the spectrally extended incident pulse. In this sense, introduced phase uncertainties in the presence of input fluctuations between two spectral densities separated by an octave and subsequent frequency-doubling have been evaluated. While in the SPM-dominated broadening case the nonlinear phase modulation is directly proportional to intensity fluctuations, in a plasma-

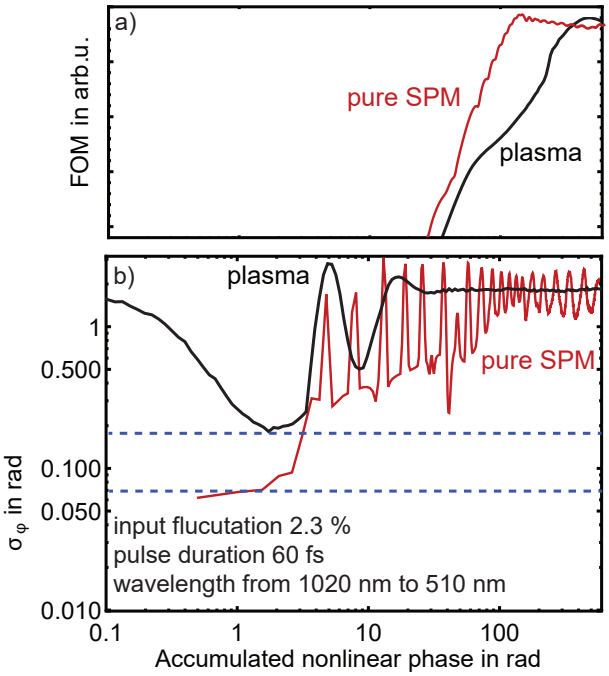

Figure 3.20: Simulation of SPM- and plasma-dominated broadening for the experimental conditions used within this work, where the seed intensity fluctuated by 2.3 %, while the frequency-doubling was carried out from 1020 nm to 510 nm. Sapphire parameters were used for simulating the multi-photon absorption. a) shows the FOM, while in b) the induced phase fluctuations are given.

dominated scenario as it is present during filamentation in dielectric media, the process of multi-photon absorption follows $\propto I^K$, i.e., it is highly nonlinear, and depends on the number of photons that have to be absorbed to overcome the band gap. In the latter, the position within the media, where plasma defocussing stops spatio-temporal shock formation is therefore fluctuating on a pulse-to-pulse basis with varying seed intensity. These seed fluctuations lead than to an increased ensemble spread σ_φ that is particularly strong for plasma-driven broadening. This idea is also confirmed in the simulation of the SCG by the nonlinear envelope equation. Hence, the plasma-dominated extension is therefore more influenced by seed fluctuations as the SPM-dominated broadening. This suggests that media with smaller band gap seem to be less drastically affected by input fluctuations in general. Then, their critical power is also minimized and hence, spectral densities are limited, too. Therefore, a trade-off between the highest achievable FOM and the smallest loss of intra-pulse coherence seems to be required. Nevertheless, as even the full treatment employing the NEE for sapphire shows, a mixture of both scenarios exists in reality. This is also confirmed by the SPM and MPI treatment under the experimental conditions present in this work, where the range in between both scenarios has been found to match the region of residual jitters.

The loss of intra-pulse coherence could therefore be explained by the supercontinuum process itself and the onset of filamentation in relation to the optical shock formation. Hence, it should be beneficial for measuring the CEP to avoid excess plasma-dominated supercontinuum generation. While plasma generation and filamentation typically go hand in hand with asymmetric broadening, one may conclude to favor symmetric broadening instead. Nevertheless, at some intensities, especially close to extrema of the FOM, excessive noise well above 1 rad on a shot-to-shot basis can be seen even for the SPM-based spectral broadening. A similar trend has been seen by Wang et al. [231], where SPM dominated

broadening in a hollow-core fiber was observed to introduce a lower dependence of 128 mrad/1% energy change compared to the results obtained by Li et al. [25] with 160 mrad/1% energy change, the latter measured for plasma-dominated filamentation in sapphire.

Interestingly, as inter-pulse coherence has been found to be strongly deteriorated by SCG in PCFs where SPM-based broadening dominates, a loss of intra-pulse coherence is most certainly not present as precise measurement of the CEP can readily be achieved with residual jitters of only several ten mrad for oscillators [12]. To the contrary, inter-pulse coherence is only weakly affected by the filamentation process, which is supported by ensemble averaging over Equation 3.3. Nevertheless, intra-pulse coherence is degraded early on. Hence, while compression to Fourier-limited pulses is possible after filamentation-based broadening, the loss of intra-pulse coherence renders phase-sensitive measurements easily compromised. Both types of coherence certainly show similar trends, e.g., being sensitive to incident pulse length and fluctuations.

To conclude, the findings describe very well the situation in most CEP detection schemes relying especially on filamentation, where single-shot results have been seen to easily exceed 100 mrad despite well-performing oscillators. Therefore, spectral extension seems favorable when relying on SPM considering the degradation of intra-pulse coherence, while MPI-dominated spectral broadening should consider a trade-off between maximizing spectral densities and the loss of intra-pulse coherence by choosing a media with appropriate band gap.

3.5 Conclusion on Fundamental Limitations during Detection

Contrary to expectations, the reduction of the shot noise influence to a negligible extent revealed that a far more dominating noise source during detection is present. This source hinders precise single-shot CEP extraction and ultimately constraints achievable shot-to-shot jitters during stabilization. Indications for this noise source are observed by strong fringe contrast variations for different measurement schemes as well as $1/f$ noise suspected to be originating from technical noise within the kHz amplifier system. These findings point to a connection between the medium employed for spectral extension and a loss of the phase relationship within the SC. The quality of the phase relationship within extended spectra and subsequent phase transfer during second-harmonic generation is termed intra-pulse coherence. Its degradation can explain the loss of fringe contrast as well as performance constraints seen in active as well as passive CEP stabilization schemes.

Simulations assessing the phase evolution during supercontinuum generation revealed to favor symmetric SPM-dominated extension over plasma-driven filamentation as the latter suffers from strong asymmetric broadening that leads to an increased uncertainty within the phase of the extended supercontinuum. It can be assumed that the uncertainty in phase between successive pulses grows nonlinearly the further the continuum is extended relative to the seed frequency. This suggests to favor symmetric instead of asymmetric broadening. In the presented experiments relying on filamentation, the most symmetric spectral extension is seen in sapphire, while the strongest asymmetric situation is found by employing xenon at 8 bar. The latter exhibits the generation of local depressions and as a result refractive index variations. In order to beat capping critical power and increase spectral densities within filamentation-dominated broadening, lower nonlinearities and hence increased band gaps are needed. This has been realized in the first part of this chapter, where the FOM has been maximized. However, maximizing the FOM at the back-end of the detection and thereby enlarging photon numbers that form a fringe has not been completely beneficial. When employing media with larger band gaps, a reduction in the extraction precision of the CEP probably caused by intra-pulse coherence degradation is observed. This can be understood if the position within the media is considered, where the Kerr nonlinearity-induced self-focusing is halted by plasma generation. With the band gap determining the order of the ionization rate at constant photon energy, the presence of intensity fluctuations may very well translate into position variations where the balance between the self-focusing and plasma defocussing is met. This leads to additional uncertainty from shot-to-shot, which also changes the spectral characteristics of the resulting supercontinuum. Further, decreasing n_2 translates into extended asymmetric broadening, as can be seen between sapphire and CaF_2. Hence, instead of simply maximizing the photon numbers by using media with higher band gaps, a trade-off between band gap and hence n_2 as well as a loss of intra-pulse coherence needs to be considered. Additionally, it is seen that the compressibility or inter-pulse coherence is not necessarily affected, enabling compression close to the Fourier limit, while the intra-pulse coherence is reduced. Vice versa, the opposite situation is observed routinely in fibers, where the inter-pulse coherence degradation inhibits nearly perfect compression, while precise measurement of the CEP is routinely carried out within CEP detection of oscillator pulses.

The presented findings not only affect the supercontinuum generation in f-$2f$ interferometry, but may also explain the high residual CEP jitters found in passive stabilization schemes [20]. With common OPA systems relying on spectral broadening prior to optical parametric amplification and subse-

quent passive stabilization in a difference-frequency generation (DFG) setup [246], the presented results may explain why shot-to-shot fluctuations of the carrier-envelope phase in such schemes occasionally reach up to 1 rad, while typical average jitters are still around 200 mrad. Nevertheless, alternatives to filamentation-ruled SCG can be found by using stereo above threshold ionization (stereo-ATI) [243] or combining passive and active stabilization, the latter realized by frequency-doubling prior to supercontinuum generation in combination with an additional 10 kHz bandwidth active stabilization [22].

Overall, intra-pulse coherence degradation can not only explain the observed performance limitations in this thesis, but also sheds light on a broader range of CEP-stabilized lasers that rely on spectral extension for CEP detection. These findings thus enable to give instructive guidance for further developments of CEP stabilization and allow to assess the suitability of an employed spectral broadening media in terms of its introduced intra-pulse coherence degradation.

Conclusion and Outlook

In this thesis two different sources of CEP noise were identified that can strongly interfere with the CEP stabilization of ultra-short laser pulses. While one source is detrimentally affecting the precision of the CEP detection in the most common CEP stabilization schemes, the other is hindering the stabilization of one particular type of Er:doped fiber lasers. In the first part of this thesis novel methodologies, namely time-resolved Kendall-τ correlation analysis and the identification of the time-resolved statistical noise properties are used to support the identification of a strong noise source in the Er:doped fiber laser. It is concluded that the observed broadband CEP noise is a result of intra-cavity amplitude-to-phase coupling within a semiconductor saturable absorber mirror (SESAM) that is operated too close or exactly at an excitonic resonance. This coupling leads to a strong transfer of intra-cavity amplitude fluctuations resulting from, e.g., amplified spontaneous emission, to phase noise and hence broadband CEP noise that exceeds the laser response bandwidth.

In the second part of this thesis, the noise added during the detection of the CEP of amplified laser pulses is investigated. It is concluded that the high levels of CEP noise observed in typical amplifier stabilization schemes are not a result of a low number of detected photons that would lead to shot noise, as was originally believed. Instead, the experiments and analysis carried out lead to the conclusion that amplitude-to-phase coupling during spectral broadening induces substantial noise. This CEP noise is a result of intensity fluctuations of the seed pulse that originates from fundamental sources such as, e.g., amplified spontaneous emission. Then, these fluctuations couple to phase noise during supercontinuum generation. As a result of this coupling the phase relationship between different spectral components of the extended spectrum is detrimentally affected, which is described here as a loss of intra-pulse coherence.

Numerical analysis of the intra-pulse coherence degradation under different spectral broadening conditions has revealed that asymmetric broadening induced by plasma-dominated processes, such as the ones occurring during filamentation, lead to a much stronger degradation of the intra-pulse coherence as compared to SPM-driven symmetric extension of the spectrum. This is in accordance with the general experimental observation, where oscillator CEP detection employing SPM or soliton fission for spectral extension in a fiber show substantially lower noise levels and hence higher CEP stability of the source as compared to amplifier CEP detection that typically relies on filamentation in dielectric media. The strong loss of intra-pulse coherence during filamentation is also in sharp contrast to the typically unaffected inter-pulse coherence, the latter describing the compressibility of pulses to the Fourier-transform

limit. While the inter-pulse coherence is commonly observed to degrade when employing fibers for spectral extension, intra-pulse coherence seems to be only marginally affected under most conditions.

The numerical simulations also show that maximizing the number of photons during spectral broadening to achieve the strongest measurement signal may lead to a strong loss of intra-pulse coherence in combination with strong amplitude fluctuations at the edges of the generated broadband spectrum. Hence, a trade-off between maximizing photon numbers and the corresponding intra-pulse coherence degradation needs to be ensured for optimizing measurement precision. This statement is confirmed by the presented comparative analysis of CEP detection schemes that relies on various media for filamentation-based spectral broadening and where the photon numbers are maximized to avoid shot noise influence. In those cases, the measured CEP stability performances is observed to be restricted above 170 mrad, which is in accordance with the estimated noise resulting from a loss of intra-pulse coherence.

Overall, the concept of intra-pulse coherence not only explains the difference in CEP stabilization performance of ultra-short laser pulses from oscillators and amplifiers, but also provides an explanation for the strong CEP noise observed in passive stabilization schemes such as CEP-stable OPCPA systems. In those systems, residual jitters have been seen to exceed 200 mrad, which can be explained by the use of dielectric media (and hence filamentation) for spectral extension that enables deriving the seed pulse from the pump pulses. The intra-pulse coherence loss in the filamentation process may lead to shot-to-shot fluctuations of the passively-stabilized CEP of the resulting idler.

Applications that rely on a stable carrier-envelope offset (CEO) frequency, such as frequency metrology, may also experience limitations caused by intra-pulse coherence degradation. In this field, the measurement and stabilization of the CEO frequency relies also on f-$2f$ interferometry and hence requires spectral broadening. Under certain conditions, the presented numerical simulations show that the phase excursions can exceed π even for SPM-driven spectral broadening. As a consequence the proper identification of the frequency of the comb needle is spoiled.

To conclude, the concept of intra-pulse coherence introduced in this thesis can be used to judge the suitability of a supercontinuum source for the desired application and is a helpful extension to the concept of inter-pulse coherence when the phases are compared within one pulse. From the presented conclusions, the following recommendations can be made. Avoiding strong asymmetric plasma-driven spectral broadening during CEP detection should lead to an overall reduction of white CEP noise and thereby ensure lower CEP jitters during stabilization. Furthermore, using the concept of intra-pulse coherence to assess the necessary thickness of the supercontinuum medium and thereby adjust the amount of accumulated nonlinear phase may enable finding an optimum compromise between maximizing photons and ensuring the preservation of intra-pulse coherence. In general, minimizing intensity fluctuations of the seed pulse as well as considering alternatives to f-$2f$ interferometry for CEP detection to avoid spectral broadening such as, e.g., measurement methods that employ above-threshold ionization, are ways to ensure further reduction of the impact of the CEP detection on the stabilization performance.

In the future, evaluation of the intra-pulse coherence degradation for the soliton fission process should help to assess the situation when spectral broadening is carried out in fibers. Furthermore, the methodologies presented in the first part of the thesis should be applied to a wider range of lasers such as, e.g., thin disk lasers, which may reveal more details on intra-cavity and extra-cavity CEP noise sources. Together, the presented conclusions and recommendations may enable routine stabilization of amplified systems and other laser sources such as CEP-stable OPCPA systems with jitters well below 100 mrad.

Publications

Journals

1. N. Raabe, T. Feng, T. Witting, A. Demircan, C. Brée, and G. Steinmeyer. Role of intrapulse coherence in carrier-envelope phase stabilization, *Phys. Rev. Lett.*, 119(12):3901, 2017.

2. N. Raabe, T. Feng, M. Mero, H. Tian, Y. Song, W. Hänsel, R. Holzwarth, A. Sell, A. Zach, and G. Steinmeyer. Excess carrier-envelope phase noise generation in saturable absorbers. *Opt. Lett.*, 42(6):1068-1071, 2017.

3. T. Feng, N. Raabe, P. Rustige, and G. Steinmeyer. Electric-field induced second-harmonic generation of femtosecond pulses in atmospheric air. *Appl. Phys. Lett.*, 112, 241101, 2018.

4. H. Tian, N. Raabe, Y. Song, M. Hu and G. Steinmeyer. High-detectivity optical heterodyne method for wideband carrier-envelope phase noise analysis of laser oscillators. *Opt. Lett.*, 43(13):3108-3111, 2018.

5. C. Zhang, T. Feng, N. Raabe and, H. Rottke. Strong-field ionization of the xenon dimer: The effect of two-equivalent-centers interference and of driving ionic transitions. *Phys. Rev. A*, 97.2: 023417, 2018.

6. T. Feng, P. Rustige, N. Raabe, and G. Steinmeyer. Intracavity measurement of the electro-optic Kerr effect via carrier-envelope phase demodulation. *Opt. Lett.*,41(22):5158-5161, 2016.

Proceedings

1. N. Raabe, T. Feng, M. Mero, H. Tian, Y. Song, W. Hänsel, R. Holzwarth, A. Sell, A. Zach, and G. Steinmeyer. Hidden amplitude-phase correlations in the carrier-envelope noise of mode-locked lasers. *Proc. SPIE 10089, Real-time Measurements, Rogue Phenomena, and Single-Shot Applications II, 1008907*, 2017.

2. J. Hyyti, N. Raabe, and G. Steinmeyer. Characterization of Ultrashort Laser Pulses and Carrier-Envelope Phase Stabilization. *Proceedings of Enrico Fermi Summer School*, 2015.

Oral conference contributions

1. N. Raabe, T. Feng, T. Witting, A. Demircan, C. Brée, and G. Steinmeyer*. Intrapulse Coherence for Gauging the Quality of Passive Carrier-Envelope Phase Stabilization. *CLEO*, paper STh4N.7, 2018.

2. T. Feng*, N. Raabe, P. Rustige, and G. Steinmeyer. Electric-field induced second-harmonic generation of femtosecond laser pulses in atmospheric air. *CLEO*, paper SW4N.1, 2018.

3. N. Raabe, T. Feng*, T. Witting, A. Demircan, C. Brée, and G. Steinmeyer. Role of intrapulse coherence in carrier-envelope phase stabilization. *HILAS*, paper HW3D.4, 2018.

4. T. Feng*, N. Raabe, P. Rustige, and G. Steinmeyer. Electric-field induced second-harmonic generation in atmospheric air with quasi-phase matching. *HILAS*, paper HW3D.6, 2018.

5. G. Steinmeyer*, N. Raabe, A. Demircan, C. Brée. The role of intrapulse coherence in supercontinuum generation. *SPIE LASE*, Paper 10517-15, 2018.

6. N. Raabe, T. Feng, T. Witting, A. Demircan, C. Brée, and G. Steinmeyer*. Intrapulse coherence as a limiting factor in interferometric carrier-envelope phase measurements. *UFO XI*, 2017.

7. N. Raabe, T. Feng, M. Mero, H. Tian, Y. Song, W. Haensel, R. Holzwarth, A. Sell, A. Zach, and G. Steinmeyer*. Hidden correlation in the CEP noise of mode-locked lasers. *CLEO Europe*, 2017.

8. T. Feng*, P. Rustige, N. Raabe, and G. Steinmeyer. Electro-optic Kerr effect measurement based on carrier-envelope phase demodulation. *CLEO Europe*, 2017.

9. H. Tian*, N. Raabe, Y. Song, G. Steinmeyer, H. Minglie. Bootstrap method for ultrabroad bandwidth carrier-envelope frequency noise analysis with superior detectivity. *CLEO*, 2017.

10. T. Feng, N. Raabe, P. Rustige, and G. Steinmeyer*. Highly sensitive measurement of the optical Kerr effect in air. *32nd URSI Gass*, 2017.

11. T. Feng*, N. Raabe, P. Rustige, and G. Steinmeyer. Intracavity hyperpolarizability measurement from carrier envelope phase demodulation. *CLEO*, 2016.

12. N. Raabe, M. Mero, Y. Song, W. Haensel, R. Holzwarth, A. Sell, A. Zach, and G. Steinmeyer*. Detecting determinism in laser noise: a novel diagnostic approach for ultrafast lasers. *CLEO*, 2016.

13. N. Raabe*, S. Birkholz, M. Mero, Y. Song, F. Bach, and G. Steinmeyer. Time Series Analysis of Mode-locked Oscillator CEP Noise. *CLEO Europe*, 2015.

14. M. Mero*, N. Raabe, and G. Steinmeyer. Long-term, real-time correction of carrier-envelope phase fluctuations. *CLEO Europe*, 2015.

Posters

1. N. Raabe, S. Birkholz, M.Mero, H. Tian, Y. Song, and G. Steinmeyer. Nonlinear Time Series Analysis of Mode-locked Oscillator CEP Noise. *Tampere Summer School*, 2015.

2. N. Raabe, X. Chen, J.F. Hergott, O. Tcherbakoff, P.M. Paul, and G. Steinmeyer. Optimizing Quantum Limitations in CEP Stabilization of Amplified Laser Systems. *Enrico Fermi Summer School*, 2014.

Acronyms

ADK Ammosov, Delone and Krainov.

AM amplitude modulation.

AOFS acousto-optic frequency shifter.

AOM acousto-optic modulator.

AOPDF acousto-optic programmable dispersive filter.

ASE amplified spontaneous emission.

ATI above-threshold ionization.

CE carrier-envelope.

CEF carrier-envelope frequency.

CEP carrier-envelope phase.

CPA chirped-pulse amplification.

DET CCD detector.

DFG difference-frequency generation.

DOG double-optical gating.

EDF erbium-doped fiber.

FME forward Maxwell equation.

FND frequency noise density.

FOM figure-of-merit.

FWHM full width at half maximum.

GPO group-phase offset.

GVD group-velocity dispersion.

HHG high-order harmonic generation.

IAP isolated attosecond pulses.

IPN integrated phase noise.

LIDAR light detection and ranging.

MPA multi-photon absorption.

MPI multi-photon ionization.

NALM nonlinear amplifier mirror.

NEE nonlinear envelope equation.

NEP noise-equivalent power.

NOLM nonlinear optical loop mirror.

NPR nonlinear polarization rotation.

OPCPA optical parametric chirped-pulse amplification.

PCF photonic crystal fibers.

PG polarization gating.

PID proportional-integral-differential.

PLL phase-locked loop.

PM phase modulation.

PMT photo-multiplier tube.

POL polarizer.

PPLN periodic-poled lithium niobate.

PPT Perelomov, Popov and Terent'ev.

PSD power spectral density.

RBW resolution bandwidth.

SA saturable absorber.

SAM self-amplitude modulation.

SC supercontinuum.

SCG supercontinuum generation.

SESAM semiconductor saturable absorber mirror.

SFA strong-field approximation.

SH second harmonic.

SHG second harmonic generation.

SI spectral interferometry.

SNR signal-to-noise ratio.

SPM self-phase modulation.

SVEA slowly varying envelope approximation.

TOD third-order dispersion.

WDM wavelength-division multiplexing device.

XPM cross-phase modulation.

Bibliography

[1] J. Eckstein. *High resolution spectroscopy using multiple coherent interactions*. PhD thesis, Stanford Univ., CA., 1978.

[2] W. Tomlinson, R. Stolen, and C. Shank. Compression of optical pulses chirped by self-phase modulation in fibers. *JOSA B*, 1(2):139–149, 1984.

[3] J. Fujimoto, A. Weiner, and E. Ippen. Generation and measurement of optical pulses as short as 16 fs. *Appl. Phys. Lett.*, 44(9):832–834, 1984.

[4] N. H. Burnett, H. A. Baldis, M. C. Richardson, and G. D. Enright. Harmonic generation in CO_2 laser target interaction. *Appl. Phys. Lett.*, 31(3):172–174, 1977.

[5] A. Baltuška, M. Uiberacker, E. Goulielmakis, R. Kienberger, V. S. Yakovlev, T. Udem, T. W. Hänsch, and F. Krausz. Phase-controlled amplification of few-cycle laser pulses. *IEEE J. Sel. Top. Quantum Electron.*, 9(4):972–989, 2003.

[6] A. Baltuška, T. Udem, M. Uiberacker, M. Hentschel, E. Goulielmakis, C. Gohle, R. Holzwarth, V. S. Yakovlev, A. Scrinzi, T. W. Hänsch, and F. Krausz. Attosecond control of electronic processes by intense light fields. *Nature*, 421, 2003.

[7] F. Riehle. Optical clock networks. *Nature Photonics*, 11(1):25, 2017.

[8] P. Gill. Is the time right for a redefinition of the second by optical atomic clocks? *Journal of Physics: Conference Series*, 723:012053, 2016.

[9] T. W. Hänsch. Nobel lecture: passion for precision. *Rev. Mod. Phys.*, 78:1297–1309, 4, 2006.

[10] L. Xu, T. W. Hänsch, C. Spielmann, A. Poppe, T. Brabec, and F. Krausz. Route to phase control of ultrashort light pulses. *Opt. Lett.*, 21(24):2008–2010, 1996.

[11] H. R. Telle, G. Steinmeyer, A. E. Dunlop, J. Stenger, D. H. Sutter, and U. Keller. Carrier-envelope offset phase control: a novel concept for absolute optical frequency measurement and ultrashort pulse generation. *Appl. Phys. B Lasers Opt.*, 69(4):327–332, 1999.

[12] B. Borchers, S. Koke, A. Husakou, J. Herrmann, and G. Steinmeyer. Carrier-envelope phase stabilization with sub-10 as residual timing jitter. *Opt. Lett.*, 36(21):4146–4148, 2011.

[13] F. Emaury, A. Diebold, A. Klenner, C. J. Saraceno, S. Schilt, T. Südmeyer, and U. Keller. Frequency comb offset dynamics of SESAM modelocked thin disk lasers. *Opt. Express*, 23(17):21836–21856, 2015.

[14] C. J. Saraceno. Mode-locked thin-disk lasers and their potential application for high-power terahertz generation. *J. Opt.*, 20(4):044010, 2018.

[15] B. E. Schmidt, N. Thiré, M. Boivin, A. Laramée, F. Poitras, G. Lebrun, T. Ozaki, H. Ibrahim, and F. Légaré. Frequency domain optical parametric amplification. *Nature comm.*, 5:3643, 2014.

[16] S. Koke, C. Grebing, B. Manschwetus, and G. Steinmeyer. Fast f-to-2f interferometer for a direct measurement of the carrier-envelope phase drift of ultrashort amplified laser pulses. *Opt. Lett.*, 33(21):2545–2547, 2008.

[17] M. Mero, N. Raabe, and G. Steinmeyer. Long-term, real-time correction of carrier-envelope phase fluctuations. In *CLEO/Europe-IQEC*, CF-4-3. Optical Society of America, 2015.

[18] G. Sansone, E. Benedetti, F. Calegari, C. Vozzi, L. Avaldi, R. Flammini, L. Poletto, P. Villoresi, C. Altucci, R. Velotta, et al. Isolated single-cycle attosecond pulses. *Science*, 314(5798):443–446, 2006.

[19] A. Golinelli, X. Chen, E. Gontier, B. Bussière, O. Tcherbakoff, M. Natile, P. D'Oliveira, P.-M. Paul, and J.-F. Hergott. Original Ti:sa 10 kHz front-end design delivering 17 fs, 170 mrad CEP stabilized pulses up to 5 W. *Opt. Lett.*, 42(12):2326–2329, 2017.

[20] A. Baltuška, T. Fuji, and T. Kobayashi. Controlling the carrier-envelope phase of ultrashort light pulses with optical parametric amplifiers. *Phys. Rev. Lett.*, 88(13):133901, 2002.

[21] T. Gaumnitz, A. Jain, Y. Pertot, M. Huppert, I. Jordan, F. Ardana-Lamas, and H. J. Wörner. Streaking of 43-attosecond soft-x-ray pulses generated by a passively CEP-stable mid-infrared driver. *Opt. Express*, 25(22):27506–27518, 2017.

[22] N. Thiré, R. Maksimenka, B. Kiss, C. Ferchaud, P. Bizouard, E. Cormier, K. Osvay, and N. Forget. 4-W, 100-kHz, few-cycle mid-infrared source with sub-100-mrad carrier-envelope phase noise. *Opt. Express*, 25(2):1505–1514, 2017.

[23] A. Klenner, F. Emaury, C. Schriber, A. Diebold, C. J. Saraceno, S. Schilt, U. Keller, and T. Südmeyer. Phase-stabilization of the carrier-envelope-offset frequency of a sesam modelocked thin disk laser. *Opt. Express*, 21(21):24770–24780, 2013.

[24] B. Borchers, A. Anderson, and G. Steinmeyer. On the role of shot noise in carrier-envelope phase stabilization. *Laser Photonics Rev.*, 8(2):303–315, 2014.

[25] C. Li, E. Moon, H. Wang, H. Mashiko, C. M. Nakamura, J. Tackett, and Z. Chang. Determining the phase-energy coupling coefficient in carrier-envelope phase measurements. *Opt. Lett.*, 32(7):796–798, 2007.

[26] L. Bergé, S. Skupin, R. Nuter, J. Kasparian, and J. P. Wolf. Ultrashort filaments of light in weakly-ionized, optically-transparent media. *Reports Prog. Phys.*, 70(10):1633, 2006.

[27] A. Couairon and L. Bergé. Modeling the filamentation of ultra-short pulses in ionizing media. *Phys. Plasmas*, 7(1):193–209, 2000.

[28] R. W. Boyd. *Nonlinear Optics (Third Edition)*. Academic Press, 2008. ISBN: 978-0-12-369470-6.

[29] T. Brabec and F. Krausz. Nonlinear optical pulse propagation in the single-cycle regime. *Phys. Rev. Lett.*, 78(17):3282–3285, 1997.

[30] M. A. Porras. Propagation of single-cycle pulsed light beams in dispersive media. *Phys. Rev. A*, 60(6):5069–5073, 1999.

[31] P. Kinsler and G. H. C. New. Few-cycle pulse propagation. *Phys. Rev. A*, 67(2):23813, 2003.

[32] F. W. Helbing, G. Steinmeyer, J. Stenger, H. R. Telle, and U. Keller. Carrier-envelope-offset dynamics and stabilization of femtosecond pulses. *Appl. Phys. B Lasers Opt.*, 74(1):35–42, 2002.

[33] H. A. Kramers. *La diffusion de la lumiere par les atomes*. 1927.

[34] R. de L. Kronig. On the theory of dispersion of x-rays. *J. Opt. Soc. Am.*, 12(6):547–557, 1926.

[35] J. Marburger. Self-focusing: theory. *Prog. Quantum Electron.*, 4:35–110, 1975.

[36] Y. R. Shen. Self-focusing: experimental. *Prog. Quantum Electron.*, 4:1–34, 1975.

[37] E. Yablonovitch and N. Bloembergen. Avalanche ionization and the limiting diameter of filaments induced by light pulses in transparent media. *Phys. Rev. Lett.*, 29(14):907–910, 1972.

[38] W. Liu, S. Petit, A. Becker, N. Aközbek, C. Bowden, and S. Chin. Intensity clamping of a femtosecond laser pulse in condensed matter. *Opt. Commun.*, 202(1-3):189–197, 2002.

[39] W. Liu, O. Kosareva, I. S. Golubtsov, A. Iwasaki, A. Becker, V. P. Kandidov, and S. L. Chin. Femtosecond laser pulse filamentation versus optical breakdown in H_2O. *Appl. Phys. B*, 76(3):215–229, 2003.

[40] S. Tzortzakis, L. Sudrie, M. Franco, B. Prade, A. Mysyrowicz, A. Couairon, and L. Bergé. Self-guided propagation of ultrashort IR laser pulses in fused silica. *Phys. Rev. Lett.*, 87(21):213902, 2001.

[41] V. Bespalov and V. Talanov. Filamentary structure of light beams in nonlinear media. *JETP Lett.*, 3:307–310, 1966.

[42] S. Birkholz. *Determinism and predictability in extreme event systems*. PhD thesis, Humboldt-Universität zu Berlin, Mathematisch-Naturwissenschaftliche Fakultät, 2016.

[43] A. J. Campillo, S. L. Shapiro, and B. R. Suydam. Periodic breakup of optical beams due to self-focusing. *Appl. Phys. Lett.*, 23(11):628–630, 1973.

[44] R. H. Stolen and C. Lin. Self-phase-modulation in silica optical fibers. *Phys. Rev. A*, 17(4):1448–1453, 1978.

[45] S. A. Akhmanov, V. A. Vysloukh, and A. S. Chirkin. *Optics of femtosecond laser pulses*. 1992, page 366. ISBN: 978-0-88318-851-4.

[46] A. J. Stentz, M. Kauranen, J. J. Maki, G. P. Agrawal, and R. W. Boyd. Induced focusing and spatial wave breaking from cross-phase modulation in a self-defocusing medium. *Opt. Lett.*, 17(1):19–21, 1992.

[47] M. Bradler. *Bulk continuum generation: the ultimate tool for laser applications and spectroscopy*. PhD thesis, Ludwig-Maximilians-Universität München, 2014.

[48] G. Yang and Y. R. Shen. Spectral broadening of ultrashort pulses in a nonlinear medium. *Opt. Lett.*, 9(11):510–512, 1984.

[49] F. DeMartini, C. H. Townes, T. K. Gustafson, and P. L. Kelley. Self-steepening of light pulses. *Phys. Rev.*, 164(2):312–323, 1967.

[50] A. L. Gaeta. Catastrophic collapse of ultrashort pulses. *Phys. Rev. Lett.*, 84(16):3582–3585, 2000.

[51] A. Brodeur and S. L. Chin. Band-gap dependence of the ultrafast white-light continuum. *Phys. Rev. Lett.*, 80(20):4406–4409, 1998.

[52] A. Brodeur and S. L. Chin. Ultrafast white-light continuum generation and self-focusing in transparent condensed media. *J. Opt. Soc. Am. B*, 16(4):637, 1999.

[53] L. Keldysh. Ionization in the field of a strong electromagnetic wave. *Sov. Phys. JETP*, 20(5):1307–1314, 1965.

[54] D. J. Little, M. Ams, and M. J. Withford. Influence of bandgap and polarization on photoionization: guidelines for ultrafast laser inscription. *Opt. Mater. Express*, 1(4):670–677, 2011.

[55] M. V. Ammosov, N. B. Delone, and V. P. Krainov. Tunnelling ionization of complex atoms and of atomic ions in an alternating electromagnetic field. *J. Exp. Theor. Phys.*, 64(6):1191–1194, 1986.

[56] C. Bree. *Self-compression of intense optical pulses and the filamentary regime of nonlinear optics*. PhD thesis, Humboldt-Universität zu Berlin, Mathematisch-Naturwissenschaftliche Fakultät I, 2011.

[57] Z. Chang. *Fundamentals of Attosecond Optics*. 2011. ISBN: 978-1-4200-8937-0.

[58] S. V. Popruzhenko, V. D. Mur, V. S. Popov, and D. Bauer. Strong field ionization rate for arbitrary laser frequencies. *Phys. Rev. Lett.*, 101(19):193003, 2008.

[59] M. Mero, J. Liu, W. Rudolph, D. Ristau, and K. Starke. Scaling laws of femtosecond laser pulse induced breakdown in oxide films. *Phys. Rev. B*, 71(11):115109, 2005.

[60] J. Jasapara, A. V. V. Nampoothiri, W. Rudolph, D. Ristau, and K. Starke. Femtosecond laser pulse induced breakdown in dielectric thin films. *Phys. Rev. B*, 63(4):45117, 2001.

[61] J. Jasapara, M. Mero, and W. Rudolph. Retrieval of the dielectric function of thin films from femtosecond pump-probe experiments. *Appl. Phys. Lett.*, 80(15):2637–2639, 2002.

[62] N. Bloembergen. The influence of electron plasma formation on superbroadening in light filaments. *Opt. Commun.*, 8(4):285–288, 1973.

[63] W. L. Smith, P. Liu, and N. Bloembergen. Superbroadening in H_2O and D_2O by self-focused picosecond pulses from a YAlG: Nd laser. *Phys. Rev. A*, 15(6):2396, 1977.

[64] P. K. Kennedy, S. A. Boppart, D. X. Hammer, B. A. Rockwell, G. D. Noojin, and W. Roach. A first-order model for computation of laser-induced breakdown thresholds in ocular and aqueous media. ii. comparison to experiment. *IEEE J. Quantum Electron.*, 31(12):2250–2257, 1995.

[65] Q. Feng, J. V. Moloney, A. C. Newell, E. M. Wright, K. Cook, P. K. Kennedy, D. X. Hammer, B. A. Rockwell, and C. R. Thompson. Theory and simulation on the threshold of water breakdown induced by focused ultrashort laser pulses. *IEEE J. Quantum Electron.*, 33(2):127–137, 1997.

[66] B. C. Stuart, M. D. Feit, S. Herman, A. M. Rubenchik, B. W. Shore, and M. D. Perry. Nanosecond-to-femtosecond laser-induced breakdown in dielectrics. *Phys. Rev. B*, 53(4):1749–1761, 1996.

[67] N. Raabe, T. Feng, T. Witting, A. Demircan, C. Brée, and G. Steinmeyer. Role of intrapulse coherence in carrier-envelope phase stabilization. *Phys. Rev. Lett.*, 119(12):123901, 2017.

[68] S. Skupin, G. Stibenz, L. Bergé, F. Lederer, T. Sokollik, M. Schnürer, N. Zhavoronkov, and G. Steinmeyer. Self-compression by femtosecond pulse filamentation: experiments versus numerical simulations. *Phys. Rev. E*, 74(5):56604, 2006.

[69] T. H. Maiman. Stimulated optical radiation in ruby. *Nature*, 187(4736):493–494, 1960.

[70] M. DiDomenico. Small-signal analysis of internal (coupling-type) modulation of lasers. *J. Appl. Phys.*, 35(10):2870–2876, 1964.

[71] L. E. Hargrove, R. L. Fork, and M. A. Pollack. Locking of He–Ne laser modes induced by synchronous intracavity modulation. *Appl. Phys. Lett.*, 5(1):4–5, 1964.

[72] A. J. DeMaria, D. A. Stetser, and H. Heynau. Self mode-locking of lasers with saturable absorbers. *Appl. Phys. Lett.*, 8(7):174–176, 1966.

[73] J. Valdmanis and R. Fork. Design considerations for a femtosecond pulse laser balancing self phase modulation, group velocity dispersion, saturable absorption, and saturable gain. *IEEE J. Quantum Electron.*, 22(1):112–118, 1986.

[74] R. Hellwarth, J. Cherlow, and T.-T. Yang. Origin and frequency dependence of nonlinear optical susceptibilities of glasses. *Phys. Rev. B*, 11(2):964–967, 1975.

[75] T. Brabec, C. Spielmann, and F. Krausz. Mode locking in solitary lasers. *Opt. Lett.*, 16(24):1961–1963, 1991.

[76] Y. Chen, F. X. Kärtner, U. Morgner, S. H. Cho, H. A. Haus, E. P. Ippen, and J. G. Fujimoto. Dispersion-managed mode locking. *JOSA B*, 16(11), 1999.

[77] R. Szipöcs, C. Spielmann, F. Krausz, and K. Ferencz. Chirped multilayer coatings for broadband dispersion control in femtosecond lasers. *Opt. Lett.*, 19(3):201–203, 1994.

[78] S. Rausch, T. Binhammer, A. Harth, J. Kim, R. Ell, F. X. Kärtner, and U. Morgner. Controlled waveforms on the single-cycle scale from a femtosecond oscillator. *Opt. Express*, 16(13):9739–9745, 2008.

[79] E. P. Ippen, H. A. Haus, and L. Y. Liu. Additive pulse mode-locking. *J. Opt. Soc. Am. B*, 6(9):1736–1745, 1989.

[80] P. N. Kean, X. Zhu, D. W. Crust, R. S. Grant, N. Langford, and W. Sibbett. Enhanced mode locking of color-center lasers. *Opt. Lett.*, 14(1):39–41, 1989.

[81] V. J. Matsas, T. P. Newson, and M. N. Zervas. Self-starting passively mode-locked fibre ring laser exploiting nonlinear polarisation switching. *Opt. Commun.*, 92(1):61–66, 1992.

[82] K. Tamura, H. A. Haus, and E. P. Ippen. Self-starting additive pulse mode-locked erbium fiber ring laser. *Electron. Lett.*, 28(24):2226–2228, 1992.

[83] N. J. Doran and D. Wood. Nonlinear-optical loop mirror. *Opt. Lett.*, 13(1):56–58, 1988.

[84] M. E. Fermann, F. Haberl, M. Hofer, and H. Hochreiter. Nonlinear amplifying loop mirror. *Opt. Lett.*, 15(13):752–754, 1990.

[85] D. Brida, G. Krauss, A. Sell, and A. Leitenstorfer. Ultrabroadband Er:fiber lasers. *Laser Photon. Rev.*, 8(3):409–428, 2014.

[86] H. A. Haus, J. G. Fujimoto, and E. P. Ippen. Structures for additive pulse mode locking. *J. Opt. Soc. Am. B*, 8(10):2068–2076, 1991.

[87] H. A. Haus and A. Mecozzi. Noise of mode-locked lasers. *IEEE J. Quantum Electron.*, 29(3):983–996, 1993.

[88] T. Udem, J. Reichert, R. Holzwarth, and T. W. Hänsch. Accurate measurement of large optical frequency differences with a mode-locked laser. *Opt. Lett.*, 24(13):881–883, 1999.

[89] R. Holzwarth, T. Udem, T. W. Hänsch, J. C. Knight, W. J. Wadsworth, and P. S. J. Russell. Optical frequency synthesizer for precision spectroscopy. *Phys. Rev. Lett.*, 85(11):2264–2267, 2000.

[90] S. A. Diddams, L. Hollberg, L.-S. Ma, and L. Robertsson. Femtosecond-laser-based optical clockwork with instability $<6.3 \times 10^{-16}$ in 1 s. *Opt. Lett.*, 27(1):58–60, 2002.

[91] E. Goulielmakis, M. Uiberacker, R. Kienberger, A. Baltšska, V. Yakovlev, A. Scrinzi, T. Westerwalbesloh, U. Kleineberg, U. Heinzmann, M. Drescher, et al. Direct measurement of light waves. *Science*, 305(5688):1267–1269, 2004.

[92] I. Sola, E. Mével, L. Elouga, E. Constant, V. Strelkov, L. Poletto, P. Villoresi, E. Benedetti, J.-P. Caumes, S. Stagira, et al. Controlling attosecond electron dynamics by phase-stabilized polarization gating. *Nature Physics*, 2(5):319, 2006.

[93] H. Mashiko, S. Gilbertson, C. Li, S. D. Khan, M. M. Shakya, E. Moon, and Z. Chang. Double optical gating of high-order harmonic generation with carrier-envelope phase stabilized lasers. *Phys. Rev. Lett.*, 100(10):103906, 2008.

[94] T. W. Hänsch, R. Holzwarth, J. Reichert, and T. Udem. Measuring the frequency of light with a femtosecond laser frequency comb. *Recent Adv. Metrol. Fundam. Constants*, 146:747–764, 2001.

[95] M. Kakehata, H. Takada, Y. Kobayashi, K. Torizuka, Y. Fujihira, T. Homma, and H. Takahashi. Single-shot measurement of carrier-envelope phase changes by spectral interferometry. *Opt. Lett.*, 26(18):1436, 2001.

[96] T. Fuji, J. Rauschenberger, A. Apolonski, V. S. Yakovlev, G. Tempea, T. Udem, C. Gohle, T. W. Hänsch, W. Lehnert, M. Scherer, and F. Krausz. Monolithic carrier-envelope phase-stabilization scheme. *Opt. Lett.*, 30(3):332–334, 2005.

[97] D. C. Heinecke, A. Bartels, T. M. Fortier, D. A. Braje, L. Hollberg, and S. A. Diddams. Optical frequency stabilization of a 10 GHz ti:sapphire frequency comb by saturated absorption spectroscopy in ^{87}rubidium. *Phys. Rev. A*, 80(5):053806, 2009.

[98] J. A. Cox, W. P. Putnam, A. Sell, A. Leitenstorfer, and F. X. Kärtner. Pulse synthesis in the single-cycle regime from independent mode-locked lasers using attosecond-precision feedback. *Opt. Lett.*, 37(17):3579–3581, 2012.

[99] K. Osvay, M. Görbe, C. Grebing, and G. Steinmeyer. Bandwidth-independent linear method for detection of the carrier-envelope offset phase. *Opt. Lett.*, 32(21):3095–3097, 2007.

[100] P. Jójárt, Á. Börzsönyi, B. Borchers, G. Steinmeyer, and K. Osvay. Agile linear interferometric method for carrier-envelope phase drift measurement. *Opt. Lett.*, 37(5):836, 2012.

[101] L. Lepetit, G. Chériaux, and M. Joffre. Linear techniques of phase measurement by femtosecond spectral interferometry for applications in spectroscopy. *J. Opt. Soc. Am. B*, 12(12):2467–2474, 1995.

[102] M. Mehendale, S. A. Mitchell, J.-P. Likforman, D. M. Villeneuve, and P. B. Corkum. Method for single-shot measurement of the carrier envelope phase of a few-cycle laser pulse. *Opt. Lett.*, 25(22):1672–1674, 2000.

[103] M. Kreß, T. Löffler, M. D. Thomson, R. Dörner, H. Gimpel, K. Zrost, T. Ergler, R. Moshammer, U. Morgner, J. Ullrich, and H. G. Roskos. Determination of the carrier-envelope phase of few-cycle laser pulses with terahertz-emission spectroscopy. *Nat. Phys.*, 2(5):327–331, 2006.

[104] C. Lemell, X.-M. Tong, F. Krausz, and J. Burgdörfer. Electron emission from metal surfaces by ultrashort pulses: determination of the carrier-envelope phase. *Phys. Rev. Lett.*, 90(7):076403, 2003.

[105] A. Apolonski, P. Dombi, G. G. Paulus, M. Kakehata, R. Holzwarth, T. Udem, C. Lemell, K. Torizuka, J. Burgdörfer, T. W. Hänsch, and F. Krausz. Observation of light-phase-sensitive photoemission from a metal. *Phys. Rev. Lett.*, 92(7):073902, 2004.

[106] G. G. Paulus, F. Lindner, H. Walther, A. Baltuška, E. Goulielmakis, M. Lezius, and F. Krausz. Measurement of the phase of few-cycle laser pulses. *Phys. Rev. Lett.*, 91(25):253004, 2003.

[107] T. Wittmann, B. Horvath, W. Helml, M. G. Schätzel, X. Gu, A. L. Cavalieri, G. G. Paulus, and R. Kienberger. Single-shot carrier–envelope phase measurement of few-cycle laser pulses. *Nat. Phys.*, 5(5):357–362, 2009.

[108] N. G. Johnson, O. Herrwerth, A. Wirth, S. De, I. Ben-Itzhak, M. Lezius, B. Bergues, M. F. Kling, A. Senftleben, C. D. Schröter, R. Moshammer, J. Ullrich, K. J. Betsch, R. R. Jones, A. M. Sayler, T. Rathje, K. Rühle, W. Müller, and G. G. Paulus. Single-shot carrier-envelope-phase-tagged ion-momentum imaging of nonsequential double ionization of argon in intense 4-fs laser fields. *Phys. Rev. A*, 83(1):13412, 2011.

[109] A. Apolonski, A. Poppe, G. Tempea, C. Spielmann, T. Udem, R. Holzwarth, T. W. Hänsch, and F. Krausz. Controlling the phase evolution of few-cycle light pulses. *Phys. Rev. Lett.*, 85(4):740–743, 2000.

[110] D. J. Jones, S. A. Diddams, J. K. Ranka, A. Stentz, R. S. Windeler, J. L. Hall, and S. T. Cundiff. Carrier-envelope phase control of femtosecond mode-locked lasers and direct optical frequency synthesis. *Science*, 288(5466):635–639, 2000.

[111] L. Arissian and J. C. Diels. Carrier to envelope and dispersion control in a cavity with prism pairs. *Phys. Rev. A - At. Mol. Opt. Phys.*, 75(1):013814, 2007.

[112] T. M. Fortier, D. J. Jones, J. Ye, and S. T. Cundiff. Long-term carrier-envelope phase coherence. *Opt. Lett.*, 27(16):1436–1438, 2002.

[113] D. E. McCumber. Intensity fluctuations in the output of cw laser oscillators. *Phys. Rev.*, 141(1):306–322, 1966.

[114] M. Sheik-Bahae, D. C. Hutchings, D. J. Hagan, and E. W. Van Stryland. Dispersion of bound electronic nonlinear refraction in solids. *IEEE J. Quantum Electron.*, 27(6):1296–1309, 1991.

[115] L. Matos, O. D. Mücke, J. Chen, and F. X. Kärtner. Carrier-envelope phase dynamics and noise analysis in octave-spanning Ti:sapphire lasers. *Opt. Express*, 14(6):2497–2511, 2006.

[116] S. Koke, C. Grebing, H. Frei, A. Anderson, A. Assion, and G. Steinmeyer. Direct frequency comb synthesis with arbitrary offset and shot-noise-limited phase noise. *Nat. Photonics*, 4(7):462–465, 2010.

[117] S. Koke, A. Anderson, H. Frei, A. Assion, and G. Steinmeyer. Noise performance of a feed-forward scheme for carrier-envelope phase stabilization. *Appl. Phys. B Lasers Opt.*, 104(4):799–804, 2011.

[118] S. Koke. *Fundamental limitations in the measurement and stabilization of the Carrier-envelope phase of ultrashort laser pulses*. PhD thesis, Humboldt-Universität zu Berlin, Mathematisch-Naturwissenschaftliche Fakultät, 2012.

[119] B. Borchers. *Pushing Frontiers in Carrier-Envelope Phase Stabilization of Ultrashort Laser Pulses*. PhD thesis, Humboldt-Universität zu Berlin, Math.-Naturwiss. Fakultät, 2014.

[120] I. Thomann, E. Gagnon, R. J. Jones, A. S. Sandhu, A. Lytle, R. Anderson, J. Ye, M. Murnane, and H. Kapteyn. Investigation of a grating-based stretcher/compressor for carrier-envelope phase stabilized fs pulses. *Opt. Express*, 12(15):3493–3499, 2004.

[121] C. Li, E. Moon, and Z. Chang. Carrier-envelope phase shift caused by variation of grating separation. *Opt. Lett.*, 31(21):3113–3115, 2006.

[122] N. Forget, L. Canova, X. Chen, A. Jullien, and R. Lopez-Martens. Closed-loop carrier-envelope phase stabilization with an acousto-optic programmable dispersive filter. *Opt. Lett.*, 34(23):3647–3649, 2009.

[123] C. Feng, J.-F. Hergott, P.-M. Paul, X. Chen, O. Tcherbakoff, M. Comte, O. Gobert, M. Reduzzi, F. Calegari, C. Manzoni, M. Nisoli, and G. Sansone. Complete analog control of the carrier-envelope-phase of a high-power laser amplifier. *Opt. Express*, 21(21):25248, 2013.

[124] R. Paschotta, H. R. Telle, and U. Keller. *Noise of solid-state lasers*. In. *Solid-state lasers Application*. Volume 119. 2007, pages 473–510.

[125] H. A. Haus and E. P. Ippen. Group velocity of solitons. *Opt. Lett.*, 26(21):1654–1656, 2001.

[126] M. Y. Sander, E. P. Ippen, and F. X. Kärtner. Carrier-envelope phase dynamics of octave-spanning dispersion-managed Ti: sapphire lasers. *Opt. Express*, 18(5):4948–4960, 2010.

[127] B. R. Washburn, W. C. Swann, and N. R. Newbury. Response dynamics of the frequency comb output from a femtosecond fiber laser. *Opt. Express*, 13(26):10622–10633, 2005.

[128] A. L. Schawlow and C. H. Townes. Infrared and optical masers. *Phys. Rev.*, 112(6):1940–1949, 1958.

[129] M. Lax. Classical noise. V. Noise in self-sustained oscillators. *Phys. Rev.*, 160(2):290–307, 1967.

[130] R. Paschotta, A. Schlatter, S. C. Zeller, H. R. Telle, and U. Keller. Optical phase noise and carrier-envelope offset noise of mode-locked lasers. *Appl. Phys. B*, 82(2):265–273, 2006.

[131] N. Haverkamp, H. Hundertmark, C. Fallnich, and H. Telle. Frequency stabilization of mode-locked erbium fiber lasers using pump power control. *Appl. Phys. B*, 78(3-4):321–324, 2004.

[132] Y. Song, F. Lücking, B. Borchers, and G. Steinmeyer. On the origin of flicker noise in carrier-envelope phase stabilization. *Opt. Lett.*, 39(24):6989–6992, 2014.

[133] F. W. Helbing, G. Steinmeyer, U. Keller, R. S. Windeler, J. Stenger, and H. R. Telle. Carrier-envelope offset dynamics of mode-locked lasers. *Opt. Lett.*, 27(3):194–196, 2002.

[134] K. W. Holman, R. J. Jones, A. Marian, S. T. Cundiff, and J. Ye. Detailed studies and control of intensity-related dynamics of femtosecond frequency combs from mode-locked Ti:sapphire lasers. *IEEE J. Sel. Top. Quantum Electron.*, 9(4):1018–1024, 2003.

[135] C. Gohle, J. Rauschenberger, T. Fuji, T. Udem, A. Apolonski, F. Krausz, and T. W. Hänsch. Carrier envelope phase noise in stabilized amplifier systems. *Opt. Lett.*, 30(18):2487–2489, 2005.

[136] B. Washburn and N. Newbury. Phase, timing, and amplitude noise on supercontinua generated in microstructure fiber. *Opt. Express*, 12(10):2166–2175, 2004.

[137] J. M. Dudley, G. Genty, and S. Coen. Supercontinuum generation in photonic crystal fiber. *Rev. Mod. Phys.*, 78(4):1135–1184, 2006.

[138] B. Schenkel, R. Paschotta, and U. Keller. Pulse compression with supercontinuum generation in microstructure fibers. *J. Opt. Soc. Am. B*, 22(3):687–693, 2005.

[139] M. Pawowska, F. Ozimek, P. Fita, and C. Radzewicz. Collinear interferometer with variable delay for carrier-envelope offset frequency measurement. *Rev. Sci. Instrum.*, 80(8):083101, 2009.

[140] C. Grebing, S. Koke, B. Manschwetus, and G. Steinmeyer. Performance comparison of interferometer topologies for carrier-envelope phase detection. *Appl. Phys. B*, 95(1):81–84, 2009.

[141] F. Lücking, A. Assion, A. Apolonski, F. Krausz, and G. Steinmeyer. Long-term carrier-envelope-phase-stable few-cycle pulses by use of the feed-forward method. *Opt. Lett.*, 37(11):2076, 2012.

[142] M. Takeda, H. Ina, and S. Kobayashi. Fourier-transform method of fringe-pattern analysis for computer-based topography and interferometry. *J. Opt. Soc. Am.*, 72(1):156, 1982.

[143] K. Pearson. Note on regression and inheritance in the case of two parents. *Proc. R. Soc. London*, 58:240–242, 1895.

[144] W. H. Press, B. P. Flannery, S. A. Teukolsky, and W. T. Vetterling. *Numerical recipes in C: the art of scientific programming*, volume 10. Cambridge university press, 1992, pages 408–412. ISBN: 0-521-43108-5.

[145] M. Haahr. True random number service, 2016.

[146] H. G. Schuster and W. Just. *Deterministic Chaos: An Introduction*. 2006. ISBN: 978-3-52760-641-2.

[147] H. Kantz and T. Schreiber. *Nonlinear time series analysis*. 1997. ISBN: 978-0-52155-144-1.

[148] T. Yanagita and K. Kaneko. Rayleigh-Bénard convection patterns, chaos, spatiotemporal chaos and turbulence. *Phys. D Nonlinear Phenom.*, 82(3):288–313, 1995.

[149] K. Ikeda and K. Matsumoto. High-dimensional chaotic behavior in systems with time-delayed feedback. *Physica D: Nonlinear Phenom.*, 29(1-2):223–235, 1987.

[150] M. Bauer, H. Heng, and W. Martienssen. Characterization of spatiotemporal chaos from time series. *Phys. Rev. Lett.*, 71(4):521, 1993.

[151] E. N. Lorenz. Deterministic non-periodic flow. *J. Atmos. Sci.*, 20:130–141, 1963.

[152] J. Argyris, G. Faust, Haase, and R. Friedrich. *Die Erforschung des Chaos*. 2010. ISBN: 978-3-540-71072-1.

[153] N. H. Packard, J. P. Crutchfield, J. D. Farmer, and R. S. Shaw. Geometry from a time series. *Phys. Rev. Lett.*, 45(9):712–716, 1980.

[154] F. Takens. *Detecting strange attractors in turbulence*. In. *Lect. Notes Math.* Springer, Berlin, 1981, pages 366–381.

[155] A. M. Fraser and H. L. Swinney. Independent coordinates for strange attractors from mutual information. *Phy. Rev. Lett.*, 33(2):1134, 1986.

[156] M. B. Kennel, R. Brown, and H. D. I. Abarbanel. Determining embedding dimension for phase-space reconstruction using a geometrical construction. *Phys. Rev. A*, 45(6):3403–3411, 1992.

[157] W. Liebert, K. Pawelzik, and H. G. Schuster. Optimal embeddings of chaotic attractors from topological considerations. *Europhys. Lett.*, 14(6):521, 1991.

[158] L. M. Pecora, L. Moniz, J. Nichols, and T. L. Carroll. A unified approach to attractor reconstruction. *Chaos: An Interdiscip. J. Nonlinear Sci.*, 17(1):13110, 2007.

[159] P. Grassberger and I. Procaccia. Characterization of strange attractors. *Phys. Rev. Lett.*, 50(5):346–349, 1983.

[160] P. Grassberger and I. Procaccia. Measuring the strangeness of strange attractors. *Phys. D: Nonlinear Phenom.*, 9:189–208, 1983.

[161] J. Theiler, S. Eubank, A. Longtin, B. Galdrikian, and J. Doyne Farmer. Testing for nonlinearity in time series: the method of surrogate data. *Phys. D Nonlinear Phenom.*, 58(1-4):77–94, 1992.

[162] T. Schreiber and A. Schmitz. Surrogate time series. *Phys. D Nonlinear Phenom.*, 142(3):346–382, 2000.

[163] H. Tian, Y. Song, F. Meng, Z. Fang, M. Hu, and C. Wang. Long-term stable coherent beam combination of independent femtosecond Yb-fiber lasers. *Opt. Lett.*, 41(22):5142–5145, 2016.

[164] T. Schibli, J. Kim, O. Kuzucu, J. Gopinath, S. Tandon, G. Petrich, L. Kolodziejski, J. Fujimoto, E. Ippen, and F. Kaertner. Attosecond active synchronization of passively mode-locked lasers by balanced cross correlation. *Opt. Lett.*, 28(11):947–949, 2003.

[165] I. N. Duling. All-fiber ring soliton laser mode locked with a nonlinear mirror. *Opt. Lett.*, 16(8):539–541, 1991.

[166] C. Freed and E. Hinkley. Direct observation of the lorentzian line shape as limited by quantum phase noise in a laser above threshold. *Phy. Rev. Lett.*, 23:277–280, 1969.

[167] L. Orsila, J. Sand, M. Närhi, G. Genty, and G. Steinmeyer. Supercontinuum generation as a signal amplifier. *Optica*, 2(8):757–764, 2015.

[168] T. R. Schibli, I. Hartl, D. C. Yost, M. J. Martin, A. Marcinkevičius, M. E. Fermann, and J. Ye. Optical frequency comb with submillihertz linewidth and more than 10 W average power. *Nat. Photonics*, 2:355, 2008.

[169] W. C. Swann, J. J. McFerran, I. Coddington, N. R. Newbury, I. Hartl, M. E. Fermann, P. S. Westbrook, J. W. Nicholson, K. S. Feder, C. Langrock, and M. M. Fejer. Fiber-laser frequency combs with sub-Hertz relative linewidths. *Opt. Lett.*, 31(20):3046–3048, 2006.

[170] F. Helbing, G. Steinmeyer, U. Keller, R. Windeler, J. Stenger, and H. Telle. Carrier-envelope offset dynamics of mode-locked lasers. *Opt. Lett.*, 27(3):194–196, 2002.

[171] D. C. Heinecke, A. Bartels, and S. A. Diddams. Offset frequency dynamics and phase noise properties of a self-referenced 10 ghz ti: sapphire frequency comb. *Opt. Express*, 19(19):18440–18451, 2011.

[172] S. Hakobyan, V. J. Wittwer, P. Brochard, K. Gürel, S. Schilt, A. S. Mayer, U. Keller, and T. Südmeyer. Full stabilization and characterization of an optical frequency comb from a diode-pumped solid-state laser with Ghz repetition rate. *Opt. Express*, 25(17):20437–20453, 2017.

[173] J. Wahlstrand, J. Willits, C. Menyuk, and S. Cundiff. The quantum-limited comb lineshape of a mode-locked laser: fundamental limits on frequency uncertainty. *Opt. Express*, 16(23):18624–18630, 2008.

[174] F. X. Kärtner. *Few-cycle laser pulse generation and its applications*, volume 95. Springer Science & Business Media, 2004.

[175] K. Vahala and A. Yariv. Semiclassical theory of noise in semiconductor lasers - part I. *IEEE J. Quantum Electron.*, 19(6):1096–1101, 1983.

[176] A. Karlsson and G. Björk. Use of quantum-noise correlation for noise reduction in semiconductor lasers. *Phys. Rev. A*, 44(11):7669–7683, 1991.

[177] W. H. Richardson and Y. Yamamoto. Quantum correlation between the junction-voltage fluctuation and the photon-number fluctuation in a semiconductor laser. *Phys. Rev. Lett.*, 66(15):1963–1966, 1991.

[178] M. Haiml, R. Grange, and U. Keller. Optical characterization of semiconductor saturable absorbers. *Appl. Phys. B*, 79(3):331–339, 2004.

[179] G. Stibenz, G. Steinmeyer, and W. Richter. Dynamic spectral interferometry for measuring the nonlinear amplitude and phase response of a saturable absorber mirror. *Appl. Phys. Lett.*, 86(8):81105, 2005.

[180] C.-C. Lee, C. Mohr, J. Bethge, S. Suzuki, M. E. Fermann, I. Hartl, and T. R. Schibli. Frequency comb stabilization with bandwidth beyond the limit of gain lifetime by an intracavity graphene electro-optic modulator. *Opt. Lett.*, 37(15):3084–3086, 2012.

[181] E. Goulielmakis, M. Schultze, M. Hofstetter, V. S. Yakovlev, J. Gagnon, M. Uiberacker, A. L. Aquila, E. M. Gullikson, D. T. Attwood, R. Kienberger, F. Krausz, and U. Kleineberg. Single-cycle nonlinear optics. *Science*, 320(5883):1614–1617, 2008.

[182] A. Guandalini, P. Eckle, M. Anscombe, P. Schlup, J. Biegert, and U. Keller. 5.1 fs pulses generated by filamentation and carrier envelope phase stability analysis. *J. Phys. B: A., Mol. Opt. Phys.*, 39(13):257, 2006.

[183] G. Steinmeyer, B. Borchers, and F. Lücking. Carrier-envelope phase stabilization. In, *Prog. Ultrafast Intense Laser Sci. Vol. IX*, pages 89–110. Springer, 2013. ISBN: 978-3-642-35052-8.

[184] A. Couairon and A. Mysyrowicz. Femtosecond filamentation in transparent media. *Phys. Rep.*, 441(2-4):47–189, 2007.

[185] M. K. Reed, M. K. Steiner-Shepard, and D. K. Negus. Widely tunable femtosecond optical parametric amplifier at 250 kHz with a Ti:sapphire regenerative amplifier. *Opt. Lett.*, 19(22):1855–1857, 1994.

[186] M. K. Reed, M. K. Steiner-Shepard, M. S. Armas, and D. K. Negus. Microjoule-energy ultrafast optical parametric amplifiers. *J. Opt. Soc. Am. B*, 12(11):2229–2236, 1995.

[187] M. Bradler, P. Baum, and E. Riedle. Femtosecond continuum generation in bulk laser host materials with sub-μJ pump pulses. *Appl. Phys. B*, 97(3):561, 2009.

[188] M. J. Weber. *Handbook of optical materials*, volume 19. 2002. ISBN: 978-1-42005-019-6.

[189] Á. Börzsönyi, Z. Heiner, A. P. Kovács, M. P. Kalashnikov, and K. Osvay. Measurement of pressure dependent nonlinear refractive index of inert gases. *Opt. Express*, 18(25):25847–25854, 2010.

[190] A. Couairon, L. Sudrie, M. Franco, B. Prade, and A. Mysyrowicz. Filamentation and damage in fused silica induced by tightly focused femtosecond laser pulses. *Phys. Rev. B*, 71(12):125435, 2005.

[191] R. Adair, L. L. Chase, and S. A. Payne. Nonlinear refractive index of optical crystals. *Phys. Rev. B*, 39(5):3337–3350, 1989.

[192] A. Dubietis, G. Tamošauskas, R. Šuminas, V. Jukna, and A. Couairon. Ultrafast supercontinuum generation in bulk condensed media. *Lith. J. Phys.*, 57(3):113–157, 2017.

[193] R. Desalvo, A. A. Said, D. J. Hagan, E. W. V. Stryland, and M. Sheik-Bahae. Infrared to ultraviolet measurements of two-photon absorption and n_2 in wide bandgap solids. *IEEE J. Quantum Electron.*, 32(8):1324–1333, 1996.

[194] P. B. Corkum, C. Rolland, and T. Srinivasan-Rao. Supercontinuum generation in gases. *Phys. Rev. Lett.*, 57(18):2268–2271, 1986.

[195] H. M. Milchberg, Y.-H. Chen, Y.-H. Cheng, N. Jhajj, J. P. Palastro, E. W. Rosenthal, S. Varma, J. K. Wahlstrand, and S. Zahedpour. The extreme nonlinear optics of gases and femtosecond optical filamentation. *Phys. Plasmas*, 21(10):100901, 2014.

[196] J. K. Ranka, R. S. Windeler, and A. J. Stentz. Visible continuum generation in air–silica microstructure optical fibers with anomalous dispersion at 800 nm. *Opt. Lett.*, 25(1):25–27, 2000.

[197] J. C. Knight. Photonic crystal fibres. *Nature*, 424(6950):847–851, 2003.

[198] A. V. Husakou and J. Herrmann. Supercontinuum generation of higher-order solitons by fission in photonic crystal fibers. *Phys. Rev. Lett.*, 87(20):203901, 2001.

[199] M. Kakehata, Y. Fujihira, H. Takada, Y. Kobayashi, K. Torizuka, T. Homma, and H. Takahashi. Measurements of carrier-envelope phase changes of 100-Hz amplified laser pulses. *Appl. Phys. B*, 74(1):43–50, 2002.

[200] A. Harth, M. Schultze, T. Lang, T. Binhammer, S. Rausch, and U. Morgner. Two-color pumped OPCPA system emitting spectra spanning 1.5 octaves from VIS to NIR. *Opt. Express*, 20(3):3076–3081, 2012.

[201] J. Kohl-Landgraf, J.-E. Nimsch, and J. Wachtveitl. LiF, an underestimated supercontinuum source in femtosecond transient absorption spectroscopy. *Opt. Express*, 21(14):17060–17065, 2013.

[202] C.-H. Lu, Y.-J. Tsou, H.-Y. Chen, B.-H. Chen, Y.-C. Cheng, S.-D. Yang, M.-C. Chen, C.-C. Hsu, and A. H. Kung. Generation of intense supercontinuum in condensed media. *Optica*, 1(6):400–406, 2014.

[203] E. Riedle, M. Beutter, S. Lochbrunner, J. Piel, S. Schenkl, S. Spörlein, and W. Zinth. Generation of 10 to 50 fs pulses tunable through all of the visible and the NIR. *Appl. Phys. B*, 71(3):457–465, 2000.

[204] S. A. Kovalenko, A. L. Dobryakov, J. Ruthmann, and N. P. Ernsting. Femtosecond spectroscopy of condensed phases with chirped supercontinuum probing. *Phys. Rev. A*, 59(3):2369, 1999.

[205] T. Bizjak, J. Karpiuk, S. Lochbrunner, and E. Riedle. 50-fs photoinduced intramolecular charge separation in triphenylmethane lactones. *J. Phys. Chem. A*, 108(49):10763–10769, 2004.

[206] B. Schmidt, C. Sobotta, S. Malkmus, S. Laimgruber, M. Braun, W. Zinth, and P. Gilch. Femtosecond fluorescence and absorption dynamics of an azobenzene with a strong push- pull substitution. *J. Phys. Chem. A*, 108(20):4399–4404, 2004.

[207] R. Lindner, R. T. Williams, and M. Reichling. Time-dependent luminescence of self-trapped excitons in alkaline-earth fluorides excited by femtosecond laser pulses. *Phys. Rev. B*, 63(7):75110, 2001.

[208] D. C. Hutchings. Nonlinear-optical activity owing to anisotropy of ultrafast nonlinear refraction in cubic materials. *Opt. Lett.*, 20(15):1607–1609, 1995.

[209] P. J. M. Johnson, V. I. Prokhorenko, and R. J. D. Miller. Stable UV to IR supercontinuum generation in calcium fluoride with conserved circular polarization states. *Opt. Express*, 17(24):21488–21496, 2009.

[210] I. Buchvarov, A. Trifonov, and T. Fiebig. Toward an understanding of white-light generation in cubic media - polarization properties across the entire spectral range. *Opt. Lett.*, 32(11):1539–1541, 2007.

[211] M. Nisoli, S. De Silvestri, and O. Svelto. Generation of high energy 10 fs pulses by a new pulse compression technique. *Appl. Phys. Lett.*, 68(20):2793–2795, 1996.

[212] E. Goulielmakis, S. Koehler, B. Reiter, M. Schultze, A. J. Verhoef, E. E. Serebryannikov, a. M. Zheltikov, and F. Krausz. Ultrabroadband, coherent light source based on self-channeling of few-cycle pulses in helium. *Opt. Lett.*, 33(13):1407–1409, 2008.

[213] Y.-H. Cheng, J. K. Wahlstrand, N. Jhajj, and H. M. Milchberg. The effect of long timescale gas dynamics on femtosecond filamentation. *Opt. Express*, 21(4):4740, 2013.

[214] N. T. Nguyen, A. Saliminia, W. Liu, S. L. Chin, and R. Vallée. Optical breakdown versus filamentation in fused silica by use of femtosecond infrared laser pulses. *Opt. Lett.*, 28(17):1591–1593, 2003.

[215] M. Kretschmar, C. Brée, T. Nagy, A. Demircan, H. G. Kurz, U. Morgner, and M. Kovačev. Direct observation of pulse dynamics and self-compression along a femtosecond filament. *Opt. Express*, 22(19):22905–22916, 2014.

[216] L. Bergé, S. Skupin, and G. Steinmeyer. Temporal self-restoration of compressed optical filaments. *Phys. Rev. Lett.*, 101(21):213901, 2008.

[217] Y.-C. Cheng, C.-H. Lu, Y.-Y. Lin, and A. H. Kung. Supercontinuum generation in a multi-plate medium. *Opt. Express*, 24(7):7224, 2016.

[218] P. He, Y. Liu, K. Zhao, H. Teng, X. He, P. Huang, H. Huang, S. Zhong, Y. Jiang, S. Fang, X. Hou, and Z. Wei. High-efficiency supercontinuum generation in solid thin plates at 0.1 TW level. *Opt. Lett.*, 42(3):474–477, 2017.

[219] Y. R. Shen. Surface properties probed by second-harmonic and sum-frequency generation. *Nature*, 337(6207):519–525, 1989.

[220] A. V. Smith. SNLO nonlinear optics program, 2017.

[221] M. Iwai, T. Yoshino, S. Yamaguchi, M. Imaeda, N. Pavel, I. Shoji, and T. Taira. High-power blue generation from a periodically poled MgO:$LiNbO_3$ ridge-type waveguide by frequency doubling of a diode end-pumped Nd:$O_3Al_5O_{12}$ laser. *Appl. Phys. Lett.*, 83(18):3659–3661, 2003.

[222] H. Hellwig, J. Liebertz, and L. Bohatý. Exceptional large nonlinear optical coefficients in the monoclinic bismuth borate BiB_3O_6. *Solid State Commun.*, 109(4):249–251, 1998.

[223] Z. Wang, B. Teng, K. Fu, X. Xu, R. Song, C. Du, H. Jiang, J. Wang, Y. Liu, and Z. Shao. Efficient second harmonic generation of pulsed laser radiation in BiB_3O_6 (BiBO) crystal with different phase matching directions. *Opt. Commun.*, 202(1-3):217–220, 2002.

[224] M. Ghotbi, M. Ebrahim-Zadeh, A. Majchrowski, E. Michalski, and I. V. Kityk. High-average-power femtosecond pulse generation in the blue using BiB_3O_6. *Opt. Lett.*, 29(21):2530–2532, 2004.

[225] T. Harimoto, Y. Takeuchi, and M. Fujita. Spectral properties of second-harmonic generation at 800 nm in a BiB_3O_6 crystal. *Opt. Express*, 12(5):811–816, 2004.

[226] X. Gu, L. Xu, M. Kimmel, E. Zeek, P. O'Shea, A. P. Shreenath, R. Trebino, and R. S. Windeler. Frequency-resolved optical gating and single-shot spectral measurements reveal fine structure in microstructure-fiber continuum. *Opt. Lett.*, 27(13):1174–1176, 2002.

[227] D. R. Solli, C. Ropers, P. Koonath, and B. Jalali. Optical rogue waves. *Nature*, 450(7172):1054, 2007.

[228] K. L. Corwin, N. R. Newbury, J. M. Dudley, S. Coen, S. A. Diddams, K. Weber, and R. S. Windeler. Fundamental noise limitations to supercontinuum generation in microstructure fiber. *Phys. Rev. Lett.*, 90(11):113904, 2003.

[229] N. R. Newbury, B. R. Washburn, K. L. Corwin, and R. S. Windeler. Noise amplification during supercontinuum generation in microstructure fiber. *Opt. Lett.*, 28(11):944–946, 2003.

[230] D. Majus and A. Dubietis. Statistical properties of ultrafast supercontinuum generated by femtosecond Gaussian and Bessel beams: a comparative study. *J. Opt. Soc. Am. B*, 30(4):994–999, 2013.

[231] H. Wang, M. Chini, E. Moon, H. Mashiko, C. Li, and Z. Chang. Coupling between energy and phase in hollow-core fiber based f-to-2f interferometers. *Opt. Express*, 17(14):12082–12089, 2009.

[232] M. Czerny and A. F. Turner. Über den Astigmatismus bei Spiegelspektrometern. *Zeitschrift für Phys.*, 61(11-12):792–797, 1930.

[233] A. Demircan and U. Bandelow. Analysis of the interplay between soliton fission and modulation instability in supercontinuum generation. *Appl. Phys. B*, 86(1):31–39, 2007.

[234] M. Bellini and T. W. Hänsch. Phase-locked white-light continuum pulses: toward a universal optical frequency-comb synthesizer. *Opt. Lett.*, 25(14):1049–1051, 2000.

[235] J. Ratner, G. Steinmeyer, T. C. Wong, R. Bartels, and R. Trebino. Coherent artifact in modern pulse measurements. *Opt. Lett.*, 37(14):2874–2876, 2012.

[236] M. Rhodes, G. Steinmeyer, J. Ratner, and R. Trebino. The coherent artifact in modern pulse measurements. *CLEO/Europe-IQEC 2013*, 37(14):2874–6, 2013.

[237] J. M. Dudley and S. Coen. Numerical simulations and coherence properties of supercontinuum generation in photonic crystal and tapered optical fibers. *IEEE J. Sel. Top. Quantum Electron.*, 8(3):651–659, 2002.

[238] G. Genty, A. T. Friberg, and J. Turunen. Coherence of supercontinuum light. *Prog. Opt.*, 61(18):71–112, 2016.

[239] W. Watanabe, Y. Masuda, H. Arimoto, and K. Itoh. Coherent array of white-light continuum generated by microlens array. *Opt. Rev.*, 6(3):167–172, 1999.

[240] S. L. Chin, S. Petit, F. Borne, and K. Miyazaki. The white light supercontinuum is indeed an ultrafast white light laser. *Jpn. J. Appl. Phys.*, 38(2A):126, 1999.

[241] D. Wegkamp, D. Brida, S. Bonora, G. Cerullo, J. Stähler, M. Wolf, and S. Wall. Phase retrieval and compression of low-power white-light pulses. *Appl. Phys. Lett.*, 99(10):101101, 2011.

[242] C. Corsi, A. Tortora, and M. Bellini. Mutual coherence of supercontinuum pulses collinearly generated in bulk media. *Appl. Phys. B*, 77(2):285–290, 2003.

[243] G. Paulus, F. Grasbon, H. Walther, P. Villoresi, M. Nisoli, S. Stagira, E. Priori, and S. De Silvestri. Absolute-phase phenomena in photoionization with few-cycle laser pulses. *Nature*, 414(6860):182, 2001.

[244] X. D. Cao, G. P. Agrawal, and C. J. McKinstrie. Self-focusing of chirped optical pulses in nonlinear dispersive media. *Phys. Rev. A*, 49(5):4085–4092, 1994.

[245] L. Bergé, J. J. Rasmussen, E. A. Kuznetsov, E. G. Shapiro, and S. K. Turitsyn. Self-focusing of chirped optical pulses in media with normal dispersion. *J. Opt. Soc. Am. B*, 13(9):1879–1891, 1996.

[246] A. Baltuška, T. Fuji, and T. Kobayashi. Self-referencing of the carrier-envelope slip in a 6-fs visible parametric amplifier. *Opt. Lett.*, 27(14):1241–1243, 2002.

Acknowledgement

To conclude, I would like to thank all people involved during the course of this thesis.

First of all, I would like to thank Prof. Marc Vrakking for giving me the opportunity to carry out research at the Max Born Institute and the supervision he provided.
Furthermore, I would like to thank the external reviewers and the examining board.

A special thanks goes to Prof. Günter Steinmeyer for providing extensive supervision, advice and creating the framework conditions enabling the direction of this research.

Additionally, I would like to thank Oleg Kornilov for his support especially during the writing phase. Further, I'am grateful to Tobias Witting, Mark Mero, Federico Furch and Horst Rottke for sharing their knowledge and support.

For my time in france I would like to give thanks to Pierre-Mary Paul, Xiaowei Chen, Emilien Gontier, Jean-Francois Hergott, Olivier Tcherbakoff, David Gazella and Pascal D'Oliveira.

For extensive collaborations involving several companies and universities, I would like to thank Youjian Song, Haochen Tian, Wolfgang Hänsel, Ronald Holzwarth, Alexander Sell, Armin Zach, Carsten Bree and Ayhan Demicran.

Furthermore, I would like to thank my colleagues Tianli Feng, Pascal Rustige, Simon Birkholz, Janne Hyyti, Lorenz von Grafenstein, Esmerando Escoto, Felix Mahler and Bastian Borchers for creating a creative and fruitful environment and many interesting discussions. Moreover, I want to thank my friends Danilo Brambila and Christof Barth.

Finally, I would like to express my deepest gratitude to my family and friends for supporting me throughout my studies.